Elastohydrodynamic interactions at small scales

by

Babak Nasouri

B.Sc., Sharif University of Technology, 2012

M.Sc., The University of Texas at Austin, 2014

A THESIS SUBMITTED IN PARTIAL FULFILLMENT

OF THE REQUIREMENTS FOR THE DEGREE OF

Doctor of Philosophy

in

THE FACULTY OF GRADUATE AND POSTDOCTORAL STUDIES

(Mechanical Engineering)

The University of British Columbia

(Vancouver)

August 2018

The following individuals certify that they have read, and recommend to the Faculty of Graduate and Postdoctoral Studies for acceptance, the dissertation entitled:

Elastohydrodynamic interactions at small scales

submitted by Babak Nasouri in partial fulfillment of the requirements for

the degree of Doctor of Philosophy

in Mechanical Engineering

Examining Committee:

Gwynn J. Elfring, Mechanical Engineering
Supervisor

George M. Homsy, Mathematics
Supervisory Committee Member

Brian Wetton, Mathematics
University Examiner

Boris Stoeber, Mechanical Engineering
University Examiner

Additional Supervisory Committee Members:

Neil J. Balmforth, Mathematics
Supervisory Committee Member

A. Srikantha Phani, Mechanical Engineering
Supervisory Committee Member

Abstract

In this dissertation, the effects of elasticity on hydrodynamic interactions at small scales are investigated.

In the microscale realm of microorganisms, inertia is irrelevant and viscous dissipation dominates the fluid motion and particles within it. As a result of this inertialess environment, microorganisms use non-reciprocal body distortions to facilitate locomotion and exhibit nontrivial behaviors in interacting with their surroundings; behaviors that have been shown to be intimately correlated to the elasticity of the cell body, or its small appendages called flagella (or cilia). Motivated by experimental observations, the effects of elasticity on hydrodynamic interactions of motile cells are investigated, using theoretical approaches. First, to model the flow field induced by microswimmers, a framework is given to account for the effects of the higher-order force moments. Specifically, the contribution of the second-order force moments of the flow field is evaluated, and explicit formulas are reported for the stresslet dipole, rotlet dipole, and potential dipole for an arbitrarily shaped active particle. For an elastic swimmer near a boundary, it is shown that the rotlet dipole bends the swimmer and results in qualitatively different swimming behaviors in comparison to the case of a rigid swimmer. Furthermore, it is demonstrated that elasticity can be exploited to evade the kinematic reversibility of the field equations in Stokes flow. A model elastic swimmer is proposed that despite the reversible actuation, can propel forward due to its nonreciprocal body deformations. The effect of elasticity in the formation of metachronal waves in ciliated microorganisms such as *Paramecium* and *Volvox* is also studied. Using a minimal model, it is shown that elastohydrodynamic interactions of cilia attached to a curved body lead to synchronization, with zero phase difference, thereby preventing the formation of

wave-like behaviors unless an asymmetry is introduced to the system. Finally, the dynamics of capillary rise between two porous and elastic sheets are investigated. The liquid, as it rises, diffuses through the sheets and changes their properties. The significant drop in sheet bending rigidity due to wetting, causes the system to coalesce faster, compared to the case of impermeable sheets, and also remarkably reduces the absorbance capacity.

Lay Summary

At microscopic scales, locomotion in fluid requires swimming techniques that are utterly different from the ones we use in our macroscopic world. Microorganisms such as spermatozoa and bacteria, use elasticity to creep around, evade a predator, and to interact with their environment in fluids. Using mathematical models, we examine the effects of body elasticity on the behaviors of microorganisms and show that, indeed, elasticity can play a key role in motion of a cell in fluids. We further highlight the importance of flexibility in interactions in fluids and study the liquid rise between two porous, flexible paper sheets to explain the liquid absorptivity of multi-ply papers.

Preface

The contents of this dissertation are the results of the research of the author, Babak Nasouri, under the supervision of Professor Gwynn J. Elfring. The following articles has been published and/or are in progress:

- B. Nasouri, G. J. Elfring, *'Higher-order force moments of active particles'*, Physical Review Fluids, **3** 044101 (2018).
  The author of this dissertation was the principal contributor. G. J. Elfring supervised the research and was involved in the concept formation, analysis and editing of the paper.

- B. Nasouri, A. Khot, G. J. Elfring, *'Elastic two-sphere swimmer in Stokes flow'*, Physical Review Fluids, **2** 043101 (2017).
  The author of this dissertation was the principal contributor. A. Khot contributed in the concept formation. G. J. Elfring supervised the research and was involved in the concept formation, analysis and editing of the paper.

- B. Nasouri, G. J. Elfring, *'Hydrodynamic interactions of cilia on a spherical body'*, Physical Review E, **93** 033111 (2016).
  The author of this dissertation was the principal contributor. G. J. Elfring supervised the research and was involved in the concept formation, analysis and editing of the paper.

- B. Nasouri, B. Thorne, G. J. Elfring, *'Dynamics of poroelastocapillary rise'*, submitted.
  The author of this dissertation was the principal contributor. B. Thorne performed the experiments. G. J. Elfring supervised the research and was

involved in the concept formation, analysis and editing of the paper.

- B. Nasouri, S. E. Spagnolie, G. J. Elfring, *'Elastic active particles near a wall'*, in progress.
  The author of this dissertation was the principal contributor. S.E. Spagnolie and G. J. Elfring supervised the research and was involved in the concept formation, analysis and editing of the paper.

Table of Contents

List of Figures

Acknowledgments

First and foremost, I'd like to express my sincere gratitude and appreciation to my advisor Prof. Gwynn J. Elfring. Gwynn! Thanks for giving me the opportunity of being your PhD student. Thanks for your exceptional patience towards my painfully-naive questions. Thanks for showing me the steps to become a scientist. And as importantly, thanks for being a knowledgeable soccer fan with whom I can rigorously discuss every game.

I'd like to thank the members of my advisory committee: Prof. George (Bud) M. Homsy, Prof. Neil J. Balmforth, and Prof. A. Srikantha Phani. Bud! It was my true honor to have you as my committee member. Your deep (and in my opinion unbounded) knowledge of fluid dynamics inspired me dearly. Neil! This dissertation is heavily based on asymptotic analysis, and I was quite privileged to learn the basics from you, and will be always thankful for that.

I'd like to thank all my labmates in Complex Fluids Lab at UBC for making my grad life more enjoy full and fun. I specially want to thank them for listening to (and probably surviving) my (seemingly) odd theories about almost everything.

This journey could have not been possible without the unconditional support and love of my parents, my brother and my (always) little sister. I am thankful to all of them and forever grateful for having them in my life.

Last but certainly not least, I'd like to thank my new family for supporting me every step of the way.

Babak Nasouri
Vancouver, Canada
August 2018

Dedication

To my Yasaman.

Epigraph

There was a time that the pieces fit, but I watched them fall away
Mildewed and smoldering, strangled by our coveting
I've done the math enough to know the dangers of our second guessing
Doomed to crumble unless we grow, and strengthen our communication

Schism, TOOL

Chapter 1

Introduction

In this dissertation, we intend to investigate the interactions between hydrodynamic forces and elasticity, and the phenomena their coupling creates. As the title of the dissertation suggests, we focus on such interactions at very small scales to comprehend a realm that our intuition may not be accustomed to. A realm wherein inertia is irrelevant and viscous dissipation governs the motion of the fluid.

But why do elastohydrodynamic interactions matter at small scales? It is needless to say that microorganisms, which are the overwhelming majority inhabitants of our world, have a significant impact on our lives. Many of these micron-sized cells are elastic themselves, and/or possess whip-like extensions, called flagella (or cilia), that are flexible thereby making these interactions ubiquitous in nature [65, 66, 153]. For instance, a spermatozoa uses its flagellum to swim toward the ovum and bacteria such as *E. coli* buckle their flagella to change their swimming direction [177]. Another important example is the coordinated beating pattern of cilia, often labeled as metachronal waves [78]. By forming these waves, cilia filter the air flow channels in the human lung from the harmful inhaled material [171], play a crucial role in breaking the left-right symmetry in human embryonic development [87], and also help microorganisms such as *Paramecium* to evade predator rotifers [109]. The contribution of elasticity to all of these phenomena, further highlights the importance of understanding elastohydrodynamic interactions of motile cells and their surrounding environment. Indeed, we demonstrate that elasticity can qualitatively alter the behavior of cells: It can be exploited to generate propulsion, it

can lead to synchrony of cilia on a curved ciliate body, and also it is able to prevent entrapment of swimmers by nearby obstacles.

Furthermore, elasticity may also be coupled with capillary forces and exhibit astounding physical phenomena such as origami [158] and substrate wrinkling [90]. In fact, this coupling, known as elastocapillarity, occurs quite frequently in our day-to-day life. When wiping a coffee spill, the liquid diffuses between the plies of the paper napkin, makes them softer and also drives them toward a coalescence. We show that such a coalescence is a direct consequence of the paper porosity and elasticity, and it can affect the absorbance capacity of the paper significantly.

1.1 Outline

This dissertation explores the elastohydrodynamic interactions in two different class of problems. In Chapters 3 to 6 the effects of elasticity on microorganisms is studied, while in Chapter 7 the dynamical behavior of elastic sheets due to capillary rise is investigated.

We begin with a brief introduction to Stokes flow in Chapter 2. In this short chapter, we re-derive two fundamental equations related to Stokes flow, namely the reciprocal theorem and the boundary integral equation, which are frequently used throughout this dissertation.

In Chapter 3, we delve deeper into Stokes flow and use the boundary integral equation to express the disturbance flow field induced by motion of active particles. In particular, we evaluate the contribution of the second-order force moments to the flow field and, by the reciprocal theorem, present explicit formulas for the stresslet dipole, rotlet dipole, and potential dipole for an arbitrarily shaped active particle. As examples of this method, we derive modified Faxén laws for active spherical particles and resolve higher-order moments for active rod-like particles.

We characterize the effect of elasticity in interaction of a swimmer with a nearby wall in Chapter 4. We show that the elastic bending of the swimmer due to the presence of the wall contributes significantly to the swimming direction and can lead to attraction or repulsion, depending on the propulsion mechanism.

In Chapter 5, we inquire about the effect of elasticity on swimming in Stokes flow. We first look into pure translation of an weakly-elastic spherical particle and

show that its shape deformation is not front-back symmetric. We then propose a swimmer that can exploit this asymmetry to propel itself forward.

We then study the effects of elasticity on coordinated beating pattern of cilia on the surface of microorganisms in Chapter 6. Using a minimal model, we show that two cilia attached to a curved body synchronize purely through elastohydrodynamic interactions. We also show that for a chain of cilia, the natural periodicity in the geometry of the ciliate body prevents formation of any wave-like behavior unless an asymmetry is introduced to the system.

As the last step, we explore the coupling of elastic forces with capillary forces in Chapter 7. We study the dynamical behavior of two elastic and porous sheets immersed into a liquid bath. Accounting for the change of sheets stiffness due to wetting, we discuss the time-evolving behavior of the meniscus and the sheets' deflections as the system reaches the equilibrium.

Finally in Chapter 8, we finish the dissertation with concluding remarks.

Chapter 2

Stokes Flow

This dissertation is focused on motions in viscous fluids at very small scales. In problems discussed in Chapters 3 to 6, and also the capillary-induced motion studied in Chapter 7, the scale of the problem is so small that the effect of inertia is negligible and the field equations are governed by the Stokes equations

$$\boldsymbol{\nabla} \cdot \boldsymbol{\sigma} = \mu \nabla^2 \mathbf{u} - \boldsymbol{\nabla} p = \mathbf{0}, \tag{2.1}$$

$$\boldsymbol{\nabla} \cdot \mathbf{u} = 0, \tag{2.2}$$

where $\boldsymbol{\sigma}$ is the stress field, $\mathbf{u}$ is the flow field, p is the pressure field, and μ is the dynamic viscosity. Given that these field equations are linear, it is insightful to determine the Green's function; the system response to a point force. We thence prescribe a vector point force $\mathbf{F}$ applied on the fluid at $\mathbf{x}_0$ as,

$$\mu \nabla^2 \mathbf{u} - \boldsymbol{\nabla} p + \mathbf{F} \delta (\mathbf{x} - \mathbf{x}_0) = \mathbf{0}. \tag{2.3}$$

The induced pressure field, flow field, and stress field are respectively

$$p = \frac{1}{8\pi} \mathbf{F} \cdot \mathbf{P} (\mathbf{x} - \mathbf{x}_0), \tag{2.4}$$

$$\mathbf{u} = \frac{1}{8\pi\mu} \mathbf{F} \cdot \mathbf{J} (\mathbf{x} - \mathbf{x}_0), \tag{2.5}$$

$$\boldsymbol{\sigma} = \frac{1}{8\pi} \mathbf{F} \cdot \mathbf{K} (\mathbf{x} - \mathbf{x}_0), \tag{2.6}$$

where

$$\mathbf{J}(\mathbf{x}) = \frac{\mathbf{I}}{|\mathbf{x}|} + \frac{\mathbf{xx}}{|\mathbf{x}|^3}, \tag{2.7}$$

is the Green's function of the Stokes equations, often referred to as the Oseen tensor, and

$$\mathbf{P}(\mathbf{x}) = \frac{2\mathbf{x}}{|\mathbf{x}|^3}, \tag{2.8}$$

$$\mathbf{K}(\mathbf{x}) = \frac{-6\mathbf{xxx}}{|\mathbf{x}|^5}, \tag{2.9}$$

are its associated pressure and stress tensor, respectively.

In the following, we re-derive two fundamental equations related to Stokes flow that are frequently used throughout this dissertation. We begin with the reciprocal theorem and then use that to derive the boundary integral equation. The following derivations can be simply found in the classical references (see for instance [98] or [154]), but here are reproduced to set the foundation for the next chapters in the dissertation.

2.1 Lorentz reciprocal theorem

Let us now consider two flows characterized by $\{\mu, p, \mathbf{u}, \boldsymbol{\sigma}\}$ and $\{\tilde{\mu}, \tilde{p}, \tilde{\mathbf{u}}, \tilde{\boldsymbol{\sigma}}\}$. We can write

$$\begin{aligned} \boldsymbol{\nabla} \cdot (\tilde{\mathbf{u}} \cdot \boldsymbol{\sigma}) &= \boldsymbol{\nabla}\tilde{\mathbf{u}} : \boldsymbol{\sigma} + \tilde{\mathbf{u}} \cdot (\boldsymbol{\nabla} \cdot \boldsymbol{\sigma}), \\ &= \boldsymbol{\nabla}\tilde{\mathbf{u}} : \boldsymbol{\sigma}, \end{aligned} \tag{2.10}$$

where we have used $\boldsymbol{\nabla} \cdot \boldsymbol{\sigma} = \mathbf{0}$. The constitutive equation for a viscous fluid dictates

$$\boldsymbol{\sigma} = -p\mathbf{I} + 2\mu\mathbf{E}, \tag{2.11}$$

where $\mathbf{E} = \frac{1}{2}\left(\boldsymbol{\nabla}\mathbf{u} + \boldsymbol{\nabla}\mathbf{u}^T\right)$ is the rate-of-strain tensor. By substituting $\boldsymbol{\sigma}$ from (2.11) in (2.10), we arrive at

$$\boldsymbol{\nabla} \cdot (\tilde{\mathbf{u}} \cdot \boldsymbol{\sigma}) = -p\boldsymbol{\nabla} \cdot \tilde{\mathbf{u}} + 2\mu\boldsymbol{\nabla}\tilde{\mathbf{u}} : \mathbf{E}. \tag{2.12}$$

From continuity $\boldsymbol{\nabla} \cdot \tilde{\mathbf{u}} = 0$. Now, by exploiting the symmetry of $\mathbf{E}$ and defining $\tilde{\mathbf{E}} = \frac{1}{2}\left(\boldsymbol{\nabla}\tilde{\mathbf{u}} + \boldsymbol{\nabla}\tilde{\mathbf{u}}^T\right)$, one can show $\boldsymbol{\nabla}\tilde{\mathbf{u}} : \mathbf{E} = \frac{1}{2}\tilde{\mathbf{E}} : \mathbf{E}$, which leads to

$$\boldsymbol{\nabla} \cdot (\tilde{\mathbf{u}} \cdot \boldsymbol{\sigma}) = \mu\tilde{\mathbf{E}} : \mathbf{E}. \tag{2.13}$$

Repeating the same procedure, we find

$$\boldsymbol{\nabla} \cdot (\mathbf{u} \cdot \tilde{\boldsymbol{\sigma}}) = \tilde{\mu}\mathbf{E} : \tilde{\mathbf{E}}. \tag{2.14}$$

But, due to their symmetry $\mathbf{E} : \tilde{\mathbf{E}} = \tilde{\mathbf{E}} : \mathbf{E}$, so from (2.13) and (2.14) we can conclude

$$\tilde{\mu}\boldsymbol{\nabla} \cdot (\tilde{\mathbf{u}} \cdot \boldsymbol{\sigma}) = \mu\boldsymbol{\nabla} \cdot (\mathbf{u} \cdot \tilde{\boldsymbol{\sigma}}). \tag{2.15}$$

It is useful to integrate Eq. (2.15) over a volume of fluid in domain $\mathcal{B}$ as

$$\tilde{\mu}\int_{\mathcal{B}} \boldsymbol{\nabla} \cdot (\tilde{\mathbf{u}} \cdot \boldsymbol{\sigma})\,\mathrm{d}V = \mu\int_{\mathcal{B}} \boldsymbol{\nabla} \cdot (\mathbf{u} \cdot \tilde{\boldsymbol{\sigma}})\,\mathrm{d}V. \tag{2.16}$$

Provided that flow fields and stress fields are not singular within the considered domain, we may use the divergence theorem to convert the volume integrals ($\mathcal{B}$) to surface integrals ($\partial\mathcal{B}$) as

$$\tilde{\mu}\int_{\partial\mathcal{B}} \mathbf{n} \cdot \boldsymbol{\sigma} \cdot \tilde{\mathbf{u}}\,\mathrm{d}S = \mu\int_{\partial\mathcal{B}} \mathbf{n} \cdot \tilde{\boldsymbol{\sigma}} \cdot \mathbf{u}\,\mathrm{d}S, \tag{2.17}$$

where $\mathbf{n}$ is the surface normal of boundary $\partial\mathcal{B}$. Expressions given in Eqs. (2.15) to (2.17) are different forms of the reciprocal theorem and can be used to simplify the calculations in Stokes flow, as we illustrate in Chapter 3.

2.2 Boundary integral equation

We may now use the reciprocal theorem to derive the boundary integral equation. Let us again take $\{\mu, p, \mathbf{u}, \boldsymbol{\sigma}\}$ and $\{\tilde{\mu}, \tilde{p}, \tilde{\mathbf{u}}, \tilde{\boldsymbol{\sigma}}\}$ as two flows in the Stokes regime. This time, we pick one of them as the flow field due to a point force of arbitrary (and constant) strength $\tilde{\mathbf{F}}$ located at $\mathbf{x}_0$. Thus, we have

$$\tilde{\mathbf{u}}(\mathbf{x}) = \frac{1}{8\pi\tilde{\mu}}\tilde{\mathbf{F}} \cdot \mathbf{J}(\mathbf{x} - \mathbf{x}_0), \tag{2.18}$$

$$\tilde{\boldsymbol{\sigma}}(\mathbf{x}) = \frac{1}{8\pi}\tilde{\mathbf{F}} \cdot \mathbf{K}(\mathbf{x} - \mathbf{x}_0). \tag{2.19}$$

We note that $\mathbf{J}$ and $\mathbf{K}$ are singular at $\mathbf{x} = \mathbf{x_0}$. Thus, the reciprocal theorem given in Eq. (2.17) is no longer valid over the full domain $\mathcal{B}$. To resolve this singularity, we define a new spherical domain $\mathcal{B}_\epsilon$ of vanishingly small radius ϵ enclosing the singular point $\mathbf{x}_0$ at its center. Now, the reciprocal theorem for the regular domain $\mathcal{B} - \mathcal{B}_\epsilon$ can be written as

$$\tilde{\mu}\int_{\partial\mathcal{B}-\partial\mathcal{B}_\epsilon} \mathbf{n}(\mathbf{x}) \cdot \boldsymbol{\sigma}(\mathbf{x}) \cdot \tilde{\mathbf{u}}(\mathbf{x}) \mathrm{d}S(\mathbf{x}) = \mu \int_{\partial\mathcal{B}-\partial\mathcal{B}_\epsilon} \mathbf{n}(\mathbf{x}) \cdot \tilde{\boldsymbol{\sigma}}(\mathbf{x}) \cdot \mathbf{u}(\mathbf{x}) \mathrm{d}S(\mathbf{x}), \tag{2.20}$$

and decomposed to

$$\begin{aligned} &-\tilde{\mu}\int_{\partial\mathcal{B}_\epsilon} \mathbf{n}(\mathbf{x}) \cdot \boldsymbol{\sigma}(\mathbf{x}) \cdot \tilde{\mathbf{u}}(\mathbf{x}) \mathrm{d}S(\mathbf{x}) + \mu \int_{\partial\mathcal{B}_\epsilon} \mathbf{n}(\mathbf{x}) \cdot \tilde{\boldsymbol{\sigma}}(\mathbf{x}) \cdot \mathbf{u}(\mathbf{x}) \mathrm{d}S(\mathbf{x}) \\ &= \tilde{\mu}\int_{\partial\mathcal{B}} \mathbf{n}(\mathbf{x}) \cdot \boldsymbol{\sigma}(\mathbf{x}) \cdot \tilde{\mathbf{u}}(\mathbf{x}) \mathrm{d}S(\mathbf{x}) - \mu \int_{\partial\mathcal{B}} \mathbf{n}(\mathbf{x}) \cdot \tilde{\boldsymbol{\sigma}}(\mathbf{x}) \cdot \mathbf{u}(\mathbf{x}) \mathrm{d}S. \end{aligned} \tag{2.21}$$

Now by using Eqs. (2.18) and (2.19) and discarding the arbitrarily chosen $\tilde{\mathbf{F}}$ from the both sides, we find

$$\begin{aligned} &-\int_{\partial\mathcal{B}_\epsilon} \mathbf{n}_\epsilon(\mathbf{x}) \cdot \boldsymbol{\sigma}(\mathbf{x}) \cdot \mathbf{J}(\mathbf{x} - \mathbf{x}_0) \, \mathrm{d}S + \mu \int_{\partial\mathcal{B}_\epsilon} \mathbf{n}_\epsilon(\mathbf{x}) \mathbf{u}(\mathbf{x}) : \mathbf{K}(\mathbf{x} - \mathbf{x}_0) \, \mathrm{d}S \\ &= \int_{\partial\mathcal{B}} \mathbf{n}(\mathbf{x}) \cdot \boldsymbol{\sigma}(\mathbf{x}) \cdot \mathbf{J}(\mathbf{x} - \mathbf{x}_0) \, \mathrm{d}S - \mu \int_{\partial\mathcal{B}} \mathbf{n}(\mathbf{x}) \mathbf{u}(\mathbf{x}) : \mathbf{K}(\mathbf{x} - \mathbf{x}_0) \, \mathrm{d}S. \end{aligned} \tag{2.22}$$

As $\epsilon \to 0$, $\boldsymbol{\sigma}(\mathbf{x})$ and $\mathbf{u}(\mathbf{x})$ on the left-hand side of Eq. (2.22) tend to $\boldsymbol{\sigma}(\mathbf{x}_0)$ and $\mathbf{u}(\mathbf{x}_0)$, respectively. Over $\partial\mathcal{B}_\epsilon$, we can write $\mathbf{x}-\mathbf{x}_0 = \epsilon\mathbf{n}_\epsilon$ and

$$\mathbf{J}(\mathbf{x}-\mathbf{x}_0) = \frac{\mathbf{I}}{\epsilon} + \frac{\mathbf{n}_\epsilon\mathbf{n}_\epsilon}{\epsilon}, \tag{2.23}$$

$$\mathbf{K}(\mathbf{x}-\mathbf{x}_0) = \frac{-6\mathbf{n}_\epsilon\mathbf{n}_\epsilon\mathbf{n}_\epsilon}{\epsilon^2}. \tag{2.24}$$

The left-hand side of Eq. (2.22) is then reduced to

$$\begin{aligned}
&-\int_{\partial\mathcal{B}_\epsilon} \mathbf{n}_\epsilon(\mathbf{x})\cdot\boldsymbol{\sigma}(\mathbf{x})\cdot\mathbf{J}(\mathbf{x}-\mathbf{x}_0)\,\mathrm{d}S + \mu\int_{\partial\mathcal{B}_\epsilon} \mathbf{n}_\epsilon(\mathbf{x})\mathbf{u}(\mathbf{x}) : \mathbf{K}(\mathbf{x}-\mathbf{x}_0)\,\mathrm{d}S \\
&= -\boldsymbol{\sigma}(\mathbf{x}_0) : \int_{\partial\mathcal{B}_\epsilon} \frac{\mathbf{n}_\epsilon\mathbf{I}+\mathbf{n}_\epsilon\mathbf{n}_\epsilon\mathbf{n}_\epsilon}{\epsilon}\mathrm{d}S - 6\mu\mathbf{u}(\mathbf{x}_0)\cdot\int_{\partial\mathcal{B}_\epsilon}\frac{\mathbf{n}_\epsilon\mathbf{n}_\epsilon}{\epsilon^2}\mathrm{d}S, \\
&= -8\pi\mu\mathbf{u}(\mathbf{x}_0).
\end{aligned} \tag{2.25}$$

Substituting Eq. (2.25) to (2.22), we finally arrive at the boundary integral equation as

$$\mathbf{u}(\mathbf{x}_0) = -\frac{1}{8\pi\mu}\int_{\partial\mathcal{B}} \mathbf{n}(\mathbf{x})\cdot\boldsymbol{\sigma}(\mathbf{x})\cdot\mathbf{J}(\mathbf{x}_0-\mathbf{x})\,\mathrm{d}S - \frac{1}{8\pi}\int_{\partial\mathcal{B}} \mathbf{n}(\mathbf{x})\mathbf{u}(\mathbf{x}) : \mathbf{K}(\mathbf{x}_0-\mathbf{x})\,\mathrm{d}S. \tag{2.26}$$

Equation (2.26) provides the flow field at an arbitrary point $\mathbf{x}_0$, using Oseen tensor $\mathbf{J}$ and its associated stress tensor $\mathbf{K}$ over the boundary $\partial\mathcal{B}$. In the next chapter, we show how one can use the boundary integral equation to express the flow field of active particles in viscous fluids.

Chapter 3

Higher-order force moments of active particles [1]

3.1 Introduction

Self-propulsion is ubiquitous in nature. Be it at the macroscopic scale of flying birds or the microscopic scale of swimming bacteria, the motion of active matter results from converting internal or ambient energy into mechanical work without any other external input [162]. At sufficiently small scales in viscous fluids, inertia is irrelevant and viscous dissipation dominates the motion of the fluid and active particles within it [84]. In the absence of inertia, 'reciprocal' body distortions are ineffective as a propulsion mechanism, and so active particles must propel themselves by other means in this realm [157]. There exist several techniques to achieve net locomotion in the low-Reynolds-number regime [106, 109, 138]. For instance, microorganisms such as *Paramecium* and *Volvox* use small appendages called cilia to facilitate motion [124]. Cilia generate thrust through a coordinated pattern of beating, which may arise from hydrodynamic [22, 136, 141] or basal [100, 159, 196] interactions. Propulsion can also be achieved synthetically by chemically-active particles with asymmetric non-uniform surface properties [2, 72, 194]. In both of these examples, the effect of surface activity is confined to a narrow

[1] A version of this chapter has been published [137].

region surrounding the particle and hence may be modeled using 'apparent' slip velocities on the surface. This way, one can explicitly find the propulsion speed and thereby the disturbance flow field, in terms of prescribed (or measured) slip velocities [54].

For the inertialess motion of sufficiently small particles in viscous fluids, the flow field is often approximated by far-field singularity solutions of the Stokes equations. To leading order, the flow field decays linearly by distance ($\sim 1/|\mathbf{x}|$) and, at this level of approximation, the particle is replaced by a point force (i.e., zeroth-order force moment) that leads to flow [98]. The next-order correction to the flow field, which decays quadratically ($\sim 1/|\mathbf{x}|^2$), can be expressed using a force-dipole (i.e., first-order force moment), which is decomposed into a torque (the antisymmetric part) and a stresslet (the symmetric part) [10]. In the absence of an external force, the over-damped motion of the particle has no net hydrodynamic force or torque and so the stresslet governs the leading-order flow field. The importance of the stresslet in characterizing the interactions of active particles [13, 76, 108], the rheology [168] and stability [169] of active suspensions, and the collective locomotion of bacteria [40] is well documented. However, the stresslet term alone fails to explain behaviors such as the 'dancing' of two *Volvox* colonies when they are in proximity of one another [41], or the vortices induced due to the motion of *C. reinhardtii* [42, 75]. An emerging picture is that modeling the motion using only terms up to the stresslet may limit understanding of how active particles interact with their environment and motivates investigation of higher-order force moments. In a recent study, Ghose and Adhikari [61] showed that the swirling motion of an active spherical particle only appears in the flow field decaying as $\sim 1/|\mathbf{x}|^3$ and $\sim 1/|\mathbf{x}|^4$ and derived expressions for higher-order force moments of a sphere. In this chapter, we generalize their results by investigating the effects of higher-order force moments on an arbitrarily-shaped active particle, thereby extending recent general results for the stresslet term by Lauga and Michelin [108]. Using the boundary integral equations, we express the flow field around an active particle through a multipole expansion up to the contribution of the second-order force moments. We then provide explicit formulas for these force moments by exploiting the reciprocal theorem using a framework developed in [50].

The reciprocal theorem for low-Reynolds-number hydrodynamics has long been

an avenue to simplify calculations in Stokes flow [84, 86, 111, 161]. Its application has ranged from the inertialess jet propulsion [178], to boundary-driven channel flow [131], to Marangoni motion of a droplet covered with bulk-insoluble surfactants in a Poiseuille flow [147]. In particular, Stone and Samuel [184] showed that the kinematics of an active particle can be determined explicitly, using the flow field induced by the rigid-body motion of a passive particle of the same instantaneous shape. Subsequently, the reciprocal theorem has been widely used to determine the kinematics of active particles both in Newtonian [49, 109] and non-Newtonian fluids [35, 36, 105, 107, 146]. This approach was recently extended to determine the stresslet of active particles [108]. More recently, a general framework has been developed for finding the force moments (of any order) of an active particle in a Newtonian (or non-Newtonian) fluid [50]. Following that approach, in this chapter, we provide formulas for calculating the force moments up to the second order, for any arbitrarily-shaped active particle.

The chapter is organized as follows. In Section 3.2, we employ the boundary integral equation to describe the disturbance flow field caused by an active particle. Using an asymptotic expansion of the far-field flow, we show how the force moments contribute to the disturbance flow field. We then in Section 3.3, use the reciprocal theorem to find general expressions for these force moments and, as examples, evaluate them explicitly for a spherical active particle, a generalized squirmer and an active slender rod.

3.2 Multipole expansion

We consider a particle with boundary $\partial\mathcal{B}$ in an otherwise unbounded Newtonian fluid of viscosity μ and background flow field $\mathbf{u}^\infty$, as shown in Fig. 3.1. Using the boundary integral equations, the disturbance flow field $\mathbf{u}' = \mathbf{u} - \mathbf{u}^\infty$ can be expressed as a summation of *single-layer* and *double-layer* potentials [98, 154]

$$\mathbf{u}'(\mathbf{x}) = -\frac{1}{8\pi\mu}\int_{\partial\mathcal{B}} \mathbf{f}'(\mathbf{y})\cdot\mathbf{J}(\mathbf{x}-\mathbf{y})\mathrm{d}S(\mathbf{y}) - \frac{1}{8\pi}\int_{\partial\mathcal{B}} \mathbf{u}'(\mathbf{y})\mathbf{n}(\mathbf{y}) : \mathbf{K}(\mathbf{x}-\mathbf{y})\mathrm{d}S(\mathbf{y}), \tag{3.1}$$

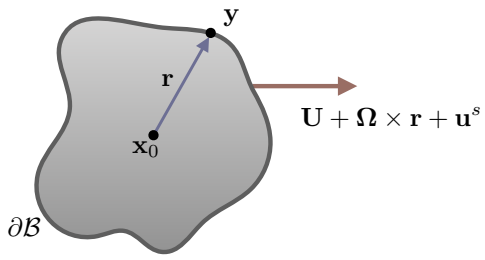

Figure 3.1: Schematic representation of an active particle of arbitrary shape. A point on the particle surface, $\partial\mathcal{B}$, is denoted by $\mathbf{y}$ and $\mathbf{x}_0$ is a convenient reference point in the body. The instantaneous velocity of a point on $\partial\mathcal{B}$ is given by rigid-body translation $\mathbf{U}$, rigid-body rotation $\boldsymbol{\Omega}\times\mathbf{r}$ and surface slip velocity $\mathbf{u}^s$.

where $\mathbf{f}'=\mathbf{n}\cdot\boldsymbol{\sigma}'$ is the traction of disturbance stress tensor $\boldsymbol{\sigma}'$, $\mathbf{y}$ is the position that is integrated over the particle surface and $\mathbf{n}$ is the surface normal pointing into the fluid. Here $\mathbf{J}(\mathbf{x})=\frac{\mathbf{I}}{|\mathbf{x}|}+\frac{\mathbf{xx}}{|\mathbf{x}|^3}$ is the Green's function of Stokes equations (or the Oseen tensor) and $\mathbf{K}(\mathbf{x})=\frac{-6\mathbf{xxx}}{|\mathbf{x}|^5}$ is its associated stress tensor. Expanding in $\mathbf{y}$ about a convenient point in the body $\mathbf{x}_0$ (for example the center of mass),

$$\mathbf{J}(\mathbf{x}-\mathbf{y})=\mathbf{J}(\mathbf{x}-\mathbf{x}_0)-\mathbf{r}\cdot\boldsymbol{\nabla}\mathbf{J}(\mathbf{x}-\mathbf{x}_0)+\frac{1}{2}\mathbf{rr}:\boldsymbol{\nabla}\boldsymbol{\nabla}\mathbf{J}(\mathbf{x}-\mathbf{x}_0)+\cdots, \tag{3.2}$$

$$\mathbf{K}(\mathbf{x}-\mathbf{y})=\mathbf{K}(\mathbf{x}-\mathbf{x}_0)-\mathbf{r}\cdot\boldsymbol{\nabla}\mathbf{K}(\mathbf{x}-\mathbf{x}_0)+\cdots, \tag{3.3}$$

where $\mathbf{r}=\mathbf{y}-\mathbf{x}_0$. Equation (3.1) then takes the form

$$\begin{aligned}\mathbf{u}'(\mathbf{x})=&-\frac{1}{8\pi\mu}\left[\langle\mathbf{f}'\rangle\cdot\mathbf{J}(\mathbf{x}-\mathbf{x}_0)-\langle\mathbf{f}'\mathbf{r}\rangle:\boldsymbol{\nabla}\mathbf{J}(\mathbf{x}-\mathbf{x}_0)+\frac{1}{2}\langle\mathbf{f}'\mathbf{rr}\rangle\odot\boldsymbol{\nabla}\boldsymbol{\nabla}\mathbf{J}(\mathbf{x}-\mathbf{x}_0)+\cdots\right]\\&-\frac{1}{8\pi}\left[\langle\mathbf{u}'\mathbf{n}\rangle:\mathbf{K}(\mathbf{x}-\mathbf{x}_0)-\langle\mathbf{u}'\mathbf{nr}\rangle\odot\boldsymbol{\nabla}\mathbf{K}(\mathbf{x}-\mathbf{x}_0)+\cdots\right].\end{aligned} \tag{3.4}$$

For convenience, in this chapter, we denote the surface integral by $\int_{\partial\mathcal{B}}\cdots\mathrm{d}S\equiv\langle\cdots\rangle$. We also use $\odot$ to denote a $k-$fold contraction where $k=\min\{a,b\}$ and a and b are the tensorial orders of the contracted tensors, e.g., $[\langle\mathbf{u}'\mathbf{nr}\rangle\odot\boldsymbol{\nabla}\mathbf{K}]_i=\left\langle u'_j n_k r_m\right\rangle\nabla_m K_{kji}$. We define $\mathbf{u}'(\mathbf{x})=\sum_{i=1}\mathbf{u}'^{(\mathrm{i})}(\mathbf{x})$, where $\mathbf{u}'^{(\mathrm{i})}(\mathbf{x})$ is the flow field that decays as $|\mathbf{x}|^{-i}$. At leading order, one can recognize the net hydrodynamic force $\mathbf{F}=\langle\mathbf{f}'\rangle$ as the

zeroth-order force moment. The presence of particle at this order is represented by a point force of strength $-\mathbf{F}$ and the flow field is simply governed by a Stokeslet,

$$\mathbf{u}'^{(1)}(\mathbf{x}) = -\frac{1}{8\pi\mu}\mathbf{F}\cdot\mathbf{J}(\mathbf{x}-\mathbf{x}_0). \tag{3.5}$$

To find the flow field decaying as $|\mathbf{x}|^{-2}$, it is useful to decompose $\mathbf{f}'\mathbf{r}$ and $\mathbf{u}'\mathbf{n}$, to their symmetric and antisymmetric parts as $\mathbf{f}'\mathbf{r} = \frac{\mathbf{f}'\mathbf{r}+\mathbf{r}\mathbf{f}'}{2} + \frac{\mathbf{f}'\mathbf{r}-\mathbf{r}\mathbf{f}'}{2}$ and $\mathbf{u}'\mathbf{n} = \frac{\mathbf{u}'\mathbf{n}+\mathbf{n}\mathbf{u}'}{2} + \frac{\mathbf{u}'\mathbf{n}-\mathbf{n}\mathbf{u}'}{2}$. Noting the symmetry of $\mathbf{K}(\mathbf{x})$ and also recalling

$$\nabla_k J_{ij} = \frac{x_i\delta_{jk} + x_j\delta_{ik} - x_k\delta_{ij}}{(x_l x_l)^{\frac{3}{2}}} - \frac{3x_i x_j x_k}{(x_l x_l)^{\frac{5}{2}}}, \tag{3.6}$$

we have

$$\begin{aligned}
\mathbf{u}'^{(2)}(\mathbf{x}) &= -\frac{1}{8\pi\mu}\Bigg[\left\langle \mathbf{r}\times\mathbf{f}'\right\rangle\cdot\mathbf{C}(\mathbf{x}-\mathbf{x}_0) \\
&\quad -\frac{1}{2}\left\langle \frac{\mathbf{f}'\mathbf{r}+\mathbf{r}\mathbf{f}'}{2} - \frac{1}{3}(\mathbf{f}'\cdot\mathbf{r})\mathbf{I} - \mu\left(\mathbf{u}'\mathbf{n}+\mathbf{n}\mathbf{u}'\right)\right\rangle : \mathbf{K}(\mathbf{x}-\mathbf{x}_0)\Bigg], \\
&= -\frac{1}{8\pi\mu}\left[\mathbf{L}\cdot\mathbf{C}(\mathbf{x}-\mathbf{x}_0) - \frac{1}{2}\mathbf{S} : \mathbf{K}(\mathbf{x}-\mathbf{x}_0)\right],
\end{aligned} \tag{3.7}$$

where $\mathbf{L} = \langle \mathbf{r}\times\mathbf{f}'\rangle$ is the antisymmetric first-order force moment, i.e. torque and $\mathbf{C}(\mathbf{x}) = \frac{\mathbf{I}\times\mathbf{x}}{|\mathbf{x}|^3}$ is the associated rotlet (or couplet) tensor [155]. In using the cross product, we follow the convention $[\mathbf{r}\times\mathbf{f}']_i = \epsilon_{ijk}r_j f'_k$ and $[\mathbf{I}\times\mathbf{r}]_{ij} = \epsilon_{jsk}\delta_{is}r_k$, where $\boldsymbol{\epsilon}$ is the third-order permutation tensor. The symmetric and deviatoric first-order force moment (i.e. $\overline{\mathbf{f}'\mathbf{r}}$) along with the contribution of the double-layer potential lead to $\mathbf{S} = \left\langle \overline{\mathbf{f}'\mathbf{r}} - 2\mu\,\overline{\mathbf{u}'\mathbf{n}}\right\rangle$, namely the stresslet [10]. The over-bracket denotes the

fully-symmetric and deviatoric part of a tensor which are defined

$$\begin{aligned}
\overline{[\ ]}_{ij} &= (1/2)([\ ]_{ij} + [\ ]_{ji}) - (1/3)[\ ]_{ss}\delta_{ij},\\
\overline{[\ ]}_{ijk} &= (1/6)\Big([\ ]_{ijk} + [\ ]_{ikj} + [\ ]_{jik} + [\ ]_{jki} + [\ ]_{kij} + [\ ]_{kji}\Big)\\
&\quad - (1/15)\Big\{([\ ]_{ssi} + [\ ]_{sis} + [\ ]_{iss})\,\delta_{kj} + \Big([\ ]_{ssj} + [\ ]_{sjs} + [\ ]_{jss}\Big)\delta_{ik}\\
&\quad + ([\ ]_{ssk} + [\ ]_{sks} + [\ ]_{kss})\,\delta_{ij}\Big\},
\end{aligned} \tag{3.8}$$

for the second and third-order tensors, respectively.

To determine the flow field decaying as $|\mathbf{x}|^{-3}$, we decompose the third-order tensors $\mathbf{f}'\mathbf{r}\mathbf{r}$ and $\mathbf{u}'\mathbf{n}\mathbf{r}$ to their irreducible parts (see [4, 5] for the decomposition technique). Now by taking the second gradient of the Oseen tensor

$$\begin{aligned}
\nabla_m\nabla_k J_{ij} = &\frac{\delta_{im}\delta_{jk} + \delta_{jm}\delta_{ik} - \delta_{km}\delta_{ij}}{(x_l x_l)^{\frac{3}{2}}} + \frac{15x_i x_j x_k x_m}{(x_l x_l)^{\frac{7}{2}}}\\
&- \frac{3\Big(x_m x_i\delta_{jk} + x_j x_m\delta_{ik} - x_k x_m\delta_{ij} + x_j x_k\delta_{im} + x_i x_k\delta_{jm} + x_i x_j\delta_{km}\Big)}{(x_l x_l)^{\frac{5}{2}}},
\end{aligned} \tag{3.9}$$

we obtain the next order correction for the flow field

$$\begin{aligned}
\mathbf{u}'^{(3)}(\mathbf{x}) = &-\frac{1}{32\pi\mu}\left[\left\langle\overline{\mathbf{f}'\mathbf{r}\mathbf{r}} - 4\mu\,\overline{\mathbf{u}'\mathbf{n}\mathbf{r}}\right\rangle \odot \boldsymbol{\nabla}\mathbf{K}(\mathbf{x}-\mathbf{x}_0)\right]\\
&- \frac{1}{24\pi\mu}\left[\left\langle\overline{\mathbf{r}(\mathbf{r}\times\mathbf{f}')}\right\rangle : \boldsymbol{\nabla}[\boldsymbol{\nabla}\times\mathbf{J}(\mathbf{x}-\mathbf{x}_0)]\right] - \frac{1}{80\pi\mu}\Big[\Big\langle 2|\mathbf{r}|^2\mathbf{f}' - (\mathbf{r}\cdot\mathbf{f}')\mathbf{r}\\
&+ 3\mu\left[4(\mathbf{u}'\cdot\mathbf{n})\mathbf{r} - (\mathbf{u}'\cdot\mathbf{r})\mathbf{n} - (\mathbf{r}\cdot\mathbf{n})\mathbf{u}'\right]\Big\rangle\cdot\nabla^2\mathbf{J}(\mathbf{x}-\mathbf{x}_0)\Big].
\end{aligned} \tag{3.10}$$

We may then identify stresslet dipole $\mathbf{S}_{\mathcal{D}} = \left\langle\overline{\mathbf{f}'\mathbf{r}\mathbf{r}} - 4\mu\,\overline{\mathbf{u}'\mathbf{n}\mathbf{r}}\right\rangle$, rotlet dipole $\mathbf{C}_{\mathcal{D}} = \left\langle\overline{\mathbf{r}(\mathbf{r}\times\mathbf{f}')}\right\rangle$ and potential dipole

$$\mathbf{d} = \Big\langle 2|\mathbf{r}|^2\mathbf{f}' - (\mathbf{r}\cdot\mathbf{f}')\mathbf{r} + 3\mu\left[4(\mathbf{u}'\cdot\mathbf{n})\mathbf{r} - (\mathbf{u}'\cdot\mathbf{r})\mathbf{n} - (\mathbf{r}\cdot\mathbf{n})\mathbf{u}'\right]\Big\rangle.$$

Finally, we find the flow field around the particle that decays slower than $|\mathbf{x}|^{-4}$ as

$$\mathbf{u}'(\mathbf{x}) = -\frac{1}{8\pi\mu}\Bigg[\mathbf{F}\cdot\mathbf{J}(\mathbf{x}-\mathbf{x}_0) + \mathbf{L}\cdot\mathbf{C}(\mathbf{x}-\mathbf{x}_0) - \frac{1}{2}\mathbf{S}:\mathbf{K}(\mathbf{x}-\mathbf{x}_0) + \frac{1}{4}\mathbf{S}_{\mathcal{D}}\odot\boldsymbol{\nabla}\mathbf{K}(\mathbf{x}-\mathbf{x}_0) - \mathbf{C}_{\mathcal{D}}:\boldsymbol{\Upsilon}(\mathbf{x}-\mathbf{x}_0) + \frac{1}{10}\mathbf{d}\cdot\nabla^2\mathbf{J}(\mathbf{x}-\mathbf{x}_0)\Bigg], \tag{3.11}$$

where

$$\Upsilon_{ijk} = \frac{\epsilon_{iks}x_s x_j + \epsilon_{jks}x_s x_i}{(x_l x_l)^{\frac{5}{2}}}, \tag{3.12}$$

is the tensor associated with the rotlet dipole.

Introducing a more compact notation through

$$\begin{aligned}\mathsf{S} &= [\mathbf{F},\mathbf{L},\mathbf{S},\mathbf{S}_{\mathcal{D}},\mathbf{C}_{\mathcal{D}},\mathbf{d},\cdots],\\ &= \Bigg[\langle\mathbf{f}'\rangle, \langle\mathbf{r}\times\mathbf{f}'\rangle, \Big\langle\overline{\mathbf{f}'\mathbf{r}} - 2\mu\,\overline{\mathbf{u}'\mathbf{n}}\Big\rangle, \Big\langle\overline{\mathbf{f}'\mathbf{r}\mathbf{r}} - 4\mu\,\overline{\mathbf{u}'\mathbf{n}\mathbf{r}}\Big\rangle, \Big\langle\overline{\mathbf{r}(\mathbf{r}\times\mathbf{f}')}\Big\rangle,\\ &\quad \Big\langle 2|\mathbf{r}|^2\mathbf{f}' - (\mathbf{r}\cdot\mathbf{f}')\mathbf{r} + 3\mu\big[4(\mathbf{u}'\cdot\mathbf{n})\mathbf{r} - (\mathbf{u}'\cdot\mathbf{r})\mathbf{n} - (\mathbf{r}\cdot\mathbf{n})\mathbf{u}'\big]\Big\rangle, \cdots\Bigg],\end{aligned} \tag{3.13}$$

and

$$\mathsf{J} = \Big[\mathbf{J},\mathbf{C},(-1/2)\mathbf{K},(1/4)\boldsymbol{\nabla}\mathbf{K},-\boldsymbol{\Upsilon},(1/10)\nabla^2\mathbf{J},\cdots\Big], \tag{3.14}$$

we obtain

$$\mathbf{u}'(\mathbf{x}) = -\frac{1}{8\pi\mu}\mathsf{S}\odot\mathsf{J}. \tag{3.15}$$

We note in particular that

$$\mathsf{S} = \mathsf{F}' + \mu\langle\mathsf{D}'\rangle, \tag{3.16}$$

represents the strengths of the multipoles of J which contains force moments from

the single-layer integral,

$$\mathsf{F}' = \left[\langle \mathbf{f}' \rangle, \langle \mathbf{r} \times \mathbf{f}' \rangle, \left\langle \overline{\mathbf{r}\mathbf{f}'} \right\rangle, \left\langle \overline{\mathbf{r}\mathbf{r}\mathbf{f}'} \right\rangle, \left\langle \overline{\mathbf{r}(\mathbf{r} \times \mathbf{f}')} \right\rangle, \left\langle 2|\mathbf{r}|^2 \mathbf{f}' - (\mathbf{r} \cdot \mathbf{f}')\mathbf{r} \right\rangle, \cdots \right], \tag{3.17}$$

and terms due to surface disturbance velocity from the double-layer,

$$\mathsf{D}' = \left[\mathbf{0}, \mathbf{0}, -2\overline{\mathbf{n}\mathbf{u}'}, -4\overline{\mathbf{u}'\mathbf{n}\mathbf{r}}, \mathbf{0}, 12(\mathbf{u}' \cdot \mathbf{n})\mathbf{r} - 3(\mathbf{u}' \cdot \mathbf{r})\mathbf{n} - 3(\mathbf{r} \cdot \mathbf{n})\mathbf{u}', \cdots \right]. \tag{3.18}$$

Finally, we note $\mathsf{S} = \mathsf{S}'$ because all terms in S^{∞} are zero as the boundary integral equation vanishes identically in that case [154].

To summarize, the second-order force moment is decomposed into a rotlet dipole, a stresslet dipole and a potential dipole, with contributions from the double-layer potentials. To better understand the physical interpretation of these force moments, consider an active particle that propels itself forward using flagella (e.g., *E. coli*). The force exerted by the flagella is completely balanced by the drag force on the body and since the distribution of these two forces is separated in position (e.g., tail and head), the induced flow field is captured by a stresslet. However, the length scales of the cell body and the flagella differ, often by orders of magnitude, and so this asymmetry gives rise to a stresslet dipole. For a case wherein flagella use rotation to generate thrust, the cell body must counter-rotate to maintain the torque-free motion thereby generating a rotlet dipole. Finally, the finite size of the cell body accounts for the presence of a potential dipole (further discussion may be found in Refs. [175, 179]).

We should emphasize that the multipole expansion given in (3.15) is valid for an active (or passive) particle of any arbitrary shape, in a viscous fluid. Given that J is generic for any unbounded single particle, determining the flow field is reduced to finding the strengths S. Thus, both traction $\mathbf{f}'$ and disturbance surface velocity $\mathbf{u}'(\mathbf{x} \in \partial\mathcal{B})$ are needed. Although the latter may be explicitly prescribed (e.g., through slip velocity), finding the traction generally requires solving the flow field in full. However, one can avoid such calculations by using the Lorentz reciprocal theorem for the Stokes flow [49, 108, 184] to calculate *moments* of $\mathbf{f}'$. In the following, we employ the general framework given in [50] to find the force moments and hence the multipole strengths S. Recovering the expressions for force,

torque and stresslet, we report explicit formulas for the stresslet dipole, rotlet dipole and potential dipole for an arbitrarily-shaped active particle.

3.3 Evaluating the force moments of an active particle

We are interested in the motion of an active particle with boundary conditions

$$\mathbf{u}\left(\mathbf{x} \in \partial\mathcal{B}\right) = \mathbf{U} + \boldsymbol{\Omega} \times \mathbf{r} + \mathbf{u}^{s}, \tag{3.19}$$

where $\mathbf{U}$ and $\boldsymbol{\Omega}$ are the rigid-body translation and rotation of the particle while $\mathbf{u}^{s}$ is a velocity due to surface activity, such as diffusiophoretic slip or a swimming gait [52, 130]. As a dual (or auxiliary) problem, here denoted by a hat, we take the passive motion of a rigid body of the same instantaneous shape,

$$\hat{\mathbf{u}}\left(\mathbf{x} \in \partial\mathcal{B}\right) = \hat{\mathbf{U}} + \hat{\boldsymbol{\Omega}} \times \mathbf{r}. \tag{3.20}$$

The reciprocal theorem indicates that the virtual power of the motion of these two bodies is equal [84], namely

$$\hat{\mu}\left\langle \mathbf{n} \cdot \boldsymbol{\sigma}' \cdot \hat{\mathbf{u}}' \right\rangle = \mu \left\langle \mathbf{n} \cdot \hat{\boldsymbol{\sigma}}' \cdot \mathbf{u}' \right\rangle, \tag{3.21}$$

where $\hat{\mathbf{u}}' = \hat{\mathbf{u}} - \hat{\mathbf{u}}^{\infty}$ and $\hat{\boldsymbol{\sigma}}' = \hat{\boldsymbol{\sigma}} - \hat{\boldsymbol{\sigma}}^{\infty}$ are the disturbance flow and stress field for the auxiliary problem, respectively. As we will show below, by using (operators of) the dual problem, the force moments of the active particle may be obtained without resolution of neither the disturbance field $\mathbf{u}'$ nor traction $\mathbf{f}'$.

Following Elfring [50], we expand the background flow of the auxiliary problem around a point in the body $\mathbf{x}_0$ as

$$\hat{\mathbf{u}}^{\infty}(\mathbf{x} \in \partial\mathcal{B}) = \hat{\mathbf{U}}^{\infty}\left(\mathbf{x}_0\right) + \mathbf{r} \cdot \boldsymbol{\nabla}\hat{\mathbf{u}}^{\infty}\left(\mathbf{x}_0\right) + \frac{1}{2}\mathbf{r}\mathbf{r} : \boldsymbol{\nabla}\boldsymbol{\nabla}\hat{\mathbf{u}}^{\infty}\left(\mathbf{x}_0\right) + \cdots, \tag{3.22}$$

which by decomposing $\boldsymbol{\nabla}\hat{\mathbf{u}}^{\infty}$ and $\boldsymbol{\nabla}\boldsymbol{\nabla}\hat{\mathbf{u}}^{\infty}$ to their irreducible parts, can be rewritten

$$\begin{aligned}\hat{\mathbf{u}}^{\infty}(\mathbf{x} \in \partial\mathcal{B}) =& \hat{\mathbf{U}}^{\infty} + \hat{\boldsymbol{\Omega}}^{\infty} \times \mathbf{r} + \mathbf{r} \cdot \hat{\mathbf{E}}^{\infty} \\ &+ \mathbf{r}\mathbf{r} : \hat{\boldsymbol{\Gamma}}^{\infty} + (\boldsymbol{\epsilon} \cdot \mathbf{r})\,\mathbf{r} : \hat{\boldsymbol{\Lambda}}^{\infty} + \left(2|\mathbf{r}|^{2}\mathbf{I} - \mathbf{r}\mathbf{r}\right) \cdot \hat{\mathbf{e}}^{\infty} + \cdots.\end{aligned} \tag{3.23}$$

Here, $\hat{\mathbf{U}}^\infty$ and $\hat{\mathbf{\Omega}}^\infty$ indicate the translation and rotation of the background flow of the auxiliary problem at $\mathbf{x}_0$. $\hat{\mathbf{E}}^\infty = \overline{\boldsymbol{\nabla}\hat{\mathbf{u}}^\infty}$ and $\hat{\mathbf{\Gamma}}^\infty = (1/2)\overline{\boldsymbol{\nabla}\boldsymbol{\nabla}\hat{\mathbf{u}}^\infty}$ are the fully symmetric and deviatoric ($\hat{E}^\infty_{ii} = 0$, $\hat{\Gamma}^\infty_{iij} = \hat{\Gamma}^\infty_{iji} = \hat{\Gamma}^\infty_{jii} = 0$) second and third-order tensors, respectively. $\hat{\mathbf{\Lambda}}^\infty = \overline{\boldsymbol{\nabla}(\boldsymbol{\nabla}\times\hat{\mathbf{u}}^\infty)}$ is a second-order symmetric tensor and $\hat{\mathbf{e}}^\infty = (1/10)\nabla^2\hat{\mathbf{u}}^\infty$. Using this expansion and relying on the linearity of the Stokes equations, we can write

$$\hat{p}' = \hat{\mu}\hat{\mathbf{P}}\odot\hat{\mathbf{U}}', \tag{3.24}$$

$$\hat{\mathbf{u}}' = \hat{\mathbf{G}}\odot\hat{\mathbf{U}}', \tag{3.25}$$

$$\hat{\boldsymbol{\sigma}}' = \hat{\mu}\hat{\mathbf{T}}\odot\hat{\mathbf{U}}', \tag{3.26}$$

$$\hat{\mathbf{f}}' = -\hat{\mathbf{R}}\odot\hat{\mathbf{U}}', \tag{3.27}$$

wherein the velocity gradients

$$\hat{\mathbf{U}}' = \left[\hat{\mathbf{U}} - \hat{\mathbf{U}}^\infty, \hat{\mathbf{\Omega}} - \hat{\mathbf{\Omega}}^\infty, -\hat{\mathbf{E}}^\infty, -\hat{\mathbf{\Gamma}}^\infty, -\hat{\mathbf{\Lambda}}^\infty, -\hat{\mathbf{e}}^\infty, \cdots\right], \tag{3.28}$$

are linearly mapped to the disturbance pressure, velocity, and stress fields by

$$\hat{\mathbf{P}} = \left[\hat{\mathbf{P}}_U, \hat{\mathbf{P}}_\Omega, \hat{\mathbf{P}}_E, \hat{\mathbf{P}}_\Gamma, \hat{\mathbf{P}}_\Lambda, \hat{\mathbf{P}}_e, \cdots\right], \tag{3.29}$$

$$\hat{\mathbf{G}} = \left[\hat{\mathbf{G}}_U, \hat{\mathbf{G}}_\Omega, \hat{\mathbf{G}}_E, \hat{\mathbf{G}}_\Gamma, \hat{\mathbf{G}}_\Lambda, \hat{\mathbf{G}}_e, \cdots\right], \tag{3.30}$$

$$\hat{\mathbf{T}} = \left[\hat{\mathbf{T}}_U, \hat{\mathbf{T}}_\Omega, \hat{\mathbf{T}}_E, \hat{\mathbf{T}}_\Gamma, \hat{\mathbf{T}}_\Lambda, \hat{\mathbf{T}}_e, \cdots\right], \tag{3.31}$$

which are functions of the position in space and the geometry of the particle and each term maintains the symmetry of the term, against which it operates. $\hat{\mathbf{R}}$ is the grand resistance tensor that linearly maps velocity moments to force moments in the dual problem. The symmetry of the stress tensor implies that all components of $\hat{\mathbf{T}}$ are symmetric in their first two (or non-contracted) indices. Under these definitions, the reciprocal theorem can be rewritten as

$$\left\langle(\mathbf{n}\cdot\boldsymbol{\sigma}')\cdot\hat{\mathbf{G}}\right\rangle\odot\hat{\mathbf{U}}' = \mu\left\langle\mathbf{u}'\cdot\left(\mathbf{n}\cdot\hat{\mathbf{T}}\right)\right\rangle\odot\hat{\mathbf{U}}'. \tag{3.32}$$

Importantly, given the boundary condition of the dual problem and the decomposition of the background field, we know the terms in the operator $\hat{\mathbf{G}}(\mathbf{x}\in\partial\mathcal{B})$ on the

boundary of the particle, which may be defined as

$$\hat{G}_{U,ij} = \delta_{ij}, \tag{3.33}$$

$$\hat{G}_{\Omega,ij} = \epsilon_{ijs} r_s, \tag{3.34}$$

$$\hat{G}_{E,ijk} = \overbrace{\delta_{ij} r_k}^{jk}, \tag{3.35}$$

$$\hat{G}_{\Gamma,ijkm} = \overbrace{\delta_{ij} r_k r_m}^{jkm}, \tag{3.36}$$

$$\hat{G}_{\Lambda,ijk} = \overbrace{\epsilon_{ijs} r_s r_k}^{jk}, \tag{3.37}$$

$$\hat{G}_{e,ijkm} = 2\delta_{ij} r_s r_s - r_i r_j, \tag{3.38}$$

$$\vdots$$

where the over-brackets are identical to (3.8) but only operate over the specified indices. In this way, the operator acts precisely to map the traction $\mathbf{f}' = \mathbf{n} \cdot \boldsymbol{\sigma}'$ to the force moments

$$\mathsf{F}' = \left\langle \mathbf{f}' \cdot \hat{\mathsf{G}} \right\rangle = \left[\langle \mathbf{f}' \rangle, \langle \mathbf{r} \times \mathbf{f}' \rangle, \left\langle \overbrace{\mathbf{r}\mathbf{f}'}^{} \right\rangle, \left\langle \overbrace{\mathbf{f}'\mathbf{r}\mathbf{r}}^{} \right\rangle, \left\langle \overbrace{\mathbf{r}(\mathbf{r} \times \mathbf{f}')}^{} \right\rangle, \left\langle 2|\mathbf{r}|^2 \mathbf{f}' - (\mathbf{r} \cdot \mathbf{f}')\mathbf{r} \right\rangle, \cdots \right]. \tag{3.39}$$

Now, given that $\hat{\mathsf{U}}'$ is arbitrarily chosen, we may discard it from both sides of Eq. (3.32). Applying the boundary conditions on $\mathbf{u}'$, and also expressing the rigid body translation and rotation as $\mathsf{U} = [\mathbf{U}, \boldsymbol{\Omega}, \mathbf{0}, \cdots]$, Eq. (3.32) can be reduced to [50]

$$\mathsf{F}' = -\frac{\mu}{\hat{\mu}} \hat{\mathsf{R}} \odot \mathsf{U} + \mu \left\langle (\mathbf{u}^s - \mathbf{u}^\infty) \cdot \left(\mathbf{n} \cdot \hat{\mathsf{T}} \right) \right\rangle. \tag{3.40}$$

Then by way of (3.16), one obtains the multipole strengths as

$$\mathsf{S} = -\frac{\mu}{\hat{\mu}} \hat{\mathsf{R}} \odot \mathsf{U} + \mu \left\langle (\mathbf{u}^s - \mathbf{u}^\infty) \cdot \left(\mathbf{n} \cdot \hat{\mathsf{T}} \right) + \mathsf{D}' \right\rangle, \tag{3.41}$$

where the double-layer potential contribution,

$$\mathsf{D}' = \Big[\mathbf{0}, \mathbf{0}, -2\overline{\mathbf{n}\,(\mathbf{u}^s - \mathbf{u}^\infty)}, -4\overline{(\mathbf{u}^s - \mathbf{u}^\infty)\,\mathbf{n}\mathbf{r}}, \mathbf{0},$$
$$12\,[(\mathbf{u}^s - \mathbf{u}^\infty)\cdot\mathbf{n}]\,\mathbf{r} - 3\,[(\mathbf{u}^s - \mathbf{u}^\infty)\cdot\mathbf{r}]\,\mathbf{n} - 3(\mathbf{r}\cdot\mathbf{n})\,(\mathbf{u}^s - \mathbf{u}^\infty), \cdots\Big], \quad (3.42)$$

is simplified as the terms associated with rigid-body motion integrate to zero [154].

Equation (3.41) provides the tensorial relationship between the boundary motion and the strength of multipoles for any arbitrarily-shaped active particle in Stokes flow. We note that the multipole strengths are split into terms arising from the rigid-body motion of the particle, U, and those associated with the (disturbance) surface activity $\mathbf{u}^s - \mathbf{u}^\infty$. Using this equation, one can derive explicit formulas for S provided $\hat{\mathsf{T}}$ is known, as we illustrate in the following.

We begin with $\mathbf{F}$ and $\mathbf{L}$. In self-propulsion, in the absence of any external force and torque, the net force and torque on the particle are strictly zero. However, to find the net translational and rotational velocity (which are unknown at this point), we may use the reciprocal theorem for the force and torque. Upon setting $\mathbf{F} = \mathbf{0}$ and $\mathbf{L} = \mathbf{0}$ in Eq. (3.41), we may solve for U directly

$$\begin{bmatrix} \mathbf{U} \\ \boldsymbol{\Omega} \end{bmatrix} = \frac{\hat{\mu}}{\mu}\begin{pmatrix} \hat{\mathbf{R}}_{FU} & \hat{\mathbf{R}}_{LU} \\ \hat{\mathbf{R}}_{F\Omega} & \hat{\mathbf{R}}_{L\Omega} \end{pmatrix}^{-1} \cdot \begin{bmatrix} \mathbf{F}^s \\ \mathbf{L}^s \end{bmatrix}, \quad (3.43)$$

where $\hat{\mathbf{R}}_{FU} = -\hat{\mu}\left\langle \mathbf{n}\cdot\hat{\mathbf{T}}_U \right\rangle$, $\hat{\mathbf{R}}_{F\Omega} = -\hat{\mu}\left\langle \mathbf{n}\cdot\hat{\mathbf{T}}_\Omega \right\rangle$, $\hat{\mathbf{R}}_{LU} = -\hat{\mu}\left\langle \mathbf{r}\times\left(\mathbf{n}\cdot\hat{\mathbf{T}}_U\right)\right\rangle$ and $\hat{\mathbf{R}}_{L\Omega} = -\hat{\mu}\left\langle \mathbf{r}\times\left(\mathbf{n}\cdot\hat{\mathbf{T}}_\Omega\right)\right\rangle$ are the components of the grand resistance tensor $\hat{\mathsf{R}}$ associated with rigid-body motion. Here $\mathbf{F}^s = \mu\left\langle (\mathbf{u}^s - \mathbf{u}^\infty)\cdot\left(\mathbf{n}\cdot\hat{\mathbf{T}}_U\right)\right\rangle$ is the hydrodynamic force arising solely from the surface activities (often referred to as the *thrust*) and $\mathbf{L}^s = \mu\left\langle (\mathbf{u}^s - \mathbf{u}^\infty)\cdot\left(\mathbf{n}\cdot\hat{\mathbf{T}}_\Omega\right)\right\rangle$ is surface activity driven torque. Equation (3.43) simply illustrates the balance between the force and torque generated by the surface activities and the hydrodynamic drag.

We may now determine other components of S by using (3.41) at higher orders.

We obtain

$$\mathbf{S} = -\frac{\mu}{\hat{\mu}}\left(\hat{\mathbf{R}}_{SU}\cdot\mathbf{U} + \hat{\mathbf{R}}_{S\Omega}\cdot\boldsymbol{\Omega}\right) + \mathbf{S}^{s}, \tag{3.44}$$

$$\mathbf{S}_{\mathcal{D}} = -\frac{\mu}{\hat{\mu}}\left(\hat{\mathbf{R}}_{S_{\mathcal{D}}U}\cdot\mathbf{U} + \hat{\mathbf{R}}_{S_{\mathcal{D}}\Omega}\cdot\boldsymbol{\Omega}\right) + \mathbf{S}^{s}_{\mathcal{D}}, \tag{3.45}$$

$$\mathbf{C}_{\mathcal{D}} = -\frac{\mu}{\hat{\mu}}\left(\hat{\mathbf{R}}_{C_{\mathcal{D}}U}\cdot\mathbf{U} + \hat{\mathbf{R}}_{C_{\mathcal{D}}\Omega}\cdot\boldsymbol{\Omega}\right) + \mathbf{C}^{s}_{\mathcal{D}}, \tag{3.46}$$

$$\mathbf{d} = -\frac{\mu}{\hat{\mu}}\left(\hat{\mathbf{R}}_{dU}\cdot\mathbf{U} + \hat{\mathbf{R}}_{d\Omega}\cdot\boldsymbol{\Omega}\right) + \mathbf{d}^{s}, \tag{3.47}$$

where the resistance tensors may be written in terms of $\hat{\mathsf{T}}$ as follows

$$\hat{R}_{SU,ijk} = -\hat{\mu}\left\langle \overbrace{n_s \hat{T}_{U,sik} r_j}^{ij} \right\rangle, \tag{3.48}$$

$$\hat{R}_{S\Omega,ijk} = -\hat{\mu}\left\langle \overbrace{n_s \hat{T}_{\Omega,sik} r_j}^{ij} \right\rangle, \tag{3.49}$$

$$\hat{R}_{S_{\mathcal{D}}U,ijkm} = -\hat{\mu}\left\langle \overbrace{n_s \hat{T}_{U,sim} r_j r_k}^{ijk} \right\rangle, \tag{3.50}$$

$$\hat{R}_{S_{\mathcal{D}}\Omega,ijkm} = -\hat{\mu}\left\langle \overbrace{n_s \hat{T}_{\Omega,sim} r_j r_k}^{ijk} \right\rangle, \tag{3.51}$$

$$\hat{R}_{C_{\mathcal{D}}U,ijk} = -\hat{\mu}\left\langle \overbrace{n_s \hat{T}_{U,snk} \epsilon_{jmn} r_i r_m}^{ij} \right\rangle, \tag{3.52}$$

$$\hat{R}_{C_{\mathcal{D}}\Omega,ijk} = -\hat{\mu}\left\langle \overbrace{n_s \hat{T}_{\Omega,snk} \epsilon_{jmn} r_i r_m}^{ij} \right\rangle, \tag{3.53}$$

$$\hat{R}_{dU,ij} = -\hat{\mu}\left\langle 2n_s \hat{T}_{U,sij} r_l r_l - n_s \hat{T}_{U,smj} r_m r_i \right\rangle, \tag{3.54}$$

$$\hat{R}_{d\Omega,ij} = -\hat{\mu}\left\langle 2n_s \hat{T}_{\Omega,sij} r_l r_l - n_s \hat{T}_{\Omega,smj} r_m r_i \right\rangle, \tag{3.55}$$

and the contributions of the surface activities are likewise

$$\mathbf{S}^s = \mu\left\langle \overline{(\mathbf{u}^s - \mathbf{u}^\infty)\mathbf{n} : \hat{\mathbf{T}}_E} - 2\overline{(\mathbf{u}^s - \mathbf{u}^\infty)\mathbf{n}} \right\rangle, \tag{3.56}$$

$$\mathbf{S}^s_{\mathcal{D}} = \mu\left\langle \overline{(\mathbf{u}^s - \mathbf{u}^\infty)\mathbf{n} : \hat{\mathbf{T}}_\Gamma} - 4\overline{(\mathbf{u}^s - \mathbf{u}^\infty)\mathbf{n}\mathbf{r}} \right\rangle, \tag{3.57}$$

$$\mathbf{C}^s_{\mathcal{D}} = \mu\left\langle \overline{(\mathbf{u}^s - \mathbf{u}^\infty)\mathbf{n} : \hat{\mathbf{T}}_\Lambda} \right\rangle, \tag{3.58}$$

$$\begin{aligned}\mathbf{d}^s = \mu\Big\langle & (\mathbf{u}^s - \mathbf{u}^\infty)\mathbf{n} : \hat{\mathbf{T}}_e + 12\left[\mathbf{n}\cdot(\mathbf{u}^s - \mathbf{u}^\infty)\right]\mathbf{r} - 3\left[\mathbf{r}\cdot(\mathbf{u}^s - \mathbf{u}^\infty)\right]\mathbf{n} \\ & - 3(\mathbf{r}\cdot\mathbf{n})(\mathbf{u}^s - \mathbf{u}^\infty)\Big\rangle.\end{aligned} \tag{3.59}$$

We should emphasize that all components of $\hat{\mathbf{T}}$ are unique for a given particle geometry. Therefore by finding them once, we can determine the force moments for any prescribed surface activity provided the shape does not change.

3.3.1 Sphere

We now resolve the force moments of an active spherical particle, using the expressions reported in the previous section. We take $\mathbf{x}_0$ to be the center of the sphere $\mathbf{r} = a\mathbf{n}$, where a is the radius. Details of the auxiliary flow field and stress field corresponding to each force moment (i.e., $\hat{\mathsf{P}}$, $\hat{\mathsf{G}}$ and $\hat{\mathsf{T}}$) are reported in Appendix A.

Having $\hat{\mathbf{T}}_U$ and $\hat{\mathbf{T}}_\Omega$ at hand, the rigid-body resistance tensors can be evaluated. We find $\hat{\mathbf{R}}_{FU} = 6\pi\hat{\mu}a\mathbf{I}$, $\hat{\mathbf{R}}_{L\Omega} = 8\pi\hat{\mu}a^3\mathbf{I}$, $\hat{\mathbf{R}}_{dU} = 10\pi\hat{\mu}a^3\mathbf{I}$ and

$$\left[\hat{\mathbf{R}}_{F\Omega}, \hat{\mathbf{R}}_{LU}, \hat{\mathbf{R}}_{SU}, \hat{\mathbf{R}}_{S\Omega}, \hat{\mathbf{R}}_{S_{\mathcal{D}}U}, \hat{\mathbf{R}}_{S_{\mathcal{D}}\Omega}, \hat{\mathbf{R}}_{C_{\mathcal{D}}U}, \hat{\mathbf{R}}_{C_{\mathcal{D}}\Omega}, \hat{\mathbf{R}}_{d\Omega}\right] = \mathbf{0}.$$

The force and torque are respectively

$$\mathbf{F} = -6\pi a\mu\mathbf{U} - \frac{3\mu}{2a}\left\langle \mathbf{u}^s - \mathbf{u}^\infty \right\rangle = -6\pi a\mu\Big(\mathbf{U} - (1 + \frac{a^2}{6}\nabla^2)\mathbf{U}^\infty\Big) - \frac{3\mu}{2a}\left\langle \mathbf{u}^s \right\rangle, \tag{3.60}$$

$$\mathbf{L} = -8\pi a^3\mu\boldsymbol{\Omega} + 3\mu\left\langle (\mathbf{u}^s - \mathbf{u}^\infty)\times\mathbf{n} \right\rangle = -8\pi a^3\mu(\boldsymbol{\Omega} - \boldsymbol{\Omega}^\infty) + 3\mu\left\langle \mathbf{u}^s\times\mathbf{n} \right\rangle, \tag{3.61}$$

where $\mathbf{U}^\infty$ and $\boldsymbol{\Omega}^\infty$ are the velocity and rotation rate of the background flow at the center of the sphere. If the particle is passive, $\mathbf{u}^s = \mathbf{0}$, we recover Faxén's first and

second laws as expected. In the absence of an external force and torque, the rigid-body translation and rotation of spherical active particle with surface velocities $\mathbf{u}^s$ are given by

$$\mathbf{U} = -\frac{1}{4\pi a^2}\left\langle \mathbf{u}^s - \mathbf{u}^\infty \right\rangle, \tag{3.62}$$

$$\mathbf{\Omega} = -\frac{3}{8\pi a^4}\left\langle \mathbf{r} \times (\mathbf{u}^s - \mathbf{u}^\infty) \right\rangle, \tag{3.63}$$

as first shown by Anderson and Prieve [3] and later generalized [49, 184]. Using the expression for stresslet given in Eq. (3.44), we find

$$\begin{aligned} \mathbf{S} &= -5\mu \left\langle \overline{(\mathbf{u}^s - \mathbf{u}^\infty)\mathbf{n}} \right\rangle - \frac{2}{3}\mu \left\langle (\mathbf{u}^s - \mathbf{u}^\infty)\cdot \mathbf{n} \right\rangle \mathbf{I}, \\ &= \frac{20\pi\mu a^3}{3}\left(1 + \frac{a^2}{10}\nabla^2\right)\mathbf{E}^\infty - 5\mu \left\langle \overline{\mathbf{u}^s \mathbf{n}} \right\rangle - \frac{2}{3}\mu \left\langle \mathbf{u}^s \cdot \mathbf{n} \right\rangle \mathbf{I}, \end{aligned} \tag{3.64}$$

where $\mathbf{E}^\infty = \overline{\nabla \mathbf{u}^\infty(\mathbf{x}_0)}$. We note that this expression for the stresslet amends a typographical error in the results of Lauga and Michelin [108] (Eq. (10) in their reference). When the sphere is passive, Eq. (3.64) recovers Faxén's third law. By using $\hat{\mathbf{T}}_\Gamma$, we determine the stresslet dipole

$$\begin{aligned} \mathbf{S}_\mathcal{D} &= -\frac{35}{4}\mu a \left\langle \overline{(\mathbf{u}^s - \mathbf{u}^\infty)\,\mathbf{n}\mathbf{n}} \right\rangle, \\ &= \frac{14\mu\pi a^5}{3}\left(1 + \frac{a^2}{14}\nabla^2\right)\mathbf{\Gamma}^\infty - \frac{35}{4}\mu a \left\langle \overline{\mathbf{u}^s \mathbf{n}\mathbf{n}} \right\rangle, \end{aligned} \tag{3.65}$$

where $\mathbf{\Gamma}^\infty = (1/2)\overline{\nabla\nabla \mathbf{u}^\infty(\mathbf{x}_0)}$. The rotlet dipole is then similarly found

$$\begin{aligned} \mathbf{C}_\mathcal{D} &= 4\mu a \left\langle \overline{[(\mathbf{u}^s - \mathbf{u}^\infty)\times \mathbf{n}]\,\mathbf{n}} \right\rangle, \\ &= \frac{16\mu\pi a^5}{15}\mathbf{\Lambda}^\infty + 4\mu a \left\langle \overline{[\mathbf{u}^s \times \mathbf{n}]\,\mathbf{n}} \right\rangle, \end{aligned} \tag{3.66}$$

where $\boldsymbol{\Lambda}^{\infty} = \overline{\boldsymbol{\nabla}(\boldsymbol{\nabla}\times\mathbf{u}^{\infty})(\mathbf{x}_0)}$. Finally, for the potential dipole, we arrive at

$$\begin{aligned}\mathbf{d} &= -10\pi\mu a^3\mathbf{U} + \frac{15a\mu}{2}\langle 2[(\mathbf{u}^s-\mathbf{u}^{\infty})\cdot\mathbf{n}]\mathbf{n} - \mathbf{u}^s + \mathbf{u}^{\infty}\rangle,\\ &= -10\pi\mu a^3(\mathbf{U}-\mathbf{U}^{\infty}) + 30\mu\pi a^5\mathbf{d}^{\infty} + \frac{15a\mu}{2}\langle 2(\mathbf{u}^s\cdot\mathbf{n})\mathbf{n} - \mathbf{u}^s\rangle, \end{aligned} \tag{3.67}$$

with $\mathbf{d}^{\infty} = (1/10)\nabla^2\mathbf{u}^{\infty}(\mathbf{x}_0)$. In total, for a spherical active particle, we have

$$\begin{aligned}\mathbf{S} = \Bigg[&-6\pi a\mu\mathbf{U} - \frac{3\mu}{2a}\langle\mathbf{u}^s-\mathbf{u}^{\infty}\rangle, -8\pi a^3\mu\boldsymbol{\Omega} + 3\mu\langle(\mathbf{u}^s-\mathbf{u}^{\infty})\times\mathbf{n}\rangle,\\ &-5\mu\left\langle\overline{(\mathbf{u}^s-\mathbf{u}^{\infty})\mathbf{n}}\right\rangle - \frac{2}{3}\mu\langle(\mathbf{u}^s-\mathbf{u}^{\infty})\cdot\mathbf{n}\rangle\mathbf{I},\\ &-\frac{35}{4}\mu a\left\langle\overline{(\mathbf{u}^s-\mathbf{u}^{\infty})\mathbf{n}\mathbf{n}}\right\rangle, 4\mu a\left\langle\overline{[(\mathbf{u}^s-\mathbf{u}^{\infty})\times\mathbf{n}]\mathbf{n}}\right\rangle,\\ &-10\pi\mu a^3\mathbf{U} + \frac{15a\mu}{2}\langle 2[(\mathbf{u}^s-\mathbf{u}^{\infty})\cdot\mathbf{n}]\mathbf{n} - \mathbf{u}^s + \mathbf{u}^{\infty}\rangle, \cdots\Bigg]. \end{aligned} \tag{3.68}$$

3.3.2 Generalized squirmer

We now examine the expressions obtained above for the specific case of a sphere with purely tangential surface activity, i.e., a squirmer [16, 120, 145]. One may then express $\mathbf{u}^s = u^s_{\theta}\mathbf{e}_{\theta} + u^s_{\phi}\mathbf{e}_{\phi}$ in spherical coordinates (r,θ,ϕ) as [145]

$$\begin{aligned}u^s_{\theta} = \sum_{n=1}^{\infty}\sum_{m=0}^{n}\Bigg[&-\frac{2\sin\theta P_n^{m\prime}(\xi)}{na^{n+2}}\left(B_{mn}\cos m\phi + \tilde{B}_{mn}\sin m\phi\right)\\ &+\frac{mP_n^m(\xi)}{a^{n+1}\sin\theta}\left(\tilde{C}_{mn}\cos m\phi - C_{mn}\sin m\phi\right)\Bigg], \end{aligned} \tag{3.69}$$

$$\begin{aligned}u^s_{\phi} = \sum_{n=1}^{\infty}\sum_{m=0}^{n}\Bigg[&\frac{\sin\theta P_n^{m\prime}(\xi)}{a^{n+1}}\left(C_{mn}\cos m\phi + \tilde{C}_{mn}\sin m\phi\right)\\ &+\frac{2mP_n^m(\xi)}{na^{n+2}\sin\theta}\left(\tilde{B}_{mn}\cos m\phi - B_{mn}\sin m\phi\right)\Bigg], \end{aligned} \tag{3.70}$$

where $P_n^m(\xi)$ is a Legendre function of order m and degree n, and the prime in $P_n^{m\prime}(\xi)$ indicates differentiation with respect to $\xi = \cos\theta$. Here, $B_{mn}, \tilde{B}_{mn}, C_{mn}$ and

$\tilde{C}_{mn}$ are constant coefficients representing different modes of the surface activity. We find the net translational and rotational velocities in terms of these coefficients and Cartesian unit vectors $\mathbf{e}_x, \mathbf{e}_y$ and $\mathbf{e}_z$ as

$$\mathbf{U} = -\frac{4}{3a^3}\left(B_{01}\mathbf{e}_z - B_{11}\mathbf{e}_x - \tilde{B}_{11}\mathbf{e}_y\right), \tag{3.71}$$

$$\mathbf{\Omega} = -\frac{1}{a^3}\left(C_{01}\mathbf{e}_z - C_{11}\mathbf{e}_x - \tilde{C}_{11}\mathbf{e}_y\right). \tag{3.72}$$

Stresslet, stresslet dipole, rotlet dipole and potential dipole can be similarly determined

$$\begin{aligned}\mathbf{S} = -\frac{12\pi\mu}{a^2}\Big[&B_{02}\overline{\mathbf{e}_z\mathbf{e}_z} - 2B_{12}\overline{\mathbf{e}_x\mathbf{e}_z} - 2\tilde{B}_{12}\overline{\mathbf{e}_y\mathbf{e}_z} \\ &+ 2B_{22}\left(\overline{\mathbf{e}_x\mathbf{e}_x} - \overline{\mathbf{e}_y\mathbf{e}_y}\right) + 4\tilde{B}_{02}\overline{\mathbf{e}_x\mathbf{e}_y}\Big],\end{aligned} \tag{3.73}$$

$$\begin{aligned}\mathbf{S}_{\mathcal{D}} = -\frac{8\pi\mu}{a^2}\Big[&\frac{5}{3}B_{03}\overline{\mathbf{e}_z\mathbf{e}_z\mathbf{e}_z} + B_{13}\left(\overline{\mathbf{e}_x\mathbf{e}_y\mathbf{e}_y} - 4\overline{\mathbf{e}_x\mathbf{e}_z\mathbf{e}_z} + \overline{\mathbf{e}_x\mathbf{e}_x\mathbf{e}_x}\right) \\ &+ \tilde{B}_{13}\left(\overline{\mathbf{e}_y\mathbf{e}_x\mathbf{e}_x} - 4\overline{\mathbf{e}_y\mathbf{e}_z\mathbf{e}_z} + \overline{\mathbf{e}_y\mathbf{e}_y\mathbf{e}_y}\right) + 10B_{23}\left(\overline{\mathbf{e}_x\mathbf{e}_x\mathbf{e}_z} - \overline{\mathbf{e}_y\mathbf{e}_y\mathbf{e}_z}\right) \\ &+ 20\tilde{B}_{23}\overline{\mathbf{e}_x\mathbf{e}_y\mathbf{e}_z} + 10B_{33}\left(3\overline{\mathbf{e}_x\mathbf{e}_y\mathbf{e}_y} - \overline{\mathbf{e}_x\mathbf{e}_x\mathbf{e}_x}\right) - 10\tilde{B}_{33}\left(3\overline{\mathbf{e}_y\mathbf{e}_x\mathbf{e}_x} - \overline{\mathbf{e}_y\mathbf{e}_y\mathbf{e}_y}\right)\Big],\end{aligned} \tag{3.74}$$

$$\begin{aligned}\mathbf{C}_{\mathcal{D}} = -\frac{48\pi\mu}{5}\Big[&C_{02}\overline{\mathbf{e}_z\mathbf{e}_z} - 2C_{12}\overline{\mathbf{e}_x\mathbf{e}_z} - 2\tilde{C}_{12}\overline{\mathbf{e}_y\mathbf{e}_z} \\ &+ 2C_{22}\left(\overline{\mathbf{e}_x\mathbf{e}_x} - \overline{\mathbf{e}_y\mathbf{e}_y}\right) + 4\tilde{C}_{22}\overline{\mathbf{e}_x\mathbf{e}_y}\Big],\end{aligned} \tag{3.75}$$

$$\mathbf{d} = -\frac{80\pi\mu}{3}\left(B_{01}\mathbf{e}_z - B_{11}\mathbf{e}_x - \tilde{B}_{11}\mathbf{e}_y\right). \tag{3.76}$$

By only keeping B_{0n} and C_{0n} terms in Eqs. (3.69) and (3.70) and setting the other coefficients to zero, the solution reduces to the axisymmetric motion of a squirmer [145]. In this case, by symmetry, all the force moments generated by the surface activity are invariant by rotation with respect to $\mathbf{e}_z$. Thus, as one can see from (3.73) to (3.76), they must be of form $\mathbf{e}_z$, $\overline{\mathbf{e}_z\mathbf{e}_z}$, $\overline{\mathbf{e}_z\mathbf{e}_z\mathbf{e}_z}$, $\cdots$ which are the irreducible traceless rotation-invariant tensors of $\mathbf{e}_z$. The contribution of non-zero force moments of an axisymmetric squirmer to the flow field is illustrated in Fig. 3.2. Note that, to express the axisymmetric solutions in terms of tangential squirming modes B_n used in Lighthill [120] and Blake [16], one can simply set

$C_{0n} = 0$ and substitute B_{0n} by $-\frac{a^{n+2}}{n+1}B_n$ in Eqs. (3.71) to (3.76).

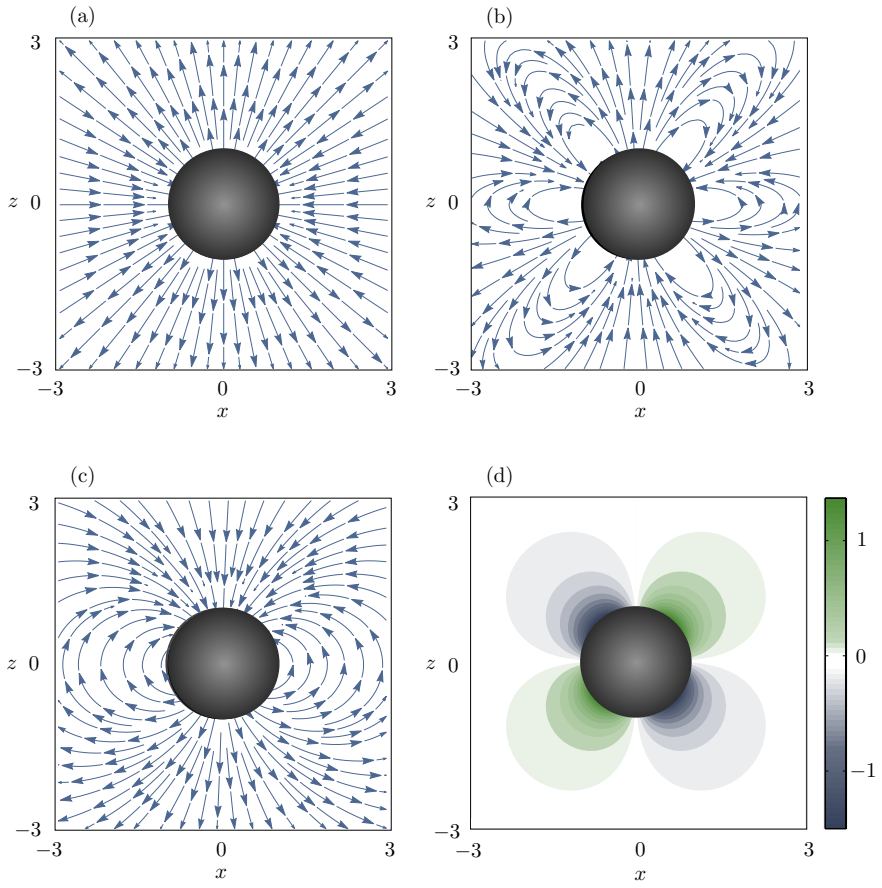

Figure 3.2: Flow fields induced by non-zero force moments of an axisymmetric squirmer of radius 1, using expressions given in (3.73) to (3.76): (a) Flow field due to a stresslet, for which we set $B_{02} = 1$ and other coefficients to zero. (b) Flow field due to a stresslet dipole with $B_{03} = 1$. (c) Flow field induced by a potential dipole with $B_{01} = 1$. (d) Flow field due to a rotlet dipole with $C_{02} = 1$. In (d), the color density indicates the magnitude of the velocity where positive (negative) values indicate flow into the plane (out of the plane) [145].

3.3.3 Axisymmetric slender rod

Let us now consider a slender rod, whose orientation is given by a unit vector $\mathbf{p}$, with an axisymmetric swimming gait along its length $\mathbf{u}^s = \alpha(s)\mathbf{p}$ in an otherwise quiescent fluid. Here s parameterizes (by arclength) the centerline of the rod, e.g. $s \in [-l/2, l/2]$ where l is the length.

To find the force moments, we first decompose a surface integral into an integration around the perimeter (denoted by R) in a plane with normal $\mathbf{p}$ and one over the length of the rod (denoted by s) so that $\langle \cdots \rangle = \langle \langle \cdots \rangle_R \rangle_s$. Using the resistive force theory for slender rods [109], we may approximate the force density per unit length

$$\langle \mathbf{n} \cdot \hat{\boldsymbol{\sigma}}' \rangle_R = -\left[\hat{\zeta}_{\parallel} \mathbf{pp} + \hat{\zeta}_{\perp} (\mathbf{I} - \mathbf{pp}) \right] \cdot \hat{\mathbf{u}}', \tag{3.77}$$

where $\hat{\zeta}_{\parallel}$ and $\hat{\zeta}_{\perp}$ are the parallel and perpendicular drag coefficients. Under this approximation, finding $\hat{\mathsf{T}}$ does not require details of the auxiliary flow field as we illustrate in the following. Recalling that $\hat{\mathbf{u}}' = \hat{\mathsf{G}} \odot \hat{\mathsf{U}}'$ and $\hat{\boldsymbol{\sigma}}' = \hat{\mu} \hat{\mathsf{T}} \odot \hat{\mathsf{U}}'$, one can write

$$\hat{\mu} \left\langle \mathbf{n} \cdot \hat{\mathsf{T}} \right\rangle = -\left\langle \left[\hat{\zeta}_{\parallel} \mathbf{pp} + \hat{\zeta}_{\perp} (\mathbf{I} - \mathbf{pp}) \right] \cdot \hat{\mathsf{G}} \right\rangle_s. \tag{3.78}$$

We note that $\hat{\mathsf{G}}(\mathbf{x} \in \partial\mathcal{B})$ is known from Eqs. (3.33) to (3.38).

To find the resistance tensors, from Eq. (3.78) we have

$$\hat{\mu} \left\langle \mathbf{n} \cdot \hat{\mathbf{T}}_U \right\rangle = -\left\langle \hat{\zeta}_{\parallel} \mathbf{pp} + \hat{\zeta}_{\perp} (\mathbf{I} - \mathbf{pp}) \right\rangle_s, \tag{3.79}$$

thus

$$\hat{\mathbf{R}}_{FU} = -\hat{\mu} \left\langle \mathbf{n} \cdot \hat{\mathbf{T}}_U \right\rangle = \left\langle \hat{\zeta}_{\parallel} \mathbf{pp} + \hat{\zeta}_{\perp} (\mathbf{I} - \mathbf{pp}) \right\rangle_s = \left[\hat{\zeta}_{\parallel} \mathbf{pp} + \hat{\zeta}_{\perp} (\mathbf{I} - \mathbf{pp}) \right] l. \tag{3.80}$$

Similarly, we find $\left[\hat{\mathbf{R}}_{F\Omega}, \hat{\mathbf{R}}_{LU}, \hat{\mathbf{R}}_{SU}, \hat{\mathbf{R}}_{S_{\mathcal{D}}\Omega}, \hat{\mathbf{R}}_{C_{\mathcal{D}}\Omega}, \hat{\mathbf{R}}_{d\Omega} \right] = \mathbf{0}, \hat{\mathbf{R}}_{L\Omega} = -\frac{l^3}{12} \hat{\zeta}_{\perp} (\mathbf{I} - \mathbf{pp})$,

$\hat{\mathbf{R}}_{dU} = \frac{l^3}{12}\left[\hat{\zeta}_{\parallel}\mathbf{pp} + 2\hat{\zeta}_{\perp}(\mathbf{I}-\mathbf{pp})\right]$ and

$$\hat{R}_{S\Omega,ijk} = \frac{l^3}{24}\hat{\zeta}_{\perp}\left(\epsilon_{iks}p_j + \epsilon_{jks}p_i\right)p_s, \tag{3.81}$$

$$\hat{R}_{C_{\mathcal{D}}U,ijk} = \frac{l^3}{24}\hat{\zeta}_{\perp}\left(p_i\epsilon_{kjm} + p_j\epsilon_{kim}\right)p_m, \tag{3.82}$$

$$\hat{R}_{S_{\mathcal{D}}U,ijkm} = \frac{l^3}{12}\left[\hat{\zeta}_{\parallel}\overbrace{p_ip_jp_k}p_m + \hat{\zeta}_{\perp}\left(\overbrace{\delta_{im}p_jp_k}^{ijk} - \overbrace{p_ip_jp_k}p_m\right)\right]. \tag{3.83}$$

Now to find S, we substitute (3.78) in (3.41). Noting that $\langle\mathsf{D}\rangle = \mathbf{0}$ since $\langle\mathbf{n}\rangle_R = \mathbf{0}$, we arrive at

$$\begin{aligned}\mathsf{S} &= -\frac{\mu}{\hat{\mu}}\hat{\mathsf{R}}\odot\mathsf{U} + \mu\left\langle\mathbf{u}^s\cdot\left(\mathbf{n}\cdot\hat{\mathsf{T}}\right)\right\rangle,\\ &= -\frac{\mu}{\hat{\mu}}\hat{\mathsf{R}}\odot\mathsf{U} - \left\langle\alpha\mathbf{p}\cdot\left[\zeta_{\parallel}\mathbf{pp} + \zeta_{\perp}(\mathbf{I}-\mathbf{pp})\right]\cdot\hat{\mathsf{G}}\right\rangle_s,\\ &= -\frac{\mu}{\hat{\mu}}\hat{\mathsf{R}}\odot\mathsf{U} - \zeta_{\parallel}\mathbf{p}\cdot\left\langle\alpha\hat{\mathsf{G}}\right\rangle_s.\end{aligned} \tag{3.84}$$

Note that $\zeta_{\parallel} = (\mu/\hat{\mu})\hat{\zeta}_{\parallel}$ and $\zeta_{\perp} = (\mu/\hat{\mu})\hat{\zeta}_{\perp}$. From this equation, we find $\mathbf{L}^s = \mathbf{0}$, $\mathbf{C}^s_{\mathcal{D}} = \mathbf{0}$ and

$$\mathbf{F}^s = -\zeta_{\parallel}\mathbf{p}\cdot\left\langle\alpha\hat{\mathbf{G}}_U\right\rangle_s = -\zeta_{\parallel}\langle\alpha\rangle_s\,\mathbf{p}, \tag{3.85}$$

$$\mathbf{S}^s = -\zeta_{\parallel}\mathbf{p}\cdot\left\langle\alpha\hat{\mathbf{G}}_E\right\rangle_s = -\zeta_{\parallel}\langle s\alpha\rangle_s\overbrace{\mathbf{pp}}, \tag{3.86}$$

$$\mathbf{S}^s_{\mathcal{D}} = -\zeta_{\parallel}\mathbf{p}\cdot\left\langle\alpha\hat{\mathbf{G}}_{\Gamma}\right\rangle_s = -\zeta_{\parallel}\left\langle s^2\alpha\right\rangle_s\overbrace{\mathbf{ppp}}, \tag{3.87}$$

$$\mathbf{d}^s = -\zeta_{\parallel}\mathbf{p}\cdot\left\langle\alpha\hat{\mathbf{G}}_e\right\rangle_s = -\zeta_{\parallel}\left\langle s^2\alpha\right\rangle_s\mathbf{p}, \tag{3.88}$$

which are in the form of irreducible traceless rotation-invariant tensors with regard to symmetry axis $\mathbf{p}$, as expected.

With no external force or torque acting on the rod, we can then determine the translational velocity

$$\mathbf{U} = -(1/l)\left\langle\mathbf{u}^s\right\rangle_s = -(1/l)\langle\alpha\rangle_s\mathbf{p}, \tag{3.89}$$

as also shown by Leshansky et al. [116]. Recalling that $\mathbf{L}^s = \mathbf{0}$, we find $\boldsymbol{\Omega} = \mathbf{0}$.

3.4 Conclusion

In this chapter, we investigated the effects of higher-order force moments on the flow field induced by an active particle. Using the boundary integral equations, we expressed the flow as a multipole expansion and decomposed the contribution of second-order force moments into a stresslet dipole, rotlet dipole and a potential dipole. Then, via the reciprocal theorem, we derived explicit formulas for these force moments which are valid for an active particle of arbitrary shape and then evaluated them for a spherical particle, a squirmer and an axisymmetric slender rod. We believe that by providing simple and explicit formulas for more accurate approximations of the flow-fields generated by active particles, we may enhance our understanding of how these particles interact with their surroundings. Given the generality of the employed framework, our results can be extended to capture the effect of third (or higher) order force moments and also can be adapted to study the hydrodynamic interactions between two [172] or many [148] active particles or active particles near boundaries [179, 185].

Chapter 4

Elastic swimmer near a wall

4.1 Introduction

Microorganisms often swim in complex trajectories when they are in proximity of obstacles. Some flagellated cells such as *E. coli* swim in circles of large radii near solid surfaces [12, 110], while some others like spermatozoa accumulate near the walls, when swimming in a confined setting [56, 118, 200]. It has also been observed that microswimmers can be entrapped by the nearby boundaries, swim alongside a wall for a long period of time [43], and then escape toward other obstacles [21, 182, 186]. Such nontrivial interactions between microorganisms and surfaces have been shown to contribute to biofilm formation [144, 156], pathogenic infection [85], and are also important in metabolite transportation [183].

In theory, the studies on the swimming trajectory of a microswimmer near a wall can be categorized into two groups: The swimmer is very close to the wall, hence lubrication equations govern the motion [9, 30], or its distance from the wall is large compared to its body size such that far-field approximations may be employed [13, 45, 117]. Although the latter relies on large distances from the wall, far-field hydrodynamics have shown to provide accurate results even at distances as small as a fraction of the cell body [180], and have been frequently utilized to explain interactions of a swimmer and nearby surfaces [38, 125, 181]. Based on this approximation, a wall reflects back the disturbance flow field caused by the swimmer and results in a force and a torque on the body [13]. Thus, the

wall presence is captured by the zeroth-order and first-order force moments of the reflected flow field. Depending on the geometry of the wall and the swimmer, and also the propulsion mechanism, the swimmer-wall interaction can lead to attraction or repulsion [13, 181]. However, this model cannot capture the effect of swimmer flexibility on its behavior near a wall. In particular, flagellum is elastic and its bending can significantly alter its hydrodynamic interactions [39, 199, 201]. In a computational study, Montenegro-Johnson et al. [132] showed that an elastic filament is scattered by around 5 to 10 degrees when swimming past a back-step in a microchannel. They found that depending on values of viscous forces and elastic forces, the swimmer may scatter toward the back-step or away from it. It has also been shown that a flagellum may buckle for reorientation [177], which stems from the elasticity of the flagellum [63, 202, 204] or the buckling of an elastic hook connecting the flagellum to the cell body [94, 139, 173]. In this chapter, by allowing the swimmer to bend from its connecting hook, we show that such reorientations occur naturally when the swimmer approaches a boundary. We show that effects of the elasticity of the swimmer is captured by the second-order force moments of the reflected flow field, namely the rotlet dipole. Then, using a minimal model, we demonstrate that elasticity prevents attraction by the wall for pusher-type swimmers, while it directs puller-type swimmers toward the wall.

4.2 Theoretical Framework

We consider an elastic swimmer located at $\mathbf{x}_0$. The motion of the swimmer is force and torque free, thus, the thrust (F^s) generated by the swimmer is completely balanced by the hydrodynamic drag (F^D)

$$\mathsf{F}^s + \mathsf{F}^D = \begin{bmatrix} \mathbf{F}^s \\ \mathbf{L}^s \end{bmatrix} + \begin{bmatrix} \mathbf{F}^D \\ \mathbf{L}^D \end{bmatrix} = \mathbf{0}, \tag{4.1}$$

where $\mathbf{F}^s$ and $\mathbf{L}^s$ are the driving force and torque, while $\mathbf{F}^D$ and $\mathbf{L}^D$ are the corresponding hydrodynamic drag and torque. The swimmer is elastic and deforms passively in response to a background flow. But, given the reported values for the typical bending rigidity of a swimmer [25, 135], we may employ a quasistatic assumption for its elastic bending. Thus, we can define the rigid-body motion

of the swimmer by $\mathsf{U} = [\mathbf{U}, \boldsymbol{\Omega}, \mathbf{0}, \cdots]$, where $\mathbf{U}$ and $\boldsymbol{\Omega}$ are the translational and rotational velocity. Due to presence of a wall, there exists a background flow field $\mathbf{u}^\infty(\mathbf{x})$. As shown in the previous chapter, at distances far from the swimmer, one can expand the background flow field around a point in the body of the swimmer (e.g., $\mathbf{x}_0$) as $\mathbf{u}^\infty = \mathsf{G} \odot \mathsf{U}^\infty$, where G is a linear operator mapping the velocity moments $\mathsf{U}^\infty = [\mathbf{U}^\infty, \boldsymbol{\Omega}^\infty, \mathbf{E}^\infty, \boldsymbol{\Gamma}^\infty, \boldsymbol{\Lambda}^\infty, \mathbf{e}^\infty, \cdots]$ to $\mathbf{u}^\infty$. In Chapter 3, we showed that $\mathbf{U}^\infty = \mathbf{u}^\infty(\mathbf{x}_0)$, $\boldsymbol{\Omega}^\infty = (1/2)\boldsymbol{\nabla} \times \mathbf{u}^\infty(\mathbf{x}_0)$, $\mathbf{E}^\infty = \overline{\boldsymbol{\nabla}\mathbf{u}^\infty(\mathbf{x}_0)}$, $\boldsymbol{\Gamma}^\infty = (1/2)\overline{\boldsymbol{\nabla}\boldsymbol{\nabla}\mathbf{u}^\infty(\mathbf{x}_0)}$, $\boldsymbol{\Lambda}^\infty = \overline{\boldsymbol{\nabla}[\boldsymbol{\nabla} \times \mathbf{u}^\infty(\mathbf{x}_0)]}$, and $\mathbf{e}^\infty = (1/10)\nabla^2\mathbf{u}^\infty(\mathbf{x}_0)$. Using this expansion, the hydrodynamic drag can be then written as

$$\mathsf{F}^D = -\mathsf{R} \odot (\mathsf{U} - \mathsf{U}^\infty), \tag{4.2}$$

where

$$\mathsf{R} = \begin{pmatrix} \mathbf{R}_{FU} & \mathbf{R}_{F\Omega} & \mathbf{R}_{FE} & \mathbf{R}_{F\Gamma} & \mathbf{R}_{F\Lambda} & \mathbf{R}_{Fe} & \cdots \\ \mathbf{R}_{LU} & \mathbf{R}_{L\Omega} & \mathbf{R}_{LE} & \mathbf{R}_{L\Gamma} & \mathbf{R}_{L\Lambda} & \mathbf{R}_{Le} & \cdots \end{pmatrix}, \tag{4.3}$$

contains all the resistance tensors associated with the force and torque. The velocity of the swimmer is thereby

$$\mathsf{U} = \mathsf{R}_{\mathsf{FU}}^{-1} \cdot \mathsf{F}^s - \mathsf{R}_{\mathsf{FU}}^{-1} \cdot \mathsf{R} \odot \mathsf{U}^\infty, \tag{4.4}$$

where

$$\mathsf{R}_{\mathsf{FU}} = \begin{pmatrix} \mathbf{R}_{FU} & \mathbf{R}_{F\Omega} \\ \mathbf{R}_{LU} & \mathbf{R}_{L\Omega} \end{pmatrix}, \tag{4.5}$$

is the rigid-body resistance tensor. Note that Eq. (4.4) provides the instantaneous velocity of the swimmer for any background flow, provided the resistance tensor is known.

Let us now further simplify the problem by considering an axisymmetric flagellated microorganism as our model swimmer, which propels forward by generating $\mathsf{F}^s = [f\hat{\mathbf{p}}, \mathbf{0}]^T$, where $\hat{\mathbf{p}}$ is a unit vector. We assume that the flagella (i.e., tail) and the cell body (i.e., head) are connected by an elastic hook which bends linearly in response to a torque dipole by the background flow (e.g., a torsional spring). We

define unit vector $\hat{\mathbf{r}}$ as the axis of symmetry of the swimmer in the absence of any background flow. Note that when there is no background flow (i.e., no wall), the thrust is aligned with the swimmer body $\hat{\mathbf{p}} = \hat{\mathbf{r}}$. The angle between $\hat{\mathbf{p}}$ and $\hat{\mathbf{r}}$ then characterizes the bending which can be defined as

$$\delta = \tan^{-1}\left(\frac{|\hat{\mathbf{r}} \times \hat{\mathbf{p}}|}{\hat{\mathbf{r}} \cdot \hat{\mathbf{p}}}\right). \tag{4.6}$$

But, how does the wall bend the swimmer? To answer this question, we need to further inspect the contribution of the background flow induced by the wall. The schematic of the effects of the background flow is illustrated in Fig. 4.1. $\mathbf{U}^\infty$ applies a force on the swimmer which is then balanced by the drag, thereby changing the translational velocity of the swimmer. Similarly, the vorticity of the background flow field $\boldsymbol{\Omega}^\infty$, exerts a torque that is balanced by the drag due to rotation. But, these forces and torques are not exerted on a single point on the swimmer body and, in fact, are non-uniformly distributed. $\mathbf{E}^\infty$ and $\boldsymbol{\Gamma}^\infty$ account for this effect by straining the swimmer due to the inequality of the forces between the head and tail. The finite size of the body gives rise to a potential dipole $\mathbf{e}^\infty$. Any difference in the torques across the body leads to a bending moment on the connecting elastic hook. This bending moment, which is a result of the rotlet dipole $\boldsymbol{\Lambda}^\infty$, is balanced by the torque due to bending of the hook as

$$k\delta \frac{\hat{\mathbf{r}} \times \hat{\mathbf{p}}}{|\hat{\mathbf{r}} \times \hat{\mathbf{p}}|} + \mathbf{R}_{L\Lambda} \cdot \boldsymbol{\Lambda}^\infty = \mathbf{0}, \tag{4.7}$$

where k is the bending rigidity of the hook. Due to this bending, the resistance tensor R changes but also we have $\hat{\mathbf{p}} \neq \hat{\mathbf{r}}$, thus from (4.4) we can determine the new swimming velocity. As finding R requires the details of the shape of the swimmer, in the following, using a toy model, we show how elastic bending of the swimmer alters the swimming trajectory near a wall.

4.3 Toy model

We now use a toy model to quantify the effects of elastic bending on interactions of a swimmer and a wall. At distances far from the swimmer, the leading-order

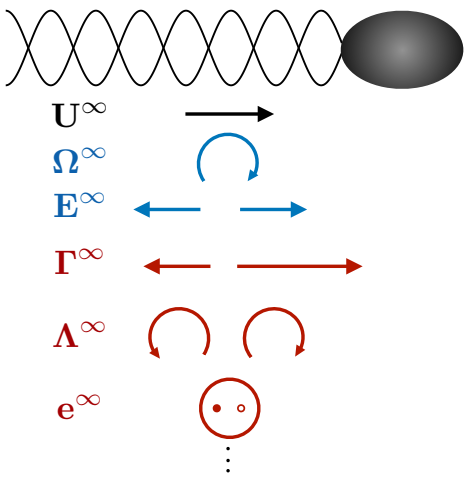

Figure 4.1: The effect of velocity moments of the background flow on a model swimmer. $\mathbf{U}^\infty$ is the zeroth-order velocity moment, $\mathbf{E}^\infty$ and $\boldsymbol{\Omega}^\infty$ are the first-order moments of the background flow, and $\boldsymbol{\Gamma}^\infty$, $\boldsymbol{\Lambda}^\infty$, and $\mathbf{e}^\infty$ together represent the second-order velocity moments.

flow field induced by force- and torque-free motion of the swimmer is captured by a symmetric force-dipole, whose strength depends on the swimmer geometry and its thrust-generating mechanism. When the swimmer generates impetus from its front end (e.g., *Chlamydomonas*), it is referred to as a puller, whereas in a pusher-type swimmer, thrust originates from the rear end (e.g., *E. coli*). Under this force-dipole approximation, the tail generates the driving force, which in turn is balanced completely by the drag force on the cell body (i.e., head). Here, we consider a two-sphere model, wherein spheres represent the head and the tail. Without any loss of generality, we assume sphere A generates the hydrodynamic thrust capturing the effect of the tail, while sphere B represents the head, as shown in Fig. 4.2. The flagella and cell body are separated in position, thus we take L as the characteristic distance between the head and tail (or the length scale of the swimmer). Furthermore, the length scales of the flagella and the cell body differ, and so we consider a_A and a_B as their characteristic sizes, noting that for a typical swimmer $a_A \ll a_B$. The swimmer is at distance h from the wall and we refer to the angle between $\hat{\mathbf{r}}$ and $\mathbf{e}_x$ as the swimming angle θ.

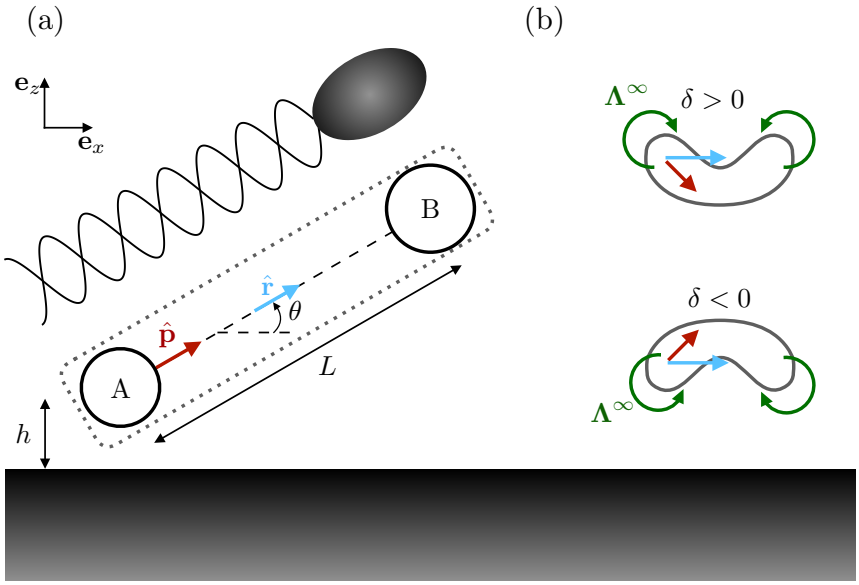

Figure 4.2: (a) Schematic of the considered swimmer. Spheres A and B represent the tail and the head, respectively. Sphere A is at distance h from the wall, L characterizes the swimmer length scale and θ is the swimming angle. (b) Bending mechanism of the swimmer by the rotlet dipole. The swimmer bends from its center with angle δ which is positive when the swimmer bends toward the wall and negative when it bends away.

We now scale lengths with L, velocities with U, forces with μLU and use $\mu L^2 U$ as the characteristic torque, where μ is the dynamic viscosity of the fluid. We non-dimensionalize all the terms using these characteristic values and henceforth refer to dimensionless quantities.

Using the far-field approximations, the flow field induced by each sphere can be modeled using a Stokeslet. To account for the presence of the wall, we may use an image Stokeslet of the same strength for each of the spheres. The no-slip condition at the wall is then satisfied by setting these image Stokeslets within the wall, at the same instantaneous distance as their corresponding particles. The background flow is then a summation of these two image Stokeslets. Calculating $\boldsymbol{\Lambda}^\infty$ using the Blake solution for image Stokeslets [17, 180], and also finding R for the deformed

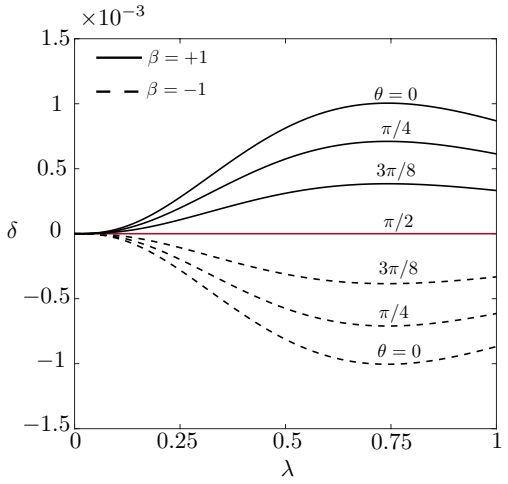

Figure 4.3: Variation of bending angle δ with respect to the ratio of radii λ, using the expression given in (4.8) with $f = 0.5$, $h(t = 0) = 10$ and $k = 10^{-4}$.

swimmer using the results of Chapter 3, we find the bending angle

$$\delta = \frac{8\beta f^4 \lambda^3 \cos\theta}{9kh^4 (1+\lambda)^3 (1+\lambda^3)}, \tag{4.8}$$

where $\lambda = \frac{a_A}{a_B}$. Here we use β to identify pushers and pullers as

$$\beta = \begin{cases} +1 & \text{pushers} \\ -1 & \text{pullers} \end{cases}. \tag{4.9}$$

In Fig. 4.3, we illustrate variation of the bending angle with respect to θ and λ. As the size of the tail increases (λ increses), the rotlet dipole becomes stronger and so does the bending angle. However, the resistance of the swimmer against bending also depends on the size of the tail. The competition between these two effects gives a rise to non-monotonic behavior of δ with respect to λ. We note that the elastic bending is maximized exactly when $\lambda = \frac{3}{4}$.

Now, noting that $\mathrm{d}h/\mathrm{d}t = \mathbf{U} \cdot \mathbf{e}_z$, $\mathrm{d}\theta/\mathrm{d}t = -\mathbf{\Omega} \cdot \mathbf{e}_y$, and using Eq. (4.4), we find

the time-evolution equation for h and θ as

$$\frac{\mathrm{d}h}{\mathrm{d}t} = \sin\theta + \frac{3\beta f}{16(1+\lambda)h^2}(1-3\cos 2\theta), \tag{4.10}$$

$$\frac{\mathrm{d}\theta}{\mathrm{d}t} = -\frac{3\beta f}{16(1+\lambda)h^3}\sin 2\theta + \frac{81\beta\lambda}{8192fh^3}(14\sin 2\theta - \sin 4\theta) + \frac{3\beta f^2\lambda^3}{8k(1+\lambda)^3(1+\lambda^3)h^4}\cos\theta. \tag{4.11}$$

We may first look into the limiting case where $k \to \infty$; the swimmer is rigid, hence $\delta = 0$. Defining θ_0 as the initial orientation angle, the thrust is pushing the swimmer toward the wall (when $\theta_0 < 0$) or away from it (when $\theta_0 > 0$). But, the hydrodynamic torque, exerted by the background flow, tries to reorient the swimmer. Depending on the *strength* of the hydrodynamic interactions and also the value of θ_0, this reorientation may qualitatively change the swimming direction (e.g., from repulsion to attraction). When $|\theta| \ll 1$, one can find the critical angle for such a change as $\theta_c = \frac{3\beta f}{8(1+\lambda)h_A^2}$ at which $\mathrm{d}h/\mathrm{d}t = 0$. When $\theta_0 > \theta_c$, we find $\mathrm{d}h/\mathrm{d}t > 0$. The swimmer thereby swims away from the wall, almost linearly, since the background flow correction to the swimming speed decays quadratically by h, and so $\mathrm{d}h/\mathrm{d}t \approx \sin\theta$. Similarly, $\theta_0 < \theta_c$ indicates that $\mathrm{d}h/\mathrm{d}t < 0$, thus pushers and pullers are both attracted by the wall, as illustrated in Fig. 4.4.

We now allow the swimmer to bend and begin with the behavior of pushers. When $\beta = 1$, the bending angle is positive, thus the swimmer bends toward the wall. The realignment of the head and tail caused by this bending, exerts an 'elastohydrodynamic' torque which is in the direction of $-\mathbf{e}_y$. We should emphasize that, this elastohydrodynamic torque is generated due to the bending of the swimmer. In this specific example, one finds $\mathbf{R}_{LU} = 6\pi(a_A + a_B)\hat{\mathbf{r}}\times\mathbf{I}$. Recalling that $\mathbf{F}^s = f\hat{\mathbf{p}}$, and also noting $\hat{\mathbf{p}} \neq \hat{\mathbf{r}}$ due to bending, we have $\mathbf{R}_{LU}\cdot\mathbf{F}^s \neq \mathbf{0}$ indicating that the thrust itself exerts a torque on the body which is the elastohydrodynamic torque.

For $\theta_0 > \theta_c$, the elastic bending enhances the repulsion of pushers by the wall. When $\theta_0 < \theta_c$, as the body gets closer to the wall, the elastohydrodynamic torque becomes more dominant (since it decays faster), and so at certain value of h, the swimmer escapes the wall with an equilibrium angle that balances these two torques. This behavior indicates that, regardless of the values of λ and θ_0 (except

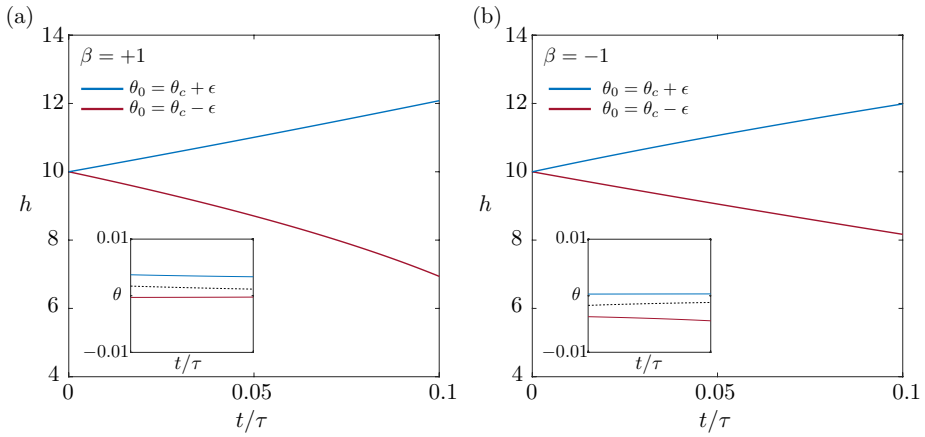

Figure 4.4: Evolution of h and θ (inset) for rigid (a) pushers and (b) pullers using expressions (4.10) and (4.11) evaluated at $h(t = 0) = 10$, $\lambda = 0.1$, $f = 0.5$ and $k \to \infty$. For each case, the initial swimming angles are $\theta_c \pm \epsilon$ where $\theta_c = 0.0017\beta$ is the initial critical angle and $\epsilon = 0.002$. The dotted line in the insets indicate the critical angle and $\tau = 16h^3(t = 0)/(3f)$ is the characteristic timescale.

for $\theta_0 = -\pi/2$), elastic pushers repel the wall. Expectedly, at higher values of λ, the effect of elasticity becomes stronger, thus the swimmer escapes the wall faster, as shown in Fig. 4.5.

Conversely, for pullers, δ is negative and the elastohydrodynamic torque acts in $+\mathbf{e}_y$, directing the swimmer toward the wall. Thus, for $\theta_0 < \theta_c$, elasticity strengthens the attraction. As illustrated in Fig. 4.6(a) and (b), for $\theta_0 > \theta_c$, the swimmer is initially propelling away, then it changes direction due to elastic bending and eventually swims toward the wall. It should be noted that, the increase of h due to the initial repulsion, weakens the effects of elastohydrodynamic torque. Thus, as shown in Fig. 4.6(c), for higher values of θ_0 and smaller λ, the elastic bending may not be able to overcome the hydrodynamic torque and the swimmer escapes. Unlike the elastic pushers wherein introducing elasticity guaranteed a repulsion, for elastic pullers, depending on the values of the initial angle and also the ratio of the radii, the swimmer either goes toward or away from the wall.

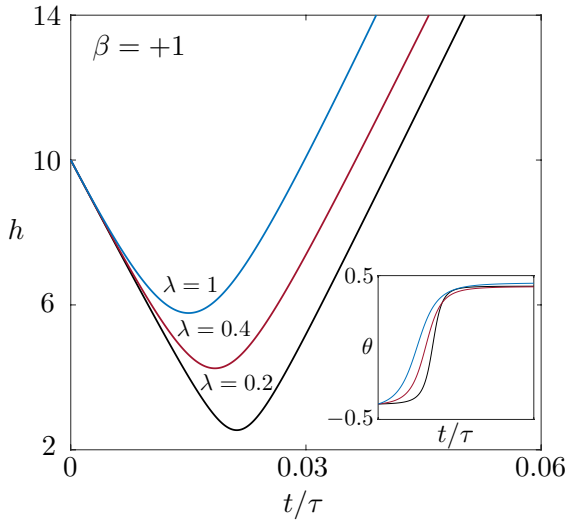

Figure 4.5: The time-evolving behavior of h and θ (inset) for elastic pusher swimmers. Plots are the numerical evaluation of Eqs. (4.10) and (4.11) with $\theta_0 = -\pi/8$, $k = 10^{-4}$, $f = 0.5$ and $\lambda = 0.2, 0.4$ and 1.

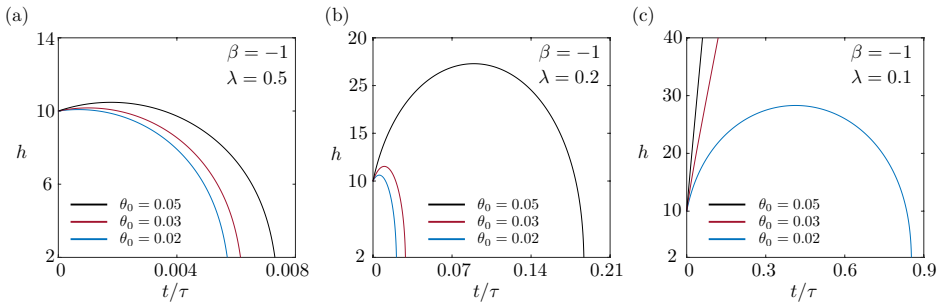

Figure 4.6: The evolution of h for a puller for (a) $\lambda = 0.5$ (b) $\lambda = 0.2$ and (c) $\lambda = 0.1$ with three initial orientations of $\theta_0 = 0.02, 0.03$ and 0.05. For all cases $k = 10^{-4}$ and $f = 0.5$.

4.4 Conclusion

In this chapter, we inquired about the dynamics of an elastic swimmer near a flat wall. Using far-field approximations, we showed that an elastic swimmer bends due to the rotlet dipole generated by the wall. We quantified the effect of bending on the trajectory of the swimmer by considering a two-sphere model. Unlike in pullers wherein the effect of elasticity is not always dominant, repulsion for pushers is found to be unavoidable if we allow the swimmer to bend elastically. Our results highlight the importance of elasticity in understanding the interaction of motile cells with nearby boundaries. Although here we neglect the hydrodynamic interactions in the lubrication regime (i.e., $h < 1$), it has been shown (both computationally [180] and experimentally [13]) that far-field approximations can capture the cell-wall interactions very well. We also note that further insight into effects of elasticity on a swimmer interactions with a surface can be gained by employing more accurate models for the bending mechanism of the hook [94, 139, 173] and also accounting for bending of the flagella [64, 123, 165].

Chapter 5

Elastic two-sphere swimmer in Stokes flow [1]

5.1 Introduction

In the microscale realm of motile cells, inertia is unimportant and the effect of viscous dissipation dominates the fluid forces on swimming bodies [84, 98]. To propel forward in this regime, many microorganisms deform their bodies periodically by converting cells' chemical energy into mechanical work [166]. As a direct consequence of this inertialess environment, to achieve nonzero net locomotion, such body deformations cannot be invariant under time reversal [157]. This constraint, colloquially referred to as the scallop theorem, indicates that due to the kinematic reversibility of the field equations in the low Reynolds number regime, reciprocal body distortions have no net effect.

Theoretically, the scallop theorem can be eluded under two circumstances: non-reciprocal kinematics or a violation of the theorem's assumptions (see [106] and the references therein). The latter exploits the fact that the scallop theorem is solely valid for inertialess single swimmers in quiescent viscous fluid. Therefore, hydrodynamic interactions [190], a non-Newtonian medium [105], or inertia [74] can all lead to propulsion. Non-reciprocal kinematics are employed by many motile

[1] A version of this chapter has been published [138].

cells in nature to facilitate motion [109, 121], and also become a key design principle for model swimmers at small scales. In 1977, Purcell introduced a simple three-link swimmer with two rotational hinges that can change its shape in a non-reciprocal fashion, leading to a locomotion [157]. Subsequently, several analytical model swimmers have been devised wherein non-reciprocal shape change provides the propulsive thrust [44, 70, 92, 135]. Notably, Najafi and Golestanian [134] proposed a simple three-sphere swimmer, in which spheres are identical and connected by two slender rods. The connecting rods change their length in a four-stage cycle that is not invariant under time reversal. After completion of one cycle, the swimmer recovers its original shape but has been translated forward (see also [71] and [115]). Avron et al. [8] suggested a more efficient, yet as simple, swimmer that consists of two linked spherical bladders of different radii. To compensate for the third sphere, they relaxed the rigidity constraint by allowing instantaneous volume exchange between spherical bladders in each stroke. The shape change of the bladders along with the periodic change in their distance, leads to a net displacement of the swimmer. Inspired by these two models, in this chapter we investigate a simple, but less intuitive, two-sphere swimmer where one of the spheres is elastic. We propose that the elastic deformation of the swimmer can be sufficient to escape the scallop theorem, alter hydrodynamic interactions and eventually lead to propulsion.

Elasticity, as an inevitable characteristic of motile cells, can significantly affect the hydrodynamics of a motion. The propulsion of flexible bodies [104, 157, 198], synchronization of flagella [51, 69] and cilia [22, 136, 141] through elastohydrodynamic interactions, and reorientation of uni-flagellated bacteria due to buckling of the flagellum [95, 177] are well-studied examples of such behaviors. For an elastic body in a flow, the balance of viscous forces, external forces and internal elastic forces causes the body to deform and to alter the surrounding flow field, often in a complex fashion [58, 59, 119]. Li et al. [119] reported that for an isolated sedimenting filament, elasticity can destabilize the motion and lead to a substantial buckling. Furthermore, Gao et al. [59] showed that elastic spheres in a shear flow exhibit a 'tank-treading' motion wherein the particle shape is at steady state while the material points on the boundary are undergoing a periodic motion. However, though seemingly simple, sedimentation of spherical elastic particles in a viscous fluid is largely unexplored. The most recent, and to the best of our knowledge the

only, analysis on sedimentation of elastic spheres dates back to more than three decades ago, when Murata [133] investigated the steady state shape deformation of a compressible, Hookean sphere. Using an asymptotic analysis, it was shown that the elastic sphere settles faster and deforms to a prolate spheroid of a smaller volume. In this chpater, to further investigate the deformation of elastic spheres, we revisit this sedimentation problem but this time for an incompressible neo-Hookean sphere under a prescribed body force. We asymptotically describe the steady state effects of non-linear elastic deformations on the swimming behaviors of an isolated elastic sphere.

The chapter is organized as follows. In Section 5.2, we investigate the translation of a single neo-Hookean sphere in Stokes flow. Using an asymptotic approach, we show that for a given body force, due to deformation, the translational velocity of the elastic sphere is smaller compared to a rigid sphere of the same size. Furthermore, we find that the shape deformation is not front-back symmetric and so neither is the flow field generated in the surrounding fluid. In Section 5.3, we show that by exploiting this asymmetry, the proposed two-sphere model can indeed swim in a low Reynolds number regime. Finally, in the case where the distance between the spheres is relatively large, we determine the propulsion velocity.

5.2 Translation of an elastic sphere

We begin our analysis with considering the translation of an incompressible isotropic neo-Hookean sphere in an otherwise quiescent viscous fluid. The sphere has radius R_0 and is driven by body force $\mathbf{f}(t)$. In the fluid domain (Ω_f), the flow field around the sphere is governed by the Stokes equations

$$\operatorname{div} \boldsymbol{\sigma}_\mathrm{f} = \mathbf{0}, \tag{5.1}$$

$$\operatorname{div} \mathbf{v} = 0, \tag{5.2}$$

where $\mathbf{v}$ is the fluid velocity and $\boldsymbol{\sigma}_\mathrm{f}$ is the dynamical stress tensor in the fluid domain defined by the constitutive relation

$$\boldsymbol{\sigma}_\mathrm{f} = -p_\mathrm{f}\mathbf{I} + \eta_\mathrm{f}\Big[\operatorname{grad} \mathbf{v} + (\operatorname{grad} \mathbf{v})^T\Big], \tag{5.3}$$

where p_f is the pressure and η_f is the viscosity of the fluid. We assume the sphere is translating with velocity $\mathbf{U}$ thus the no slip boundary condition dictates $\mathbf{v} = \mathbf{U}$ at the fluid-solid interface. In the solid domain (Ω_s), the governing equations are described in terms of material coordinates. Thus, to avoid any confusion, we write the material gradient, divergence and Laplacian using $\boldsymbol{\nabla}$, $\boldsymbol{\nabla}\cdot$ and ∇^2, respectively. The equilibrium momentum balance in Ω_s then yields

$$\boldsymbol{\nabla}\cdot\boldsymbol{\sigma}_\mathrm{s} + \mathbf{f}(t) = \mathbf{0}, \tag{5.4}$$

where $\boldsymbol{\sigma}_\mathrm{s}$ is the solid elastic stress and $\mathbf{f}$ is a body force density on the sphere. Since the motion is axisymmetric, we assume the elastic sphere reaches a stable equilibrium, wherein the velocity gradient field in the solid domain is zero and the sphere has a rigid motion thereafter [91, 193]. As we will show later, for a weakly-elastic sphere, the leading-order effect of elasticity does not lead to any change in shape. Thus, a higher-order analysis is necessary in order to understand the change in shape of a translating elastic sphere. Extending linear elasticity to higher orders introduces further complexity by involving more material properties [142], instead here we use a phenomenological neo-Hookean model to capture the higher-order effects.The constitutive relation for an isotropic incompressible neo-Hookean solid can be expressed in terms of the displacement vector $\mathbf{u}$ as [81, 142]

$$\boldsymbol{\sigma}_\mathrm{s} = -p_\mathrm{s}\mathbf{I} + \eta_\mathrm{s}\left(\mathsf{F}\cdot\mathsf{F}^T - \mathbf{I}\right), \tag{5.5}$$

where $\mathsf{F} = \mathbf{I} + \boldsymbol{\nabla}\mathbf{u}$ is the deformation gradient tensor and η_s is the shear modulus. For any material point, the displacement vector is defined $\mathbf{u} = \boldsymbol{\chi}(\mathbf{X}, t) - \mathbf{X}$, where $\mathbf{X}$ is the position vector in the reference configuration (in other words material point) and $\boldsymbol{\chi}(\mathbf{X}, t)$ is the deformation vector mapping each material point to its new location [81]. Here, p_s serves only as a Lagrange multiplier to impose the incompressibility of the solid through

$$\det(\mathsf{F}) = 1, \tag{5.6}$$

where $\det(\mathsf{F})$ is the determinant of tensor F. The solid and fluid momentum balances are coupled through the continuity of normal traction at the interface ($\partial\Omega$), which

dictates

$$\boldsymbol{\sigma}_{\mathrm{s}} \cdot \mathbf{n} = \boldsymbol{\sigma}_{\mathrm{f}} \cdot \mathbf{n}, \tag{5.7}$$

where $\mathbf{n}$ is the normal vector to the surface of the deformed sphere.

Without any loss of generality, we will assume that the translational velocity, $\mathbf{U} = U\mathbf{e}_z$, and the body force density, $\mathbf{f} = bf(t)\mathbf{e}_z$, are oriented along $\mathbf{e}_z$. For simplicity we assume a spatially uniform body force where b is a positive constant denoting the magnitude of the forcing while f is a dimensionless $O(1)$ function such that the elastic deformation may be considered quasistatic.

Before going further, we non-dimensionalize all the equations defining dimensionless quantities $\hat{\boldsymbol{\nabla}} = R_0\boldsymbol{\nabla}$, $\hat{\mathbf{u}} = \mathbf{u}/R_0$, $\hat{\mathbf{v}} = \mathbf{v}/U_{\mathrm{ch}}$, $\hat{\mathbf{U}} = \mathbf{U}/U_{\mathrm{ch}}$, $\hat{t} = t/(R_0/U_{\mathrm{ch}})$, $\hat{p}_{\mathrm{f}} = p_{\mathrm{f}}/(\eta_{\mathrm{f}}U_{\mathrm{ch}}/R_0)$, $\hat{\boldsymbol{\sigma}}_{\mathrm{f}} = \boldsymbol{\sigma}_{\mathrm{f}}/(\eta_{\mathrm{f}}U_{\mathrm{ch}}/R_0)$, $\hat{\boldsymbol{\sigma}}_{\mathrm{s}} = \boldsymbol{\sigma}_{\mathrm{s}}/\eta_{\mathrm{s}}$, $\hat{p}_{\mathrm{s}} = p_{\mathrm{s}}/\eta_{\mathrm{s}}$ and $\hat{\mathbf{f}}(t) = \mathbf{f}(t)/(\eta_{\mathrm{s}}/R_0)$, where $U_{\mathrm{ch}} = 2bR_0^2/9\eta_{\mathrm{f}}$. Here U_{ch} simply denotes the translational speed of a rigid sphere under a constant body force of magnitude b. Furthermore, for a forcing profile with frequency ω, we define $\nu = \omega R_0/U_{\mathrm{ch}}$ as a ratio of time scales. Now for convenience, we drop the ($\hat{}$) notation and henceforth refer to dimensionless variables. The dimensionless form of the boundary condition at the fluid-solid interface is then derived

$$\boldsymbol{\sigma}_{\mathrm{s}} \cdot \mathbf{n} = \epsilon\boldsymbol{\sigma}_{\mathrm{f}} \cdot \mathbf{n}, \tag{5.8}$$

where $\boldsymbol{\sigma}_{\mathrm{f}} = -p_{\mathrm{f}}\mathbf{I} + \text{grad } \mathbf{v} + (\text{grad } \mathbf{v})^T$ is the dimensionless stress in the fluid, $\boldsymbol{\sigma}_{\mathrm{s}} = -p_{\mathrm{s}}\mathbf{I} + \boldsymbol{\nabla}\mathbf{u} + \boldsymbol{\nabla}\mathbf{u}^T + \boldsymbol{\nabla}\mathbf{u} \cdot \boldsymbol{\nabla}\mathbf{u}^T$ is the dimensionless stress in the solid phase and $\epsilon = \eta_{\mathrm{f}}U_{\mathrm{ch}}/\eta_{\mathrm{s}}R_0$ represents the ratio of the viscous forces to the elastic forces. The relaxation time scale of the solid $\tau_{\mathrm{relax}} \sim \eta_{\mathrm{f}}/\eta_{\mathrm{s}}$ which when non-dimensionlized scales as $O(\epsilon)$. Thus, for $\epsilon \ll 1$, the time required for relaxation is asymptotically shorter than the imposed time scale of motion, which justifies the quasistatic assumption.

In order to develop a geometric relation between the displacement vector and the surface deformation, we consider spherical coordinate systems (r, θ, ϕ) in the spatial configuration. Since the motion is axisymmetric, we can define the surface

as $r_s(\theta)$ where θ is the polar angle. Thus, at the interface, this definition yields

$$\|\mathbf{X} + \mathbf{u}\| = r_s, \tag{5.9}$$

providing a geometric relation between surface equation and the displacement vector. We should emphasize that the governing equations in Ω_s are expressed in a material description. Thus, to obtain the deformation in the spatial variables, we transform the results of Eq. (5.9), using the mapping $\boldsymbol{\chi}$.

5.2.1 Asymptotic analysis

Here we focus on the case wherein the elastic forces are much larger than the viscous forces, i.e., $\epsilon \ll 1$. We expand all the parameters in terms of ϵ and refer to the i^{th} order of any parameter using superscript (i) (e.g., $p_f = p_f^{(0)} + \epsilon p_f^{(1)} + \epsilon^2 p_f^{(3)} + \cdots$). Due to the linearity of the Stokes equations, at any order the flow field around the sphere is governed by

$$-\text{grad}\, p_f^{(i)} + \text{div}\left(\text{grad}\, \mathbf{v}^{(i)}\right) = \mathbf{0}, \tag{5.10}$$

$$\text{div}\, \mathbf{v}^{(i)} = 0, \tag{5.11}$$

where $\boldsymbol{\sigma}_f^{(i)} = -p_f^{(i)}\mathbf{I} + \text{grad}\, \mathbf{v} + (\text{grad}\, \mathbf{v})^T$ and $i \in \{0, 1, 2, \cdots\}$. We use the general solution given by Sampson for axisymmetric Stokes flow in the spherical coordinate system [84, 170]. The boundary conditions in the fluid domain thereby are $\mathbf{v}^{(i)} = 0$ at $r \to \infty$ and $\mathbf{v} = U\mathbf{e}_z$ at $r = r_s$. In the solid domain, the nonlinear governing equations are linearized perturbatively, thus we treat the problem at each order separately. As one can notice from Eq. (5.8), there is no deformation at the zeroth order thus the leading-order elastic effects are of $O(\epsilon)$. Throughout the following analysis we first solve the solid domain equations using a material description, and then map to the spatial configuration to enforce the interface boundary conditions. All formula given below for $\mathbf{u}$ and p_s are reported in terms of spatial variables.

Zeroth order flow field (first order solid deformations)

At the zeroth order in the fluid domain, the motion is simply the translation of a rigid sphere in Stokes flow. Satisfying $\mathbf{v}^{(0)} = f\,\mathbf{e}_z$ at $r = 1$, we find

$$v_r^{(0)} = \frac{f}{2}\left(\frac{3}{r} - \frac{1}{r^3}\right)\cos\theta, \tag{5.12}$$

$$v_\theta^{(0)} = -\frac{f}{4}\left(\frac{3}{r} + \frac{1}{r^3}\right)\sin\theta, \tag{5.13}$$

$$p_{\mathrm{f}}^{(0)} = \frac{3f}{2r^2}\cos\theta. \tag{5.14}$$

The leading-order deformation equations in the solid domain are in the form of the Stokes equations as

$$-\boldsymbol{\nabla} p_{\mathrm{s}}^{(1)} + \nabla^2 \mathbf{u}^{(1)} + \mathbf{f}(t) = \mathbf{0}, \tag{5.15}$$

$$\boldsymbol{\nabla}\cdot\mathbf{u}^{(1)} = 0, \tag{5.16}$$

$$\boldsymbol{\sigma}_{\mathrm{s}}^{(1)} = -p_{\mathrm{s}}^{(1)}\mathbf{I} + \boldsymbol{\nabla}\mathbf{u}^{(1)} + \boldsymbol{\nabla}\mathbf{u}^{(1)T}. \tag{5.17}$$

Thus, here as well, we can employ Sampson's general solution for an axisymmetric Stokes flow. At this order, the interface boundary condition is $\sigma_{\mathrm{s},rr}^{(1)} = \sigma_{\mathrm{f},rr}^{(0)}$ and $\sigma_{\mathrm{s},r\theta}^{(1)} = \sigma_{\mathrm{f},r\theta}^{(0)}$. Noting that at this order the reference and spatial configurations coincide, we obtain

$$u_r^{(1)} = \frac{f}{2}(1 - r^2)\cos\theta, \tag{5.18}$$

$$u_\theta^{(1)} = \frac{f}{2}(-1 + 2r^2)\sin\theta, \tag{5.19}$$

$$p_{\mathrm{s}}^{(1)} = -\frac{f}{2} r\cos\theta. \tag{5.20}$$

To find the surface deformation, we define surface equation $r_{\mathrm{s}} = 1 + s(\theta)$ and use the geometric relation in (5.9), which at this order leads to $s^{(1)} = u_r^{(1)}$ at $r = 1$. Therefore, we find $s^{(1)} = 0$, indicating that the elastic sphere remains spherical with no surface deformation. We note that this result is similar to the sedimentation of a falling drop in a viscous fluid. Taylor and Acrivos [188] showed that when inertia is neglected and the flow fields both inside and outside the drop are similarly

governed by the Stokes equations, the shape has to remain spherical to satisfy the continuity of the normal tractions at the interface.

First-order flow field (second order solid deformations)

At this order, the flow field at surface of the sphere satisfies $\mathbf{v}^{(1)} = U^{(1)}\mathbf{e}_z$. Recalling that $s^{(1)} = 0$, we find

$$v_r^{(1)} = \frac{U_1 f^2}{2}\left(\frac{3}{r} - \frac{1}{r^3}\right)\cos\theta, \tag{5.21}$$

$$v_\theta^{(1)} = -\frac{U_1 f^2}{4}\left(\frac{3}{r} + \frac{1}{r^3}\right)\sin\theta, \tag{5.22}$$

$$p_{\mathrm{f}}^{(1)} = \frac{3U_1 f^2 \cos\theta}{2r^2}, \tag{5.23}$$

where the first correction for translational velocity U_1 shall be determined by satisfying the interface boundary condition. In the solid domain, the governing equations are

$$-\boldsymbol{\nabla} p_{\mathrm{s}}^{(2)} + \nabla^2 \mathbf{u}^{(2)} + \boldsymbol{\nabla}\left(\boldsymbol{\nabla}\cdot\mathbf{u}^{(2)}\right) + \boldsymbol{\nabla}\cdot\left(\boldsymbol{\nabla}\mathbf{u}^{(1)}\cdot\boldsymbol{\nabla}\mathbf{u}^{(1)T}\right) = \mathbf{0}, \tag{5.24}$$

$$\boldsymbol{\nabla}\cdot\mathbf{u}^{(2)} + \mathrm{tr}(\boldsymbol{\nabla}\mathbf{u}^{(1),\mathrm{c}}) = 0, \tag{5.25}$$

where tr( ) and ( )$^{\mathrm{c}}$ indicate trace and cofactor of the tensor, respectively. Here the stress in the solid phase is defined

$$\boldsymbol{\sigma}_{\mathrm{s}}^{(2)} = -p_{\mathrm{s}}^{(2)}\mathbf{I} + \boldsymbol{\nabla}\mathbf{u}^{(2)} + \boldsymbol{\nabla}\mathbf{u}^{(2)T} + \boldsymbol{\nabla}\mathbf{u}^{(1)}\cdot\boldsymbol{\nabla}\mathbf{u}^{(1)T}. \tag{5.26}$$

Now, by enforcing the interface boundary conditions $\sigma_{\mathrm{s},rr}^{(2)} = \sigma_{\mathrm{f},rr}^{(1)}$ and $\sigma_{\mathrm{s},r\theta}^{(2)} = \sigma_{\mathrm{f},r\theta}^{(1)}$ at $r = 1$, we find $U_1 = 0$ and

$$u_r^{(2)} = -\frac{f^2 r}{304}\left(23 + 27r^2 + (69 + 5r^2)\cos 2\theta\right), \tag{5.27}$$

$$u_\theta^{(2)} = \frac{f^2 r}{304}\left(69 + 97r^2\right)\sin 2\theta, \tag{5.28}$$

$$p_{\mathrm{s}}^{(2)} = \frac{f^2}{152}\left(190 - 199r^2 - 27r^2\cos 2\theta\right), \tag{5.29}$$

leading to $p_{\mathrm{f}}^{(1)} = 0$, $v_r^{(1)} = 0$ and $v_\theta^{(1)} = 0$. It is worthwhile to emphasize that the leading order corrections for the flow field (i.e., $v_r^{(1)}$ and $v_\theta^{(1)}$) are imposed by the leading order deformation in the solid domain. Thus, $s^{(1)} = 0$ indeed causes no disturbance in the flow field at this order. Finally, to find $s^{(2)}$, we use the geometric relation

$$s^{(2)} = u_r^{(2)} + \frac{\left(u_\theta^{(1)}\right)^2}{2}, \quad \text{at } r = 1, \tag{5.30}$$

leading to $s^{(2)} = -\frac{31f^2}{304}(1 + 3\cos 2\theta)$, which indicates a shape deviation from a sphere to an oblate spheroid of aspect ratio $1 - \frac{93}{152}f^2\epsilon^2$.

Second-order flow field (third-order solid deformations)

The no slip boundary condition for the Stokes equations at this order is $\mathbf{v}^{(2)} + s^{(2)}\frac{\partial \mathbf{v}^{(0)}}{\partial r} = U^{(2)}\mathbf{e}_z$. The second order flow field around the sphere is

$$v_r^{(2)} = \frac{U_2 f^3 \cos\theta}{2}\left(\frac{3}{r} - \frac{1}{r^3}\right) + \frac{93f^3\cos\theta}{1520}\left(\frac{2}{r} + \frac{1 - 15\cos 2\theta}{r^3} - \frac{3 - 15\cos 2\theta}{r^5}\right), \tag{5.31}$$

$$v_\theta^{(2)} = -\frac{U_2 f^3 \sin\theta}{4}\left(\frac{3}{r} + \frac{1}{r^3}\right) - \frac{93f^3\sin\theta}{6080}\left(\frac{4}{r} + \frac{13 + 15\cos 2\theta}{r^3} - \frac{27 + 45\cos 2\theta}{r^5}\right), \tag{5.32}$$

$$p_{\mathrm{f}}^{(2)} = \frac{3U_2 f^3\cos\theta}{2r^2} - \frac{93f^3\cos\theta}{3040}\left(\frac{4}{r^2} + \frac{15 - 75\cos 2\theta}{r^4}\right). \tag{5.33}$$

Similar to the previous order, to determine the correction for the translational velocity (i.e., U_2), we need to solve the solid deformation equations at the third order given by

$$-\boldsymbol{\nabla} p_{\mathrm{s}}^{(3)} + \nabla^2 \mathbf{u}^{(3)} + \boldsymbol{\nabla}\left(\boldsymbol{\nabla}\cdot\mathbf{u}^{(3)}\right) + \boldsymbol{\nabla}\cdot\left(\boldsymbol{\nabla}\mathbf{u}^{(1)}\cdot\boldsymbol{\nabla}\mathbf{u}^{(2)T} + \boldsymbol{\nabla}\mathbf{u}^{(2)}\cdot\boldsymbol{\nabla}\mathbf{u}^{(1)T}\right) = \mathbf{0}, \tag{5.34}$$

$$\boldsymbol{\nabla}\cdot\mathbf{u}^{(3)} + \det\left(\boldsymbol{\nabla}\mathbf{u}^{(1)}\right) + T = 0, \tag{5.35}$$

where T is the $O(\epsilon^3)$ contribution of $\mathrm{tr}(\boldsymbol{\nabla}\mathbf{u}^{\mathrm{c}})$. Here, the stress inside the solid is defined

$$\boldsymbol{\sigma}_{\mathrm{s}}^{(3)} = -p_{\mathrm{s}}^{(3)}\mathbf{I} + \boldsymbol{\nabla}\mathbf{u}^{(3)} + \boldsymbol{\nabla}\mathbf{u}^{(3)T} + \boldsymbol{\nabla}\mathbf{u}^{(1)}\cdot\boldsymbol{\nabla}\mathbf{u}^{(2)T} + \boldsymbol{\nabla}\mathbf{u}^{(2)}\cdot\boldsymbol{\nabla}\mathbf{u}^{(1)T}. \tag{5.36}$$

Enforcing the third order interface boundary conditions at $r = 1$ as

$$\sigma_{\mathrm{s},rr}^{(3)} + s^{(2)}\frac{\partial\sigma_{\mathrm{s},rr}^{(1)}}{\partial r} - \frac{\mathrm{d}s^{(2)}}{\mathrm{d}\theta}\sigma_{\mathrm{s},r\theta}^{(1)} = \sigma_{\mathrm{f},rr}^{(2)} + s^{(2)}\frac{\partial\sigma_{\mathrm{f},rr}^{(0)}}{\partial r} - \frac{\mathrm{d}s^{(2)}}{\mathrm{d}\theta}\sigma_{\mathrm{f},r\theta}^{(0)}, \tag{5.37}$$

$$\sigma_{\mathrm{s},r\theta}^{(3)} + s^{(2)}\frac{\partial\sigma_{\mathrm{s},r\theta}^{(1)}}{\partial r} - \frac{\mathrm{d}s^{(2)}}{\mathrm{d}\theta}\sigma_{\mathrm{s},\theta\theta}^{(1)} = \sigma_{\mathrm{f},r\theta}^{(2)} + s^{(2)}\frac{\partial\sigma_{\mathrm{f},r\theta}^{(0)}}{\partial r} - \frac{\mathrm{d}s^{(2)}}{\mathrm{d}\theta}\sigma_{\mathrm{f},\theta\theta}^{(0)}, \tag{5.38}$$

we finally find $U_2 = -\frac{31f^3}{380}$, and

$$u_r^{(3)} = \left(7r^2\left(310r^2 - 2091\right)\cos 2\theta - 5816r^4 + 9645r^2 - 30240\right)\frac{f^3\cos\theta}{25536}, \tag{5.39}$$

$$u_\theta^{(3)} = \left(7r^2\left(434r^2 + 697\right)\cos 2\theta + 5284r^4 + 381r^2 + 10080\right)\frac{f^3\sin\theta}{8512}, \tag{5.40}$$

$$p_{\mathrm{s}}^{(3)} = -r\left(322r^2\cos 2\theta + 3766r^2 - 2991\right)\frac{f^3\cos\theta}{1596}. \tag{5.41}$$

Thence, we can determine the third order shape deformation using the geometric relation (5.9), which reads $s^{(3)} = u_r^{(3)} + u_\theta^{(1)}u_\theta^{(2)}$ at $r = 1$. Notably, we find $s^{(3)} = -\frac{2777f^3}{1824}\cos^3\theta$ indicating a 'egg-like' deformation which exhibits a front-back asymmetry in the surface of the elastic sphere as shown in Fig. 5.1.

It is also worthwhile to note that elastic capsules containing viscous fluids exhibit a similar asymmetry in their deformation under pure translation. In a numerical study, Ishikawa et al. [93] showed that at steady state, a weakly-elastic spherical micro-torque swimmer deforms to an egg-like shape. A similar deformation was observed experimentally for sedimenting vesicles as well [91].

Third-order flow field

To quantify the effect of the shape asymmetry on the motion of the particle, we shall determine the third order correction for the flow field. Once again, we solve

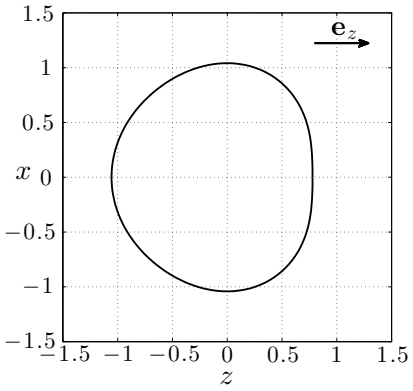

Figure 5.1: Deformed shape of the translating elastic sphere when $f = 1$ and $\epsilon = 0.45$.

the Stokes equations, but this time with $\mathbf{v}^{(3)} + s^{(3)} \frac{\partial \mathbf{v}^{(0)}}{\partial r} = U^{(3)} \mathbf{e}_z$ at $r = 1$. Thus, we can find the third order correction for the fluid field and stress field in terms of the translational velocity $U^{(3)}$. Now to find $U^{(3)}$, instead of solving for the next order solid deformation (as we did in the previous orders), we employ an auxiliary case wherein a rigid sphere of the same radius is translating with the same driving force [149]. Since the motion is over-damped, regardless of the shape, the driving force is always entirely balanced by the viscous surface forces. Thus, for a given driving force, the net drag force on both elastic and rigid spheres are the same. For the elastic sphere we have

$$\mathbf{F}^{\mathrm{dr}} + 3\epsilon \int_{\partial\Omega} \boldsymbol{\sigma}_{\mathrm{f}} \cdot \mathbf{n} \mathrm{d}S = \mathbf{0}, \tag{5.42}$$

where $\mathbf{F}^{\mathrm{dr}} = \mathbf{f}V$ is the total driving force on the sphere, V is the volume and S represent dimensionless area element of the sphere. On the other hand, for the rigid sphere case, the drag law dictates $\mathbf{F}^{\mathrm{dr}}/V = \frac{9f}{2}\epsilon\, \mathbf{e}_z$, thus

$$\frac{1}{V} \int_{\partial\Omega} \boldsymbol{\sigma}_{\mathrm{f}} \cdot \mathbf{n} \mathrm{d}S = -\frac{3f}{2} \mathbf{e}_z. \tag{5.43}$$

Since div $\boldsymbol{\sigma}_{\mathrm{f}} = \mathbf{0}$, by the divergence theorem, one may alternatively integrate the traction over an undeformed sphere of radius larger than the mean radius of

the deformed sphere. Then by substituting $\boldsymbol{\sigma}_{\mathrm{f}} = \boldsymbol{\sigma}_{\mathrm{f}}^{(0)} + \epsilon\boldsymbol{\sigma}_{\mathrm{f}}^{(1)} + \epsilon^2\boldsymbol{\sigma}_{\mathrm{f}}^{(2)} + \epsilon^3\boldsymbol{\sigma}_{\mathrm{f}}^{(3)}$, we determine the left-side of Eq. (5.43) as $\frac{1}{V}\int_{\partial\Omega}\boldsymbol{\sigma}_{\mathrm{f}}\cdot\mathbf{n}\mathrm{d}S = -\frac{3}{2}\left(f + U^{(3)}\epsilon^3\right)\mathbf{e}_z$, indicating that $U^{(3)} = 0$. Thus, the final expression for the translational velocity

$$U = \left[1 - \frac{31}{380}f^2\epsilon^2 + O(\epsilon^4)\right]f, \tag{5.44}$$

and the third order corrections in the flow field are

$$v_r^{(3)} = \frac{2777f^4}{17024}\left(\frac{1}{r^2} - \frac{1}{r^4}\right)\left(3 - 9\cos^2\theta - \frac{3 - 30\cos^2\theta + 35\cos^4\theta}{r^2}\right), \tag{5.45}$$

$$v_\theta^{(3)} = \frac{2777f^4}{34048}\left(\frac{\sin 2\theta}{r^4}\right)\left(12 - 14\cos^2\theta - \frac{12 - 28\cos^2\theta}{r^2}\right), \tag{5.46}$$

$$p_{\mathrm{f}}^{(3)} = \frac{2777f^4}{42560}\left(\frac{1}{r^4}\right)\left(15 - 45\cos^2\theta - \frac{21 - 210\cos^2\theta + 245\cos^4\theta}{r^2}\right). \tag{5.47}$$

To recover the solution for the case of translation under a constant body force (i.e. sedimentation), one can set $f = 1$ finding $U = 1 - \frac{31}{380}\epsilon^2 + O(\epsilon^4)$. We see that the deformation of the incompressible neo-Hookean sphere causes a reduction in the settling speed compared to a rigid sphere. Our results are notably different when compared with the sedimentation of a compressible Hookean solid for which a faster-than-rigid settling speed and a reduction in volume are reported [133].

5.3 Two-sphere swimmer

We consider a model swimmer which consists of two spheres: a rigid sphere A and a neo-Hookean isotropic incompressible elastic sphere B (identical to the elastic sphere defined in Section 5.2). The spheres are of equal radii and linked by a rod of length L. To propel itself forward, the swimmer repeats a two-step, one-dimensional motion in which the connecting rod shortens its length in step (I), and then returns back to its original length in step (II) in a harmonic fashion (see Fig. 5.2). While advancing from one step to another, sphere B changes its shape continuously and instantaneously, until it reaches its spherical shape again at the end point of each step. We note that despite the reversible actuation, the flow field induced by sphere B is not front-back symmetric. Thus, for sphere A, the contribution of the background flow (induced by sphere B) is different between step

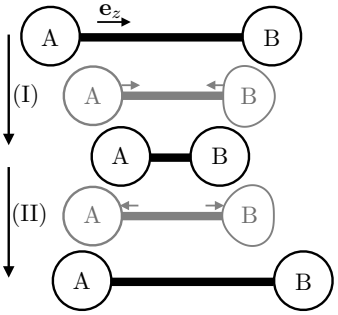

Figure 5.2: One cycle of the two-step motion of the swimmer. Step (I): The rod shortens its length. Step (II): Spheres move away from one another until they reach the initial distance. The steps in grey color demonstrate the swimmer while it proceeds to the next step and sphere B is deformed.

(I) and (II). The net motion in each cycle thereby is not kinematically reversible and indeed the swimmer can propel with a velocity that we determine below.

The connecting rod exerts driving forces $\mathbf{F}_\mathrm{A}$ and $\mathbf{F}_\mathrm{B}$ on spheres A and B, respectively. The force-free motion of the swimmer necessitates $\mathbf{F}_\mathrm{A} + \mathbf{F}_\mathrm{B} = \mathbf{0}$. Although, in practice, the driving forces are applied locally at the sphere-rod junctions, here we neglect the effect of the rod and assume a spatially uniform force density for both spheres, noting that such actuation forces can be imposed by magnetic fields or optical tweezers. Thus, we prescribe the periodic motions by defining $\mathbf{F}_\mathrm{A}/V = -\mathbf{F}_\mathrm{B}/V = \frac{9}{2}\epsilon \sin(\nu t)\mathbf{e}_z$. Assuming that spheres are well separated at all times, we employ a far-field approximation to determine the flow field around the swimmer. The velocity of each sphere, i.e. $\mathbf{U}_\mathrm{A}$ and $\mathbf{U}_\mathrm{B}$, then follows the drag law

$$\mathbf{U}_\mathrm{A} = \mathbf{R}_\mathrm{A}^{-1} \cdot \mathbf{F}_\mathrm{A} + \mathcal{F}_\mathrm{A}\left[\mathbf{v}_{\mathrm{B}\to\mathrm{A}}\right], \tag{5.48}$$

$$\mathbf{U}_\mathrm{B} = \mathbf{R}_\mathrm{B}^{-1} \cdot \mathbf{F}_\mathrm{B} + \mathcal{F}_\mathrm{B}\left[\mathbf{v}_{\mathrm{A}\to\mathrm{B}}\right], \tag{5.49}$$

where $\mathbf{R}_\mathrm{A}$ and $\mathbf{R}_\mathrm{B}$ are hydrodynamic resistance tensors for spheres A and B, $\mathcal{F}_\mathrm{A}$ and $\mathcal{F}_\mathrm{B}$ are the Faxèn operators, and $\mathbf{v}_{\mathrm{B}\to\mathrm{A}}$ ($\mathbf{v}_{\mathrm{A}\to\mathrm{B}}$) is the background flow field on sphere A (B), induced by sphere B (A). Here, to focus only on the leading order propulsion velocity, we limit our calculations to the first reflection of the

flow fields. Therefore, we neglect the contribution of the background flow on the deformation of sphere B. At each step, we take the average velocity of the two spheres as the instantaneous velocity of the swimmer, defining $\mathbf{U}^{(\mathrm{I})} = \frac{\mathbf{U}_{\mathrm{A}}^{(\mathrm{I})}+\mathbf{U}_{\mathrm{B}}^{(\mathrm{I})}}{2}$ and $\mathbf{U}^{(\mathrm{II})} = \frac{\mathbf{U}_{\mathrm{A}}^{(\mathrm{II})}+\mathbf{U}_{\mathrm{B}}^{(\mathrm{II})}}{2}$, where superscripts (I) and (II) refer to the quantities at the corresponding steps. Thence, to find the net propulsion velocity we average the swimming velocities over one complete cycle

$$\bar{\mathbf{U}} = \frac{1}{\tau}\left(\int_0^{\tau/2} \mathbf{U}^{(\mathrm{I})}\mathrm{d}t + \int_{\tau/2}^{\tau} \mathbf{U}^{(\mathrm{II})}\mathrm{d}t\right), \tag{5.50}$$

where $\tau = 2\pi/\nu$ is the period of the cycle. By making use of Eqs. (5.48) and (5.49) and noting that $\mathbf{F}_{\mathrm{A}}(t+\frac{\tau}{2}) = -\mathbf{F}_{\mathrm{A}}(t)$ and $\mathbf{F}_{\mathrm{B}}(t+\frac{\tau}{2}) = -\mathbf{F}_{\mathrm{B}}(t)$, Eq. (5.50) can be reduced to

$$\bar{\mathbf{U}} = \frac{1}{2\tau}\left\{\int_0^{\tau/2}\left(\mathcal{F}_{\mathrm{A}}\left[\mathbf{v}_{\mathrm{B}\to\mathrm{A}}^{(\mathrm{I})}\right] + \mathcal{F}_{\mathrm{B}}\left[\mathbf{v}_{\mathrm{A}\to\mathrm{B}}^{(\mathrm{I})}\right]\right)\mathrm{d}t + \int_{\tau/2}^{\tau}\left(\mathcal{F}_{\mathrm{A}}\left[\mathbf{v}_{\mathrm{B}\to\mathrm{A}}^{(\mathrm{II})}\right] + \mathcal{F}_{\mathrm{B}}\left[\mathbf{v}_{\mathrm{A}\to\mathrm{B}}^{(\mathrm{II})}\right]\right)\mathrm{d}t\right\}. \tag{5.51}$$

From the general description of Faxèn operator [20, 97], we find $\mathcal{F}_{\mathrm{A}} = 1 + \frac{1}{6}\nabla^2$ and $\mathcal{F}_{\mathrm{B}} = 1 + \left(\frac{1}{6} + \frac{31}{228}\epsilon^2\right)\nabla^2 + O(\epsilon^3/l^2)$. Now using the asymptotic descriptions of the flow fields reported in Section 5.2, we arrive at the leading order propulsion velocity

$$\bar{\mathbf{U}} = \frac{24993}{136192}\frac{\epsilon^3}{L^2}\mathbf{e}_z. \tag{5.52}$$

We note that the deformation of the sphere governs the propulsive thrust and that the magnitude of the change in distance between the spheres does not contribute to the leading order motion, unlike the three sphere swimmer where the difference in arm lengths quantifies the asymmetry [134].

5.4 Conclusion

In this chapter, we inquired about the effects of elasticity on swimming in Stokes flow. We started by addressing the pure translation of an elastic particle in viscous fluid. We asymptotically showed that under a body force the translational velocity

of an elastic sphere is slower, and also the shape deformation is not front-back symmetric. The latter indicates an asymmetry in the surrounding flow field which can be exploited to evade the scallop theorem. To highlight the effect of this deformation on swimming, we proposed a very simple swimmer of two spheres that can swim with a reversible actuation, solely due to elasticity of one of the spheres. Our results show that accounting for elasticity of bodies may be crucial to fully understand the dynamics of swimming cells and specifically can be useful in designing microswimmers. Finally we note that while conceptually simple, our elastic two-sphere swimmer is not very effective for small deformations, but in practice one might use an elastic body which is already asymmetric to exacerbate this effect.

Chapter 6

Hydrodynamic interactions of cilia on a spherical body [1]

6.1 Introduction

To propel themselves in a low-Reynolds-number regime [157], many microorganisms use small whip-like extensions, called flagella (when they possess one or two) or cilia (when they possess many) [19, 124]. The motion of cilia is controlled by ATP-fuelled motor proteins which exert a driving force on the cilia by converting chemical energy in the cell [166]. The cyclic motion of each cilium in a chain can form a coordinated pattern of beating, wherein each pair of neighboring cilia are orbiting with a constant, non-zero, phase difference [101]. As a result of this synchrony, the tips of cilia form a moving wave, known as a metachronal wave [78]. By forming metachronal waves, the microorganism minimizes the required energy for beating [77], which enhances the efficiency of the motion [99]. In addition to providing a means of locomotion, cilia in the human body filter air flow channels in the lung from the harmful inhaled material [171], and also play a crucial role in breaking the left-right symmetry in human embryonic development [87].

Several analytical studies have shown that hydrodynamic interactions alone can lead to synchronization (zero phase difference) or phase-locking (constant non-zero

[1] A version of this chapter has been published [136]

phase difference) for model systems of two flagella [51, 191, 192] or many cilia [31, 141]. Using minimal models, it was observed that certain conditions, be they elastic deformations of trajectory [141], or shape [53], or a certain forcing profile [191], may be required to reach such phase-locking or synchronization. Recent experimental studies have also confirmed the hydrodynamic synchronization of micro-scale oscillators in natural systems. Using high-speed video microscopy, it was shown that beating flagella on *Chlamydomonas reinhardtii* [67, 152] and *Volvox carteri* [22, 24], exhibit a synchronization due to hydrodynamic interactions. Similar synchrony was observed in model colloidal systems where two spheres were oscillating on linear [26, 102] or circular [18] trajectories and each sphere was driven by optical tweezers.

In a ciliary array, the distribution of cilia as well as the details of the ciliate body affect the behavior of the dynamical system [25, 54, 73]. Niedermayer *et al.* reported that introducing radial flexibility to the circular trajectory of two orbiting beads leads to synchronization, but that a non-periodic array of such beads cannot reach stable collective phase-locking [141]. They also showed that marginally-stable metachronal waves are formed only when the cilia are distributed in a periodic fashion. More recently it was observed that an open-ended array of cilia can indeed form robust metachronal waves if the cilia beat perpendicular to the ciliate boundary [22]. It has also been shown that the presence of a large body near an array of linearly oscillating beads is necessary for emergence of metachronal waves [203]. The bounding surface restricts the range of hydrodynamic interactions of the beads and leads the system to a collectively phase-locked state. The emerging picture from the literature is that the stability and existence of metachronal waves depends on the geometry of the cilia and ciliate body. Notably however, in many ciliates in nature the cilia are continuously distributed about a closed curved body such as on *paramecia* or *volvox*, and this imposes a natural periodicity to the dynamical system and mediates the hydrodynamic interactions of the ciliary chains in a way that is yet to be understood.

In this chapter we investigate the effects of a large curved ciliate body on the hydrodynamic interactions of cilia in a viscous fluid. Following the work of Niedermayer *et al.* who studied interactions of cilia above a flat wall [141], we use the discrete-cilia model [16, 122] where each cilium is replaced by a single sphere

and assume that a constant tangential forcing is applied by the dynein motors. We first present an analysis of the interactions of two cilia and then build up our model of a chain of cilia around a large spherical body. We show that the radial flexibility in the trajectories can lead the system to synchronize similar to the case of cilia near a flat boundary [141]. Furthermore, we show that with this model, the only stable fixed point for a chain of identical cilia is when all cilia are in phase (synchronized). Finally, we demonstrate an emergent wave-like behavior of the cilia in response to an imposed asymmetry in the beating rate of one cilium.

6.2 Motion of a single cilium

We model the cilium as a single sphere of radius $\hat{a}$ undergoing a circular orbit, of radius $\hat{R}$, whose center is at distance $\hat{h}$ from the ciliate body as shown in Fig. 6.1. Dynein motors drive the motion of the cilium and, in a viscous fluid at small scales, this forcing is balanced entirely by the hydrodynamic drag,

$$\hat{\mathbf{F}}^m + \hat{\mathbf{F}}^D = \mathbf{0}. \tag{6.1}$$

A simple model of the forcing stipulates a constant tangential driving force [113], $\hat{F}^{\mathrm{dr}}$, and an elastic restoring force that keeps the cilia moving along a preferred path (of radius $\hat{R}_0$) [141], such that

$$\hat{\mathbf{F}}^m = \hat{F}^{\mathrm{dr}}\mathbf{e}_\phi - \hat{k}\left(\hat{R} - \hat{R}_0\right)\mathbf{e}_R, \tag{6.2}$$

where $\hat{k}$ is the stiffness of the cilia. The drag force, $\hat{\mathbf{F}}^D$, for the rigid body translation of a sphere at velocity $\hat{\mathbf{U}}$ is given by the drag law

$$\hat{\mathbf{F}}^D = -\hat{\mathbf{R}}_{FU} \cdot \left(\hat{\mathbf{U}} - \mathcal{F}\left[\hat{\mathbf{u}}^\infty\right]\right), \tag{6.3}$$

where $\mathbf{u}^\infty$ is the background flow and the Faxén operator is $\mathcal{F} = 1 + \frac{\hat{a}^2}{6}\nabla^2$ [11]. The resistance tensor for a sphere moving parallel to a wall is $\hat{\mathbf{R}}_{FU} = 6\pi\hat{\mu}\hat{a}\left(\mathbf{I} + O(\hat{a}^3/\hat{h}^3)\right)$ [84]. In our analysis, we assume the thickness of a cilium is much smaller than its length so that in our minimal model $\hat{a} \ll \hat{h}$, therefore the effect of wall on the hydrodynamic resistance shall be neglected.

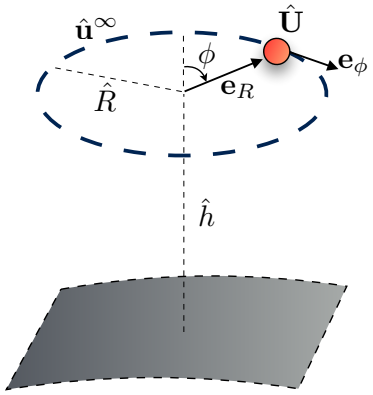

Figure 6.1: A schematic of the motion of a model cilium near a spherical body. The circular trajectory has a radius of $\hat{R}$ and its center is at distance $\hat{h}$ from the boundary. The cilium moves with velocity $\hat{\mathbf{U}}$ through a fluid with velocity $\hat{\mathbf{u}}^{\infty}$. In this study, ϕ indicate the instantaneous phase of the cilium and the vectors $\mathbf{e}_{\phi}$ and $\mathbf{e}_R$ show the tangential and radial directions of the motion, respectively.

As a starting point, we examine the motion of a single cilium in the absence of other cilia. The background flow field is then zero and the cilium orbits strictly on its preferred circular path. In this case, Eq. (6.2) leads to a steady state solution

$$\dot{\hat{\phi}}_{ss} = \frac{\hat{F}^{\mathrm{dr}}}{6\pi\hat{\mu}\hat{a}\hat{R}_0} \equiv \hat{\omega}, \tag{6.4}$$

$$\dot{\hat{R}}_{ss} = 0, \quad \hat{R}_{ss} = \hat{R}_0, \tag{6.5}$$

where the over-dot indicates differentiation with respect to time and $\hat{\omega}$ defined as the intrinsic angular velocity of the cilium. Using the reported values for the bending rigidity of a cilium [27, 143], Niedermayer *et al.* [141] noted that radial relaxation is much faster than a period of rotation, namely $\hat{F}^{dr}/\hat{k}\hat{R}_0 \ll 1$, and so a quasi-static assumption may be employed for the radial dynamics of the system.

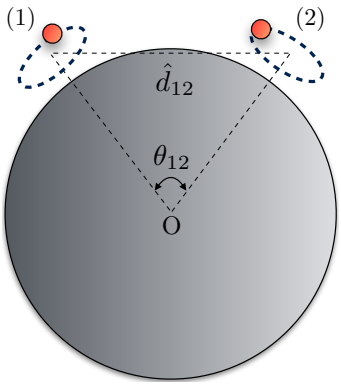

Figure 6.2: A system of two cilia around a spherical body of radius $\hat{A}$. In this figure, $\hat{d}_{12}$ is the distance and θ_{12} is the angle between center of the trajectories.

6.3 Interactions of two cilia

We now consider a system of two cilia around a spherical body, with trajectories centered at a distance $\hat{d}_{12}$ as shown in Fig. 6.2. The velocity of each cilium can be written as $\hat{\mathbf{U}}_i = \hat{R}_i\dot{\hat{\phi}}_i\mathbf{e}_{\phi_i} + \dot{\hat{R}}_i\mathbf{e}_{R_i}$, where $i \in \{1,2\}$. The motion of each cilium in this case is affected by the background flow field induced by the other cilium. The ciliate body is considerably larger than the thickness of a cilium, $\hat{a} \ll \hat{A}$, where $\hat{A}$ is the radius of the spherical body. We also assume the cilia are far apart from one another ($\hat{d}_{12} \gg \hat{h}, \hat{R}_0$) [143], so that far-field approximations for the induced flow fields may be employed. Under these assumptions one can model the flow field due to the motion of a sphere by a point force (or Stokeslet) to leading order while the no-slip boundary condition on the surface of the spherical body is satisfied by an image Stokeslet set in the body. The background flow field on cilium (1), induced by cilium (2) is

$$\hat{\mathbf{u}}^{\infty}(\hat{\mathbf{x}}_1) = \frac{1}{8\pi\hat{\mu}}\left(\hat{\mathbf{J}}(\hat{\mathbf{x}}_1,\hat{\mathbf{x}}_2) + \hat{\mathbf{J}}^*(\hat{\mathbf{x}}_1,\hat{\mathbf{x}}_2^*)\right)\cdot\hat{\mathbf{F}}_2^m, \tag{6.6}$$

where $\hat{\mathbf{F}}_2^m$ refers to the driving force of the cilium (2), $\hat{\mathbf{x}}_1$ and $\hat{\mathbf{x}}_2$ indicate the location of each cilium, $\hat{\mathbf{J}}$ is the Oseen tensor and $\hat{\mathbf{J}}^*$ is the Blake's solution for the image Stokeslet [17, 84], at a point $\hat{\mathbf{x}}_2^* = (\hat{A}^2/|\hat{\mathbf{x}}_2|^2)\hat{\mathbf{x}}_2$ located to satisfy the no-slip

condition at the spherical boundary [181].

Before going further, we non-dimensionalize all equations by scaling lengths by the radius of the spherical body, $\hat{A}$, and rates by the average angular velocity of the two cilia, $\bar{\hat{\omega}}$. We drop the notation ($\hat{}$) for the dimensionless quantities defined by $\hat{a} = \hat{A}a$, $\hat{R}_j = \hat{A}R_j$, $\hat{h} = \hat{A}h$, $\hat{d}_{12} = \hat{A}d_{12}$, $\hat{\omega}_j = \bar{\hat{\omega}}\omega_j$ and $\dot{\hat{\phi}}_j = \bar{\hat{\omega}}\dot{\phi}_j$, $\hat{\mathbf{U}}_j = (\hat{A}\bar{\hat{\omega}})\mathbf{U}_j$, $\dot{\hat{R}}_j = (\hat{A}\bar{\hat{\omega}})\dot{R}_j$, $\hat{t} = (1/\bar{\hat{\omega}})t$ and $\hat{\mathbf{R}}_{FU} = (\hat{k}/\bar{\hat{\omega}})\mathbf{R}_{FU}$. A dimensionless parameter $\kappa = \hat{k}/6\pi\hat{\mu}\hat{a}\bar{\hat{\omega}} \gg 1$ which indicates the ratio of the elastic restoring force to the hydrodynamic drag force then naturally arises. We assume the dimensionless length scales are ordered as follows, $a \ll \{h, R_0\} \ll 1$ and take $R_0 = O(h)$ [143]. Since the radius of the trajectory is small compared to the scale of the body, we may write $d_{12} = 2\sin(|\theta_{12}|/2) + O(h)$.

In these limits, by using the description for background flow field in Eq. (6.6), the motion Eq. (6.2) can be solved for case of two neighboring cilia, asymptotically. The evolution equations are then to leading order

$$\dot{\phi}_1 = \omega_1 + \rho\omega_2 S_{12} - \frac{\rho\omega_1\omega_2}{\kappa} L_{12}, \tag{6.7}$$

$$\dot{\phi}_2 = \omega_2 + \rho\omega_1 S_{21} - \frac{\rho\omega_1\omega_2}{\kappa} L_{21}, \tag{6.8}$$

$$R_1 = R_0 + \frac{\rho R_0\omega_2}{\kappa} L_{12}, \tag{6.9}$$

$$R_2 = R_0 + \frac{\rho R_0\omega_1}{\kappa} L_{21}, \tag{6.10}$$

where $\rho = 9ah^2/8$ is the strength of the hydrodynamic interactions dictated by the functions

$$S_{ij} = \frac{4}{d_{ij}^3}\Big[\Theta_{ij}\cos\Delta_{ij} + \Phi_{ij}\cos\varphi_{ij}\Big], \tag{6.11}$$

$$L_{ij} = \frac{4}{d_{ij}^3}\Big[\Theta_{ij}\sin\Delta_{ij} + \Phi_{ij}\sin\varphi_{ij}\Big]. \tag{6.12}$$

Here we've defined phase difference $\Delta_{ij} = \phi_i - \phi_j$ and sum $\varphi_{ij} = \phi_i + \phi_j$ while the distance between cilium is given by $d_{ij} = 2\sin(|\theta_{ij}|/2)$ where θ_{ij} is the angle

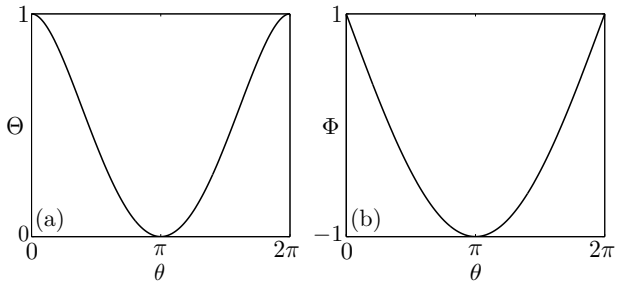

Figure 6.3: Geometric terms (a) Θ and (b) Φ as functions of the angle between cilia.

between the cilia i and j. Finally the functions

$$\Theta_{ij} = \frac{\cos|\theta_{ij}| + \sin(|\theta_{ij}|/2)}{1 + \sin(|\theta_{ij}|/2)}, \tag{6.13}$$

$$\Phi_{ij} = \frac{\cos|\theta_{ij}| - \sin(|\theta_{ij}|/2)}{1 + \sin(|\theta_{ij}|/2)}, \tag{6.14}$$

capture the effect of the geometry of the spherical body on the hydrodynamic interactions, as shown in Fig. 6.3.

We observe that as expected hydrodynamic interactions above a wall scale as $O(d_{ij}^{-3})$ [113, 192], but now, due to the spherical shape of the ciliate body, both the relative position, Δ and average position φ, of the two cilia around the ciliate body affect the hydrodynamic interactions as well by way of the geometric functions Θ and Φ respectively. The background flow velocity on each cilium (induced by the other) directly impacts both the angular velocity of each cilium, through the function S_{ij}, as well as its radial position via the function L_{ij}, which in turn affects the phase-speed as well.

Taking the difference of (6.7) and (6.8) we obtain an evolution equation for the phase difference

$$\dot{\Delta}_{12} = \Delta\omega(1 - \rho S_{12}) - 2(\rho/\kappa)\omega_1\omega_2 L_{12}, \tag{6.15}$$

where $\Delta\omega = \omega_1 - \omega_2$. We see the phase difference evolves due to a difference in the

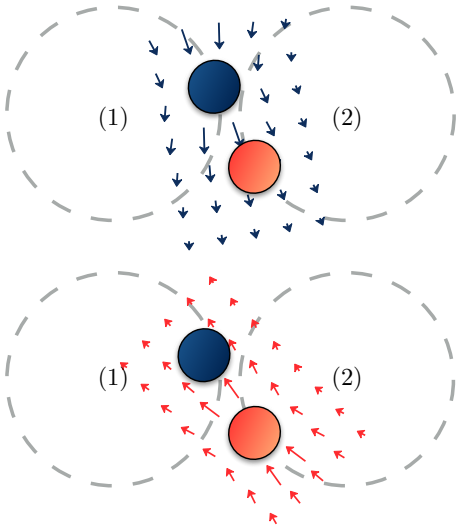

Figure 6.4: The effect of the background flow field on the motion of each cilia. The two cilia are orbiting clockwise, cilium (2) is ahead, thus its induced flow field pulls cilium (1) to a smaller radius of trajectory which increases the instantaneous velocity of cilium (1). On the other hand, the velocity of cilium (2) decreases as the flow field of cilium (1) pushes cilium (2) to a larger trajectory. In this figure arrows show the flow field induced by each cilium.

intrinsic phase-speed, due to hydrodynamic interactions directly but also indirectly because of elastic radial displacements. To illustrate the latter point, let us assume cilium (2) is ahead by a positive phase difference of Δ_{12}, as shown in Fig. 6.4. In this case, the background flow drives a contraction of the orbit for cilium (1) ($R_1 < R_0$) and expansion of the orbit for cilium (2) ($R_2 > R_0$). Since the internal driving forces of the cilia are constant, the changes in trajectories speed up cilium (1) and slow down cilium (2).

If intrinsic velocities are different, $\Delta\omega \neq 0$, for an equilibrium phase difference to arise, this difference must not overwhelm the elasto-hydrodynamic interactions, in other words $\Delta\omega = O(\rho)$ for fixed points in phase-difference. The second term on the right-hand side of Eq. (6.15) is then $O(\rho^2)$ and shall be neglected.

To provide further clarity we note that the individual phases evolve on a much

shorter time scale than the phase-differences, $\dot{\phi}_i = O(1)$ while $\dot{\Delta}_{12} = O(\rho)$; hence, we use a multiple scale analysis and average over a period of the short-time scale, $\tau_{\phi} = 2\pi/\omega_1 + O(\rho)$ to focus on the long-time behavior of the phase difference (indicated with an overbar). The cycle-averaged evolution equation for the phase-difference is then an Adler equation

$$\dot{\bar{\Delta}}_{12} = \Delta\omega - \gamma\Theta_{12}\sin\bar{\Delta}_{12}, \tag{6.16}$$

where the synchronization strength in the case of a flat wall $\gamma = 8(\rho/d^3\kappa)\omega_1\omega_2$ [141], is augmented by the geometric term Θ_{12}. If the frequency mismatch is small enough to be balanced by the elasto-hydrodynamic coupling, $|\Delta\omega| < \gamma\Theta_{12}$, a steady-state phase difference emerges given by $\bar{\Delta}_{12}^{\text{eq}} = \sin^{-1}(\Delta\omega/\gamma\Theta_{12})$. In the limiting case of a rigid cilium ($\kappa \to \infty$) hydrodynamic interactions do not lead to an evolution of phase, and no phase-locking can occur where $\Delta\omega \neq 0$. When the cilia are identical (i.e., $\omega_1 = \omega_2 = 1$) the phase-locking of the system is guaranteed (if $\theta_{12} \neq \pi$) as Equation (6.16) reduces to

$$\dot{\bar{\Delta}}_{12} = -\gamma\Theta_{12}\sin\bar{\Delta}_{12}, \tag{6.17}$$

indicating that the equilibrium phase difference is zero.

Unsurprisingly, the evolution equations for phase difference on a spherical body are largely similar to above a flat wall under the assumption that the cilia are much smaller than the ciliate. The difference is that the hydrodynamic interactions are mediated by the geometry of the body through Θ_{12}. We see that when the two cilia are located at the opposite sides of the spherical body ($\theta_{12} = \pi$), radial interactions are completely screened by the ciliate as $\Theta_{12} = 0$. We also note that for the angles near zero (and 2π), special care must be used as these limits force $d_{12} \to 0$. To evaluate the system at these angles we can rescale the evolution Eqs. (6.7) and (6.8) with distance $\hat{d}_{12}$, thereby recovering the flat body solution reported in Ref. [141] in the limiting case where $\theta_{12} \to 0$ (or 2π) and $\hat{A} \to \infty$.

6.4 Interactions of chain of cilia

Now we proceed to the system of N identical cilia around a spherical body where $N \geq 3$. Relying on the linearity of the Stokes equation, the flow field induced by a chain of cilia can be determined by summing the contributions of all the cilia as well as their image points. Following the procedure outlined in the case of two cilia, the evolution equation for cilium (i) in a chain of N cilia, to the leading order, is

$$\dot{\phi}_i = \omega_i + \rho \sum_{j \neq i}^{N} \omega_j S_{ij} - \frac{\rho \omega_i}{\kappa} \sum_{j \neq i}^{N} \omega_j L_{ij}, \tag{6.18}$$

where $\{i, j\} \in \{1, 2, \ldots, N\}$. For simplicity, we shall assume first that all cilia in the chain have the same intrinsic angular velocity, $\omega_i = \omega_j = 1$. The evolution of the phase difference on the long time scale is then

$$\begin{aligned} \dot{\bar{\Delta}}_{1i} = 4\rho \sum_{m \neq 1}^{N} \sum_{j \neq i}^{N} \left(d_{1m}^{-3} \Theta_{1m} \cos \bar{\Delta}_{1m} - d_{ij}^{-3} \Theta_{ij} \cos \bar{\Delta}_{ij} \right) \\ - \frac{4\rho}{\kappa} \sum_{m \neq 1}^{N} \sum_{j \neq i}^{N} \left(d_{1m}^{-3} \Theta_{1m} \sin \bar{\Delta}_{1m} - d_{ij}^{-3} \Theta_{ij} \sin \bar{\Delta}_{ij} \right), \end{aligned} \tag{6.19}$$

where we have set cilium (1) as the reference phase, defining $\Delta_{1i} = \phi_1 - \phi_i$. We note that unlike the case of two identical cilia where the average tangential terms do not contribute to synchronization (because of a pair-wise symmetry), in the case of many cilia the tangential terms (S_{ij}) do not vanish and hence contribute to evolution of the phase differences.

To further simplify the system, we now consider a chain of cilia which are equally distributed around the body and hence the angle between any two cilia is $\theta_{ij} = 2\pi(i-j)/N$. By direct substitution into Eq. (6.19), one can show that an equal phase-difference, Δ^{eq}, between all neighboring cilia is a fixed point of Eq. (6.19). Because the system is periodic (in θ), the sum of the phase differences must be an integer multiple of 2π,

$$\Delta^{\text{eq}} N = 2\pi M, \tag{6.20}$$

where $M \in \mathbb{Z}$ for which there are only N unique solutions (due to periodicity in ϕ), synchronized (when $M = 0$) or metachronal waves (when $M \neq 0$).

The strength of the interactions between a pair of cilia decays rapidly as their distance increases, due both to the d_{ij}^{-3} term as well as the effect of the angle, thus, we perform a linear stability analysis of these equilibrium states of the system considering only nearest neighbor interactions. Without loss of generality, we assume $-\pi \leq \Delta^{\text{eq}} \leq \pi$. Using Gaussian elimination, we determined the maximum eigenvalues of the Jacobian at Δ^{eq}, as

$$\lambda_1 = 4d_{12}^{-3}\Theta_{12}\Big[(\rho/\kappa)(\alpha \text{sgn}[\cos\Delta^{\text{eq}}] - 2)\cos\Delta^{\text{eq}} + \alpha\rho\sin|\Delta^{\text{eq}}|\Big], \tag{6.21}$$

where $\alpha(N) \in [0, 2)$ is a constant which depends on the number of cilia as shown in Fig. 6.5. As an example, when $N = 3$ the angle between each pair of cilia is $2\pi/3$. In this case $\alpha = 0$ hence the system has a stable equilibrium only if $\cos\Delta^{\text{eq}} > 0$ and of the possible solutions $\Delta^{\text{eq}} = 0, \pm 2\pi/3$ only $\Delta^{\text{eq}} = 0$ is stable. When the cilia are all in-phase, $\Delta^{\text{eq}} = 0$, $\lambda_1 < 0$ for any N, indicating asymptotic stability of the synchronized state for any number of identical, evenly distributed cilia on a spherical ciliate provided the system has finite flexiblity. In the rigid limit, $\kappa \to \infty$, the largest eigenvalue is zero which causes a loss of stability of the synchronized state (as shown in numerical simulations).

For a system to form metachronal waves, a non-zero equilibrium phase difference between the cilia is required. However, one can show directly that if $\pi/2 \leq |\Delta^{\text{eq}}| \leq \pi$, $\lambda_1 > 0$ while when $0 \leq |\Delta^{\text{eq}}| < \pi/2$ for stability one must have the integer

$$M < \frac{N}{2\pi}\tan^{-1}\left(\frac{2-\alpha}{\alpha\kappa}\right), \tag{6.22}$$

which is satisfied only by $M = 0$ for $\kappa > 1$ (and here $\kappa \gg 1$). Thus, all non-zero values of M (metachronal waves) are linearly unstable for any number of identical, evenly distributed cilia on a spherical ciliate. Unlike the reported results for the chain of cilia near a flat boundary [141], this system cannot form a stable metachronal wave and all the cilia eventually synchronize. The synchronization of

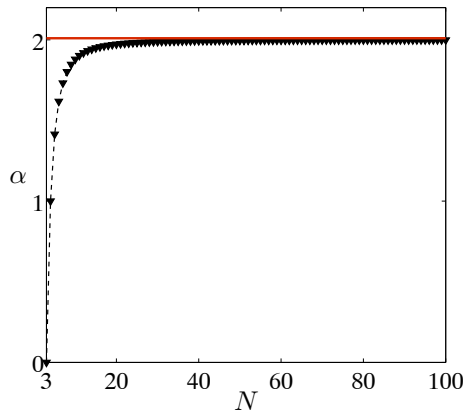

Figure 6.5: The value of the coefficient α, which dictates the stability of fixed points of a ciliary chain, is shown as a function of the given number of cilia N.

two chains of $N = 10$ and $N = 15$ cilia from random initial conditions has been illustrated numerically in Fig. 6.6.

In real biological examples one can hardly expect perfect symmetry and uniformity in the system so it is important to understand the effect of an imposed asymmetry on the stability of this system. There are several well documented sources of asymmetry, from biochemical noise [67, 195], to the different intrinsic properties of a developing cilium [68, 83] or even the addition of a transverse external flow [80] which have all been found to spontaneously affect the behavior of a ciliary system. In particular, the beating rate of a developing cilium fluctuates as it grows, which can perturb the equilibrium state of the system [83]. To analyze this phenomenon, we impose an asymmetry on the system by increasing the intrinsic velocity of cilium (1) to $1 + \Delta\omega$, where we assume $\Delta\omega \ll 1$. The evolution

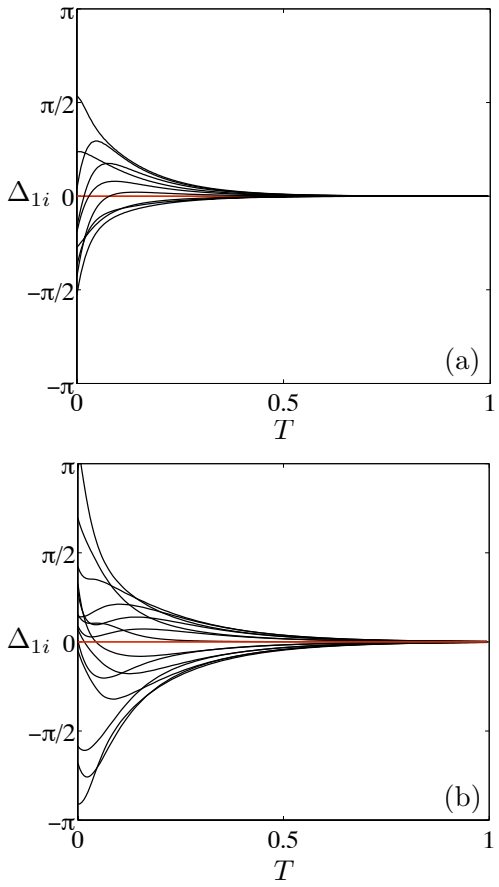

Figure 6.6: Synchronization of a chain of (a) 10 and (b) 15 identical cilia distributed uniformly around a spherical body, with the random initial phases. Each line indicates the evolution of the phase difference for each cilium i compared to cilium (1), $\Delta_{1i} = \phi_1 - \phi_i$, over the time $T = t/(\kappa/\rho)$. These plots are the numerical evaluation of Eq. (6.18) at the characteristic values of $\rho = 3.6{\times}10^{-6}$, $\kappa = 100$ and $\bar{\tilde{\omega}} = 20\pi$ rad.s^{-1} [27, 143].

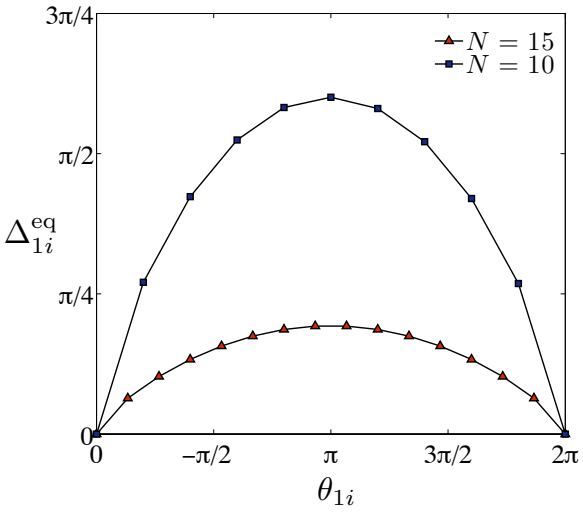

Figure 6.7: Phase differences of nearby cilia in a chain of 10 and 15 cilia around a spherical body when the intrinsic angular velocity of cilium (1) is higher compared to the other cilia by $\Delta\omega = 10^{-6}$ for both cases.

equations for the phase differences are then

$$\begin{aligned}\dot{\bar{\Delta}}_{1i} &= \Delta\omega \\ &+ 4\rho \sum_{m\neq 1}^{N}\sum_{j\neq i}^{N}\left(d_{1m}^{-3}\Theta_{1m}\cos\bar{\Delta}_{1m} - d_{ij}^{-3}\Theta_{ij}\cos\bar{\Delta}_{ij}\right) \\ &- \frac{4\rho}{\kappa}\sum_{m\neq 1}^{N}\sum_{j\neq i}^{N}\left(d_{1m}^{-3}\Theta_{1m}\sin\bar{\Delta}_{1m} - d_{ij}^{-3}\Theta_{ij}\sin\bar{\Delta}_{ij}\right). \qquad (6.23)\end{aligned}$$

Now, due to the imposed asymmetry, the system no longer converges to a synchronized state where phases are equal. There must be a non-zero equilibrium phase difference between cilium (2) and cilium (1) (for example) to balance the difference in the intrinsic velocities. However, the effect of the imposed asymmetry becomes weaker as the distance from cilium (1) increases and, therefore, the phase difference between a two adjacent cilia decreases. These phase differences form a coordinated system of beating, which is illustrated in Fig. 6.7 for two sample cases of $N = 10$ and $N = 15$.

These results indicate that the system responds to this asymmetry through an emergent wave-like behavior. Since this asymmetry arises from any developing cilium in the chain, these waves can originate from different parts of the ciliate and vanish once the beating rate of the developing cilium reaches the frequency of the other cilia. Here we should note that unlike metachronal waves which have $\sim 7-10$ cilia per wavelength [127, 203], the asymmetry-induced behavior has a characteristic wavelength which spans the entire chain of N cilia. Furthermore, as N increases, the strength of the imposed asymmetry becomes weaker and the equilibrium phase differences of the cilia decrease. Thus, the amplitude of such waves is inversely proportional to the number of cilia in the chain, as shown in Fig. 6.7.

6.5 Conclusion

In this chapter, we used a minimal model to capture the dynamics of cilia on a spherically shaped microorganism. We showed that, similar to the case of cilia above a flat wall, elasto-hydrodynamic interactions can lead to synchronization, however here the interactions are additionally mediated due to the geometry of the ciliate body.

For a chain of identical cilia uniformly distributed around a spherical boundary, we showed that the natural periodicity in the geometry of the ciliate leads the system to synchronize. We also showed that in this system, metachronal waves are strictly unstable fixed points of the dynamical system unlike in the case of interaction above a flat wall. This result suggests that the geometry of the ciliate plays a crucial role in the behavior of the ciliary chain and it has to be accounted for when analyzing microorganisms with curved bodies and suggests that a natural extension of this analysis would be to investigate a distrubtion of cilia over the whole surface of the ciliate. Our results also suggest that to form stable metachronal waves, rotation and translation of the ciliate [57], elasticity of the cell-internal fibers connecting the cilia [159], or motion of the cilia perpendicular to the ciliate body [22], may be necessary in such microorganisms. We also reported a wave-like response of the system when one of the cilia is intrinsically faster. In this case, the neighboring cilia display stable phase-locking with the faster cilium with a phase difference

that decreases with distance from the asymmetry. Although the characteristics of this asymmetry-induced phenomenon do not match metachronal waves, we should note that in real ciliary chains there are likely many cilia of differing lengths or biochemical noise which may lead to more complex dynamics in biological systems.

Chapter 7

Dynamics of poroelastocapillary rise

7.1 Introduction

Interactions of capillary forces and elastic materials are abundant in nature: Bundle formations in bristles of a wet painting brush or in wet eyelashes [14, 46], strong hydrophobic interactions of the feathers of aquatic birds [164], or the fluid-mediated adhesion of a beetle to a substrate [48] are just a few examples amongst the many. These interactions, referred to as elastocapillary effects, have shown to be a key factor in collapsing [126] or fabricating [32, 114] engineered microstructures, in the lubrication of soft materials [89, 176] and can be exploited for ultra-thin whitening [29]. Our understanding of capillary rise dates back to experiments of Newton (1704), Jurin (1712), and the analysis of Laplace (1805). When a small tube is in contact with a wetting fluid, capillary forces drive the liquid into the tube until they are balanced by the gravitational forces. In a seminal work, Washburn [197] showed that in capillary rise the balance of surface tension forces and viscous dissipation governs the rate of fluid motion.

The coupling of surface tension forces and elastic forces can lead to surface deformations when liquid is in contact with elastic media, for instance by forming wrinkles [90] or a ridge [150]. In particular, capillary-induced self-assembly of thin flexible materials has attracted extensive attention, owing to recent developments

in micro- and nano-engineering (see [15] and the references therein). To shed some light on such interactions, Kim and Mahadevan [96] notably studied the capillary rise of a liquid between two flexible sheets, clamped at one end and free at the other, and analytically characterized the equilibrium configurations. Duprat et al. [47] then complemented this analysis by looking into sheet deformation prior to equilibrium and developed a framework for capturing the dynamical behavior of this elastocapillary rise (see also [7]). Subsequently, several studies have further extended this model by, for instance, investigating its multiple equilibria [187], considering a series of sheets [60, 174] or by employing the model to enhance the capillary flow in microchannels [6]. In all of these studies, the sheets have been taken as impermeable entities whose properties remain constant upon wetting. For example, paper sheets are often permeable as liquid may diffuse through and change their properties significantly [112]. For instance, water softens a paper napkin as it flows between the plies, which may affect its absorbency. Given that such absorbency is important in paper products used in household and diagnostic applications [128], here we try to quantify the effect of sheet permeability on elastocapillary rise, as a simple model of, for instance, flow between plies of a paper towel.

Paper consists of multiple layers of cellulose fibers. Each fiber has an internal cavity of half of its size, and the surrounding wall is closely packed with hydrophilic microfibrils [189]. When infiltrated by water, before filling the cavities, the liquid diffuses within the microfibrils and causes expansion and swelling [55]. Imbibition of water into cellulose sponges [82, 103], swelling of two parallel sheets submerged into a liquid bath [88], and self-rolling of a piece of paper immersed into water [163] are all examples of this phenomenon. In a recent study, Lee et al. [112] characterized deformation and stiffness of a strip of a paper when it imbibes a stain of water due to surface tension forces. They showed that by absorbing water, the paper sheet swells, increasing its thickness by $\sim 25\%$, while simultaneously decreasing its Young's modulus from $\hat{E} = 828$ MPa to $\hat{E} = 24$ MPa. This significant change of stiffness, which occurs due to imbibition of water by fiber-based materials, can alter the papers absorptivity, and so is quite important in painting [28] and diagnostic applications [129]. Thus, to understand the effect of this permeability on capillary rise, in this chapter, we consider the elastocapillary rise of a liquid (e.g., water)

between two paper sheets. The paper sheets are permeable and they become softer as the liquid rises and permeates through. To study the system's behavior, we closely follow the work of Duprat et al. [47], but modify their model to incorporate the permeability of the sheets by allowing the properties to change upon liquid imbibition. We discuss the dynamics of sheet deformation and the equilibrium states, and compare them with those of impermeable sheets. We show that due to the softening of the sheets, the absorbency of the system with permeable sheets is reduced compared to the system with impermeable ones.

The outline of this chapter is as follows. In Section 7.2, we present the details of the system and perform a scaling analysis. In Section 7.3, we derive evolution equations for the sheet deformation and the meniscus position. We then solve these equations using a finite difference scheme given in Section 7.4. Finally, in Section 7.5, we discuss the results, compare them with those of impermeable sheets and our experimental observations.

7.2 Problem Statement

We are interested in the capillary rise of a viscous fluid between two permeable elastic paper sheets. We consider sheets of length $\hat{l}$, thickness $\hat{b}$, width $\hat{w}$ and assume they are separated initially by distance $2\hat{h}_0$, as shown in Fig. 7.1(a). The sheets are clamped at the upper end (i.e., $\hat{z} = \hat{l}$) and immersed into the liquid bath from the lower free end (i.e., $\hat{z} = 0$). The liquid then rises vertically (in $\mathbf{e}_z$) and we refer to the meniscus position as $\hat{z}_m$. The sheets are elastic and deform as the liquid rises and we quantify the deflections by $\hat{h}(\hat{z}, \hat{t})$ which varies from $\hat{h}_0$ (no deflection) to zero (coalescence). The behavior of the system is dominated by three forces: surface tension forces drive the flow, gravitational forces resist the rise of the liquid, and finally the elastic forces account for the sheet deformations. We characterize these forces using two dimensionless groups, namely the elastocapillary number $\mathcal{E}$, which compares surface tension forces to elastic forces, and the Bond number $\mathcal{B}$,

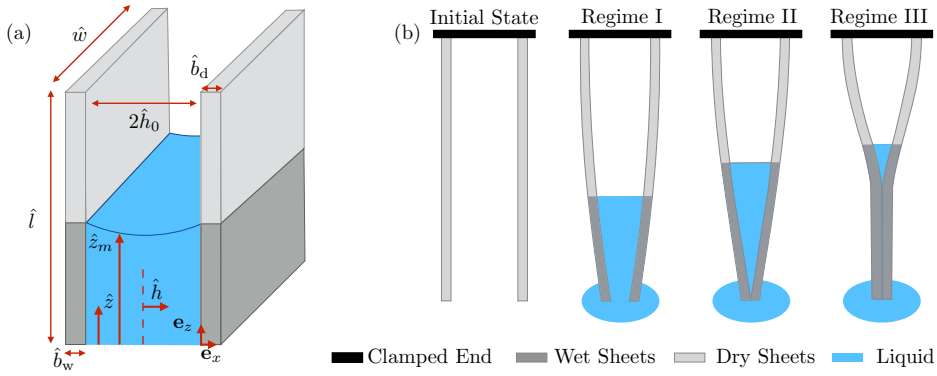

Figure 7.1: The schematic of the system: (a) Two poroelastic sheets clamped at the upper end are immersed into a liquid bath from the lower end. (b) Three scenarios of the equilibrium. In regime I, sheets only slightly bend. In regime II, sheets lower end are in contact and in regime III, sheets coalesce over a finite length.

which compares the effects of gravity and surface tension. We define

$$\mathcal{E} = \frac{\hat{\gamma}\hat{l}^4}{\hat{B}\hat{h}_0^2}, \tag{7.1}$$

$$\mathcal{B} = \frac{\hat{\rho}\hat{g}\hat{l}\hat{h}_0}{\hat{\gamma}}, \tag{7.2}$$

where $\hat{\gamma}$ is the surface tension, $\hat{\rho}$ is density, $\hat{g}$ is the magnitude of gravitational acceleration, and $\hat{B} = \frac{1}{12}\hat{E}\hat{b}^3$ is the bending stiffness per unit width with $\hat{E}$ being the Young's modulus of the sheet. Duprat et al. [47] showed that depending on values of $\mathcal{B}$ and $\mathcal{E}$, the system can exhibit three different configurations: the sheets bend but do not touch ($\hat{h}(\hat{z}=0) > 0$, regime I), they deflect such that they touch but do not coalesce ($\hat{h}(\hat{z}=0) = 0$ and $\frac{\partial \hat{h}}{\partial \hat{z}}(\hat{z}=0) \neq 0$, regime II), or they coalesce over a finite length (regime III), as shown in Fig. 7.1(b).

Since the sheets are permeable, as liquid rises due to surface tension forces, it also permeates through the sheets and changes their properties. Thus, to account for such changes, in our model we consider different properties for wet and dry parts of the sheets and henceforth refer to them using subscripts 'w' and 'd' as

$\left\{\hat{B}_w, \mathcal{E}_w, \hat{b}_w, \cdots\right\}$ and $\left\{\hat{B}_d, \mathcal{E}_d, \hat{b}_d, \cdots\right\}$.

Scaling analysis

This dynamical system involves several time scales and to simplify the problem it is important to compare them. The classic time scale over which fluid rises ($\hat{\tau}_r$), is found by employing a steady unidirectional (Poiseuille) flow field $u = \Delta\hat{p}\hat{h}_0^2/(3\hat{\mu}\hat{l})$ and noting that at equilibrium pressure must balance gravity $\Delta\hat{p} = \hat{\rho}\hat{g}\hat{l}$ and that the pressure is set by surface tension $\Delta\hat{p} = \hat{\gamma}/\hat{h}_0$ so that capillary rise time scale $\hat{\tau}_r = \hat{l}/\hat{u} = 3\hat{\mu}\hat{\gamma}/\hat{h}_0^3(\hat{\rho}\hat{g})^2$. When the elastic deformation of the sheets is appreciable, Duprat et al. [47] argued that the pressure scale is instead set by the deflection of the sheets $\Delta\hat{p} = \hat{B}\hat{h}_0/\hat{l}^4$ so that in this case the 'visco-elastic' time scale $\tau_{ve} = \hat{l}/\hat{u} = 3\hat{\mu}\hat{l}^6/\hat{B}\hat{h}_0^3 = \mathcal{B}^2\mathcal{E}\hat{\tau}_r$. Duprat et al. [47] found that this occurs when $\mathcal{B}^2\mathcal{E} \gtrsim 10$. Furthermore, at the moment when the sheets touch the liquid, inertia is clearly not negligible, and in fact dominates the capillary rise [160]. Das et al. [34] showed that this inertia-dominated regime prevails at $\hat{t} < \hat{\tau}_c$, where $\hat{\tau}_c = \sqrt{\hat{\rho}\hat{h}_0^3/\hat{\gamma}}$ (see also [33]). In our problem fluid also permeates through thickness of the sheet as well as through the sheet vertically. Considering Washburn-like behavior for the fluid permeation in the sheet [197] the time scale for lateral fluid permeation $\hat{\tau}_{\mathrm{D},x} = \hat{b}^2/\hat{D}_w$ and vertical fluid permeation $\hat{\tau}_{\mathrm{D},z} = \hat{l}^2/\hat{D}_w$, where $\hat{D}_w$ is the isotropic diffusion coefficient of the paper.

To compare these time scales, we use properties of a filter paper sheet reported in [112] and consider water as the viscous fluid. We also take $\hat{l} = 1$ cm and $\hat{h}_0 = 0.5$ mm as typical values for the sheet length and gap size, respectively. We find $\hat{\tau}_c/\hat{\tau}_r \sim 10^{-2}$, so we may neglect the effect of inertia since it vanishes very fast. We also find $\hat{\tau}_{\mathrm{D},x}/\hat{\tau}_r \sim 10^{-2}$ indicating that fluid diffuses through the thickness of the sheet considerably faster than the capillary rise. Thus, we assume liquid permeates the sheet (in its thickness), instantly. We also find $\hat{\tau}_r/\hat{\tau}_{\mathrm{D},z} \sim 10^{-3}$, implying that fluid diffusion along the length of the sheet is very slow and so is negligible at the time scale of the rise. Relying on these scalings, one can assume that paper sheet is wet in the liquid-filled region and dry in the liquid-free region. Thus, given a meniscus position $\hat{z}_m$, we consider properties of the wet paper sheet for $0 \le \hat{z} \le \hat{z}_m$ and dry one for $\hat{z}_m < \hat{z} \le \hat{l}$.

7.3 Governing Equations

Here, we take $\hat{l}$ as the characteristic vertical length scale, $\hat{h}_0$ as the characteristic deflection of the sheet, and $\hat{\tau}_{ve}$ as the characteristic time scale of the problem. We thereby non-dimensionalize all the quantities defining $z = \hat{z}/\hat{l}$, $z_m = \hat{z}_m/\hat{l}$, $h = \hat{h}/\hat{h}_0$, $t = \hat{t}/\hat{\tau}_{ve}$ and $p = \frac{\hat{p}}{\hat{B}_w \hat{h}_0/\hat{l}^4}$. Note that we have dropped the caret notation for the dimensionless parameters. We assume that a reflection symmetry between the sheets is maintained and so we derive the governing equations for one sheet (e.g., the one on the right in Fig. 7.1(a)) and the other side shall be identical. In modeling the system, we closely follow the works of Stone et al. [7, 47], but incorporate the change of properties due to wetting. Since the properties of the sheet have a discontinuity at the meniscus, we treat the wet and dry parts separately and enforce boundary conditions at the interface.

Noting that $\hat{h}_0 \ll \hat{l}$, we employ the lubrication approximation to express the fluid motion. The one-dimensional momentum equation then dictates

$$u = -h_w^2 \left(\frac{\partial p}{\partial z} + \mathcal{B}\mathcal{E}_w \right), \tag{7.3}$$

where u is the vertical component of the meniscus velocity and all variables are averaged across the gap. Although the deflection of the sheet is a continuous function, we differentiate the deflection of the wet (h_w, when $z \leq z_m$) and dry (h_d, when $z > z_m$) parts for clarity. As noted earlier, the time scale of the liquid permeation through the sheet thickness is considerably smaller than the one of the rise. Thus, one can assume that the liquid saturates the sheets thickness instantly as the meniscus rises. Furthermore, because the sheet is very thin ($\hat{b}_w \ll \hat{h}_0$), we neglect the mass of liquid permeated within the sheet. One-dimentional mass conservation then yields

$$\frac{\partial h_w}{\partial t} + \frac{\partial}{\partial z}(h_w u) = 0. \tag{7.4}$$

Provided the sheet is sufficiently thin and long (i.e., $\hat{b} \ll \hat{w} \ll \hat{l}$), we may use linear

elasticity to approximate the quasi-static sheet deflection

$$p = \frac{\partial^4 h_w}{\partial z^4}. \tag{7.5}$$

Substituting pressure (7.5) to (7.3), we find

$$u = -h_w^2 \left(\frac{\partial^5 h_w}{\partial z^5} + \mathcal{B}\mathcal{E}_w \right), \tag{7.6}$$

which at $z = z_m$ gives the time evolution of the meniscus since $u(z = z_m) = \frac{\mathrm{d}z_m}{\mathrm{d}t}$. Now by making use of Eq. (7.6), we can rewrite the continuity equation (7.4) in terms of h_w and its derivatives as

$$\frac{\partial h_w}{\partial t} = h_w^2 \left(3 \frac{\partial h_w}{\partial z} \frac{\partial^5 h_w}{\partial z^5} + 3\mathcal{B}\mathcal{E}_w \frac{\partial h_w}{\partial z} + h_w \frac{\partial^6 h_w}{\partial z^6} \right). \tag{7.7}$$

For $z > z_m$, there is no pressure gradient across the sheet and so we have

$$0 = \frac{\partial^4 h_d}{\partial z^4}. \tag{7.8}$$

Boundary conditions

To account for the fixed end at $z = 1$, we set $h_d(z = 1) = 1$ and $\frac{\partial h_d}{\partial z}(z = 1) = 0$. At the lower end ($z = 0$), we note that there exists no net pressure or moment on the sheet so $\frac{\partial^4 h_w}{\partial z^4}(z = 0) = \frac{\partial^2 h_w}{\partial z^2}(z = 0) = 0$. Furthermore, in regime I, wherein sheets cannot apply any force on each other $\frac{\partial^3 h_w}{\partial z^3}(z = 0) = 0$. In regime II, the sheets are no longer force free at $z = 0$ but instead we have $h_w(z = 0) = 0$. For regime III, this boundary condition changes to $h_w(z = z_c) = 0$ and $\frac{\partial h_w}{\partial z}(z = z_c) = 0$, where z_c is the length of the coalescence (i.e., $h_w(z < z_c) = 0$).

At the interface $z = z_m$, continuity of sheet deflection and its slope are enforced by $h_w(z = z_m) = h_d(z = z_m)$ and $\frac{\partial h_w}{\partial z}(z = z_m) = \frac{\partial h_d}{\partial z}(z = z_m)$. Force and moment must also be continuous across the interface, thus $B_w \frac{\partial^3 h_w}{\partial z^3} = B_d \frac{\partial^3 h_d}{\partial z^3}$, and $B_w \frac{\partial^2 h_w}{\partial z^2} = B_d \frac{\partial^2 h_d}{\partial z^2}$. Finally, due to surface tension forces, there exists a pressure jump at the meniscus, which can be found using the Young-Laplace equation [37] and can be

written in dimensionless form as

$$\frac{\partial^4 h_w}{\partial z^4} - \frac{\partial^4 h_d}{\partial z^4} = -\frac{\mathcal{E}_w}{h_w}, \tag{7.9}$$

where we assume the contact angle is zero and neglect the effects of a dynamic contact angle.

In summary, we have a coupled system of sixth-order non-linear Partial Differential Equations (PDEs) subjected to two boundary conditions at the clamped end, three (or four in regime III) conditions at the free end and one condition accounting for the pressure jump at the meniscus. Additionally, we have four continuity conditions that need to be satisfied at the interface.

To solve this problem numerically, it is convenient to incorporate the dynamics of the liquid-free region into the boundary conditions for the liquid-filled region, given the simplicity of the governing equations in the liquid-free region [7, 47]. To illustrate, from Eq. (7.8), one can find the deflection and the slope at the liquid-free region as

$$h_d = A_3 z^3 + A_2 z^2 + A_1 z + A_0, \tag{7.10}$$

$$\frac{\partial h_d}{\partial z} = A_6 z^2 + A_5 z + A_4, \tag{7.11}$$

where A_0 to A_6 are determined using the boundary conditions at the fixed end ($z = 1$) and the interface ($z = z_m$). h_d and $\frac{\partial h_d}{\partial z}$ are then found in terms of h_w and its derivatives at $z = z_m$ as

$$h_d(z) = 1 + \frac{B_r}{6}(1-z)^2\left[3\frac{\partial^2 h_w}{\partial z^2} + \frac{\partial^3 h_w}{\partial z^3}(z - z_m) + 2\frac{\partial^3 h_w}{\partial z^3}(1 - z_m)\right], \tag{7.12}$$

$$\frac{\partial h_d}{\partial z}(z) = -\frac{B_r}{2}(1-z)\left[2\frac{\partial^2 h_w}{\partial z^2} + \frac{\partial^3 h_w}{\partial z^3}(z - z_m) + \frac{\partial^3 h_w}{\partial z^3}(1 - z_m)\right], \tag{7.13}$$

where $B_r = \frac{B_w}{B_d}$. Noting that $h_w = h_d$ and $\frac{\partial h_w}{\partial z} = \frac{\partial h_d}{\partial z}$ at the interface, we then find

$$h_w(z = z_m) = 1 + \frac{B_r}{3}\frac{\partial^3 h_w}{\partial z^3}(1 - z_m)^3 + \frac{B_r}{2}\frac{\partial^2 h_w}{\partial z^2}(1 - z_m)^2, \tag{7.14}$$

$$\frac{\partial h_w}{\partial z}(z = z_m) = -\frac{B_r}{2}\frac{\partial^3 h_w}{\partial z^3}(1 - z_m)^2 - B_r\frac{\partial^2 h_w}{\partial z^2}(1 - z_m), \tag{7.15}$$

which provides two boundary conditions for h_w at $z = z_m$. Now, the governing equations in the liquid-filled region are independent of h_d, and so we can determine the behavior of the sheet by solely solving the system for $z \leq z_m$. Once h_w is found, we use Eq. (7.12) to find the deformation for the whole sheet.

7.4 Numerical Approach

At early times, $t \ll 1$, one may consider a quasi-static deformation of the sheet ($\frac{\partial h_w}{\partial t} = 0$) since sheet deflections are very small and time enters the problem only through boundary conditions [47]. We expand the deflection $h_w(z) = \sum_{n=0}^{n=5} C_n z^n + O(z_m^6)$, where $z_m \ll 1$. From the pressure drop at the meniscus given in (7.9), we find $C_5 = -\frac{\mathcal{E}_w}{120 z_m}$. Boundary conditions at $z = 0$ dictate $C_4 = C_2 = 0$ and, recalling that in this limit sheets can only reach regime I, we have $C_3 = 0$. Finally, from the boundary conditions given in (7.14) and (7.15), we arrive at

$$\begin{aligned} h_w = 1 - \frac{\mathcal{E}_w}{120 z_m} z^5 + \left(\frac{\mathcal{E}_w z_m^3}{24} + \frac{\mathcal{E}_d z_m^3}{12} - \frac{\mathcal{E}_d z_m^2}{3} + \frac{\mathcal{E}_d z_m}{4}\right) z \\ + \left(-\frac{\mathcal{E}_w z_m^3}{30} + \frac{\mathcal{E}_d z_m}{6} - \frac{\mathcal{E}_d}{6}\right) z_m + O(z_m^6), \end{aligned} \tag{7.16}$$

which governs the sheet deflection in the liquid-filled region for $t \ll 1$. Substituting h_w from (7.16) in (7.6), we find the leading-order evolution equation for the meniscus as

$$\frac{\mathrm{d}z_m}{\mathrm{d}t} = \frac{\mathcal{E}_w}{z_m} - \mathcal{B}\mathcal{E}_w. \tag{7.17}$$

To solve the dynamical system in full, we use Eqs. (7.16) and (7.17) for early times, and then to determine the behavior of the system at later times, we follow the work of Aristoff et al. [7] and implement an implicit finite-difference scheme that is second-

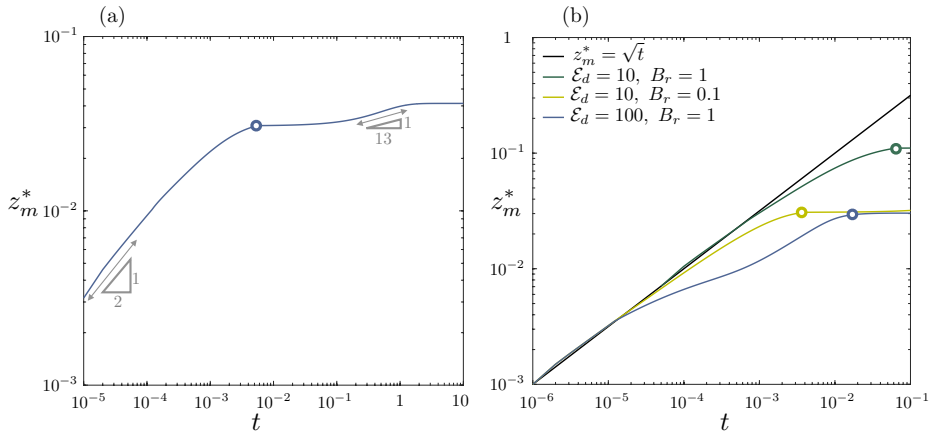

Figure 7.2: The time evolution of rescaled meniscus, $z_m^* = \sqrt{B_r/(2\mathcal{E}_d)}z_m$: (a) Permeable sheets with $\mathcal{B} = 2$, $\mathcal{E}_d = 10$ and $B_r = 0.1$. (b) Two impermeable sheets with $\mathcal{E}_d = 10$ and $\mathcal{E}_d = 100$ and permeable sheets with $\mathcal{E}_d = 10$ (or $\mathcal{E}_w = 100$). In (b), for all cases $\mathcal{B} = 3$ and solid black line refers to the classical capillary rise [197]. Circles on each line indicate the time in which sheets reach regime II ($h(t, z = 0) = 0$).

order accurate in space and first-order accurate in time. To resolve the nonlinear terms in Eqs. (7.6) and (7.7) (e.g., $h_w^2 \frac{\partial h_w}{\partial z} \frac{\partial^5 h_w}{\partial z^5}$), we discretize the higher-order term ($\frac{\partial^5 h_w}{\partial z^5}$) and then use the results of the previous time-step for the lower-order terms (h_w and $\frac{\partial h_w}{\partial z}$). We repeat the procedure iteratively until the relative convergence error reaches below 10^{-5}. We discretize the sheet length in the liquid-filled region using 30 points and take $\Delta t = 10^{-3}$ as the typical time step. Recalling that in the scale of the considered problem we found $\hat{\tau}_c/\hat{\tau}_r \sim 10^{-2}$, we neglect inertia and take $h_w(t = 0) = 1$ (zero deflection) and $z_m(t = 0) = 10^{-3}$ (negligible inertial meniscus rise) as initial conditions.

7.5 Results and Discussion

At early times ($t \ll 1$) when the sheet deflection is not yet significant, elasticity does not contribute to the dynamics of the meniscus, nor does the permeability of sheet. Thus, regardless of the values of $\mathcal{E}_d$ and B_r $\left(= \frac{B_w}{B_d} = \frac{\mathcal{E}_d}{\mathcal{E}_w}\right)$, the meniscus strictly follows the classical behavior of a simple capillary rise in a rigid channel given by

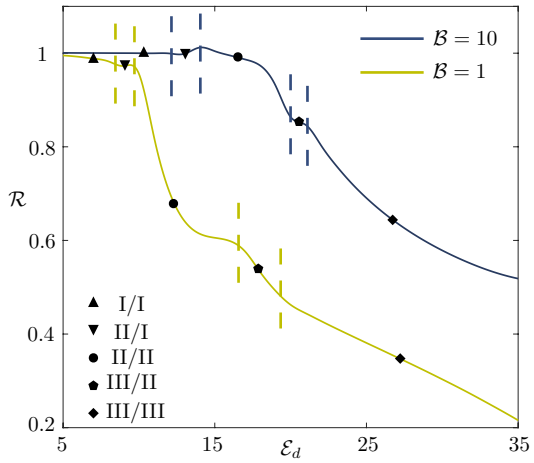

Figure 7.3: The liquid absorption ratio, $\mathcal{R}$, of permeable sheets compared to impermeable ones of the same $\mathcal{E}_d$ for $\mathcal{B} = 1$ and $\mathcal{B} = 10$. Dashed lines separate the different combinations of equilibrium regimes for permeable and impermeable cases and symbols denote the regimes (e.g., II/I indicates that permeable sheets reach regime II while impermeable sheets are at regime I).

$z_m = \sqrt{2\mathcal{E}_w t}$ (note that in the dimensional form $\mathcal{E}_w$ disappears). Defining a rescaled meniscus position as $z_m^* = \sqrt{1/(2\mathcal{E}_w)}z_m$ (or equivalently $z_m^* = \sqrt{B_r/(2\mathcal{E}_d)}z_m$), one can see from Fig. 7.2(a) that $z_m^* = \sqrt{t}$ predicts the initial behavior of z_m^* quite accurately. This behavior can also be explained using the asymptotic expressions given in (7.16) and (7.17). At leading order, we find $h_w = 1$ indicating no deflection and so the problem is reduced to capillary rise between two rigid sheets. Furthermore, since at early times $z_m \ll 1$, meniscus dynamics can be approximated to leading order as $\mathrm{d}z_m/\mathrm{d}t = \mathcal{E}_w/z_m$ (or $\mathrm{d}z_m^*/\mathrm{d}t = 1/(2z_m^*)$) confirming the diffusive behavior. At later times, the sheet deformation becomes appreciable and the meniscus position no longer follows the classical capillary-rise predictions. Once the lower ends of the sheets are in contact (denoted by a circle in Fig. 7.2(a)), after a short period of almost stationary position, the meniscus rises with $z_m^* \sim t^{1/13}$, and then finally reaches the equilibrium.

We now compare the dynamics of the permeable sheets with impermeable cases. As noted earlier, for $t \ll 1$, one can neglect the effect of elasticity and permeability and so all the cases identically follow the classical behavior. For impermeable sheets, as the elastocapillary number increases, the effect of bending becomes more dominant and the meniscus position deviates from $z_m^* = \sqrt{t}$ sooner. But in permeable sheets, the time evolution of meniscus is dictated by elastocapillary numbers of both the dry region (e.g., $\mathcal{E}_d = 10$) and the wet region (e.g., $\mathcal{E}_w = 100$). Meniscus deviation from the classical behavior thereby lies within two cases of impermeable sheets with bounding elastocapillary numbers ($\mathcal{E}_d = 10$ and 100), as can be seen in Fig. 7.2(b). However interestingly, the permeable sheets reach regime II ($h_w(z = 0) = 0$) faster than both bounding cases (denoted by circles in Fig. 7.2(b)).

Note that the system can only collect liquid while $h_w(z = 0) > 0$; once the lower ends of sheets touch ($h_w(z = 0) = 0$), further rise of the liquid is purely due to sheet deflection as the liquid in the bath can no longer flow into the system. This behavior may indicate that permeable sheets have less time to capture the liquid. To better highlight this point, in Fig. 7.3 we have reported the absorption ratio of permeable sheets to impermeable sheets, $\mathcal{R}$, by determining the area of the risen liquid between the sheets at equilibrium. As noted earlier, for small values of elastocapillary number, for which both cases reach regime I, the sheets only slightly bend. The effect of permeability is thereby not significant and the absorption ratio is nearly one. For permeable sheets, as the value of elastocapillary number increases, the sheets deflect more readily in response to the capillary rise. Thus, the softening of the sheets due to wetting facilitates this bending and leads the sheets to coalesce faster, thereby decreasing the absorption ratio. For instance, when $\mathcal{E}_d = 35$, this ratio drops to $\sim 40\%$ for $\mathcal{B} = 10$ and $\sim 20\%$ for $\mathcal{B} = 1$ in regime III.

Recall that Duprat et al. [47] found that for impermeable sheets when $\mathcal{B}^2\mathcal{E}_d \gtrsim 10$ the time scale for the capillary rise is set by the deformation of the sheets, $\hat{\tau}_{ve}$. We find here, surprisingly, that despite the discontinuity of $\mathcal{E}$ at the meniscus, permeable sheets exhibit the same behavior for $\mathcal{B}^2\mathcal{E}_w \gtrsim 10$, as shown in Fig. 7.4 (note that in our dimensionless units $t = 1$ is $\hat{t} = \hat{\tau}_{ve}$). This result indicates that when the sheets are sufficiently flexible, the equilibrium time scale for permeable sheets is dominantly dictated by the properties of the liquid-filled region, and the dry region

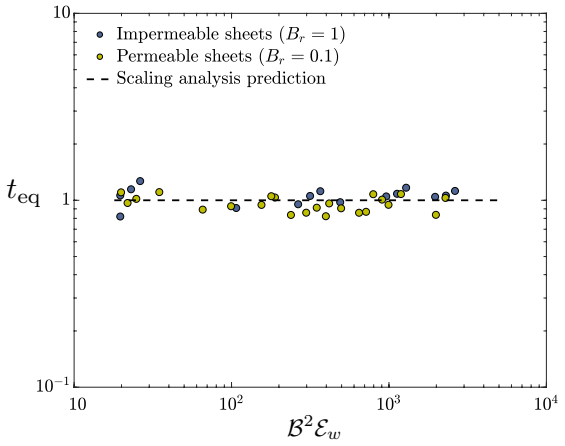

Figure 7.4: Time to reach the 99% of the equilibrium height versus $\mathcal{B}^2\mathcal{E}_w$. Symbols represent the numerical results for the equilibrium time scale of impermeable and permeable sheets. The dashed line indicates $t_{\rm eq} = 1$.

has no appreciable contribution.

In Fig. 7.5(a), the regime map for permeable sheets with $1 < \mathcal{B} < 10$ and $1 < \mathcal{E}_d < 10^2$ is illustrated. Unlike the case of impermeable sheets wherein for some values of elastocapillary number (i.e., $10 \lesssim \mathcal{E}_d \lesssim 30$) regimes I and II coexist [47], here the three regimes are distinct, which may be caused by further softening of the sheets due to wetting and their higher tendency to coalesce. Recall that higher Bond numbers can indicate larger gaps, so one can argue that sheets need to bend more to touch (regime II) or coalesce (regime III). Thus, reaching regime II and III is more difficult when the Bond number ($\mathcal{B}$) is large. Indeed, as shown in Fig. 7.5(a), our numerical results show that when the gap (or similarly $\mathcal{B}$) is large, reaching coalescence requires longer sheets which indicates higher values of elastocapillary number. We note that this is in contrast to impermeable sheets for which when the gap is large, coalescence is more easily obtained for shorter sheets [47].

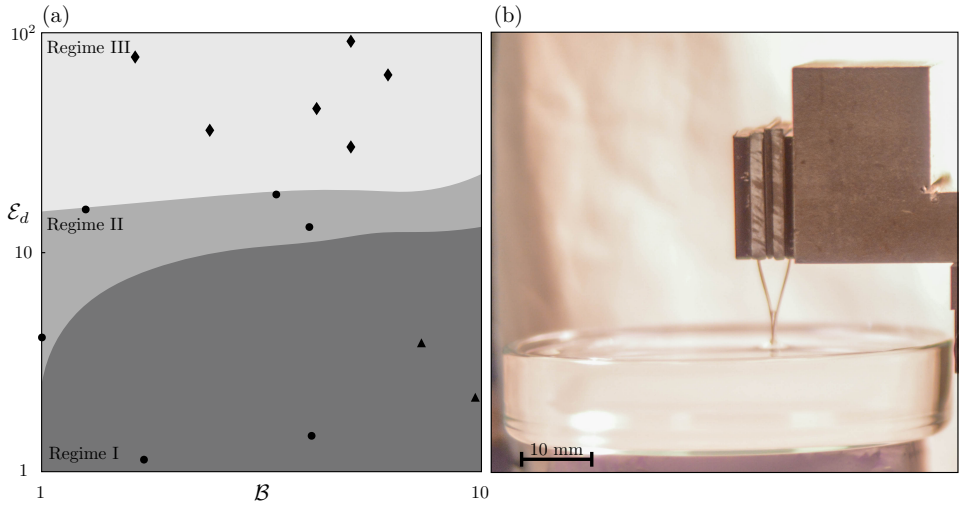

Figure 7.5: (a) Regime map for the equilibrium sate of permeable sheets in a logarithmic $(\mathcal{B}, \mathcal{E}_d)$ space. Each shade refers to its specified regime and is obtained using the numerical scheme discussed in Section 7.4. Symbols are the equilibrium states observed experimentally: Triangles (▲) denote regime I, circles (●) indicate regime II and diamonds (♦) refer to regime III. (b) The experimental apparatus. Sheets here are in regime III.

Finally, in deriving the governing equations, we neglected the vertical liquid permeation within the sheet as it occurs on a longer time scale than the capillary rise. But, once the system reaches the equilibrium, the contribution of this upward permeation becomes significant, and the system then further evolves until the sheets are fully wet.

Experimental observations

We compare our numerically-obtained regime map with experimental observations. We use filter papers (Whatmann grade 1) that we clamp at the upper end using rare-earth magnets, and set the initial gap using steel shims of varying thicknesses, as shown in Fig. 7.5(b). We slowly immerse the sheets into a water bath and capture the equilibrium state using a digital camera. We report our observations for various combinations of Bond numbers and elastocapillary numbers in Fig. 7.5(a)

(symbols in the figure). We see that our numerical model is in good agreement with the experiments in predicting regime III. However, the model predictions and the experimental results deviate from each other at lower values of elastocapillary number for which the numerical model predicts regime I, while in the experiments, sheets surprisingly reach regime II. We believe that this discrepancy can arise from the inertial effects which were neglected in our model. To examine regime I, the system should have a low elastocapillary number. Noting that in our experiments we can only tune $\hat{h}_0$ and $\hat{l}$, we experimentally obtain low values for the elastocapillary number by increasing the initial gap between the sheets (see Eq. (7.1)). But, the time scale of inertial effects $\hat{\tau}_c$ scales as $\sim \hat{h}_0^{3/2}$, and so it becomes more important when $\hat{h}_0$ increases. Specifically, for gap values of order ~ 2 mm, the time scale of inertial effects is of the same order as that of the capillary rise. Therefore, for the cases with a large value of the initial gap (which often are in regime I), the effects of inertia is no longer negligible and may contribute to the equilibrium state. In our experiments, we observe that in this regime sheets rapidly (and significantly) bend toward each other at the very beginning and then exhibit the expected elastocapillary rise dynamics thereafter. Due to this initial effect, sheets' lower ends meet more readily and so the system proceeds to regime II.

7.6 Conclusion

In this chapter, we studied the dynamics of capillary rise of a liquid between two flexible permeable paper sheets. Accounting for the change of sheet stiffness due to wetting, we discussed the motion of the meniscus and the sheet deflection as the system reaches the equilibrium. As the liquid rises, it permeates within the sheets and softens them significantly. Noting that the dynamics of the system is governed by both dry and wet regions of the sheets, as a direct consequence of this further softening in the wet region, permeable sheets evolve toward coalescence more readily, compared to impermeable ones. We also showed that the equilibrium time scale of the system is quite similar to those of impermeable sheets, however, the volume of fluid captured between the permeable sheets can be notably lower. The lower ends of permeable sheets meet sooner which means the system has less time to draw liquid in from the bath, and also the sheets are softer and so they

deform significantly in response to the liquid rise. Recalling that, for instance, multi-ply paper towel is a collection of compressed multi-layer permeable sheets, our results indicate that permeability of fibers should be accounted for in modeling capillary-based systems, such as in sorption of oil spills [79, 140] and in designing microfluidic paper-based analytical devices [128, 129]. Given the generality of the considered model, our results can be extended to capture the behavior of a series of permeable sheets [60, 174] and be adapted to study the buckling of papers when they are fixed at both ends.

Chapter 8

Concluding Remarks

In this dissertation, using theoretical approaches, we investigated the effects of elasticity on hydrodynamic interactions at small scales. We started by evaluating the force moments of an arbitrarily-shaped active particle and provided explicit formulas for the stresslet dipole, rotlet dipole, and potential dipole, using the reciprocal theorem. It was then shown that for an elastic swimmer near a boundary the rotlet dipole of the background flow governs the elastic bending of the swimmer, thereby playing a key role in directing the swimmer toward (or away from) the wall. We also demonstrated that an elastic sphere deforms asymmetrically under a body force, and proposed a two-sphere swimmer that can exploit this asymmetry to propel itself forward. Moreover, using a minimal model, we investigated the hydrodynamic interactions of a ciliary chain around a curved body and showed that no wave-like behavior emerges from their interactions unless an asymmetry is introduced to the chain. Finally, we looked at the capillary rise between two elastic porous sheets and quantified their dynamical behavior as the liquid rises and diffuses through the sheets. We demonstrated that, by imbibing the liquid, sheets tend to coalesce faster and so the system absorbs less liquid.

From all these studies, we can conclude that elasticity plays a key role in the dynamical behavior of the system and can alter the hydrodynamic interactions significantly. Our results highlight that elasticity should be accounted for when modeling hydrodynamic interactions in inertialess environments. Nevertheless, there are, inevitably, limitations to the taken methodologies which are worthwhile

to be discussed and can motivate future directions.

In the vast world of microorganisms, the effect of elasticity can be far more complex than what we considered in our studies. The linear elasticity models employed in Chapters 4 and 6 have proven useful in recovering some essential behaviors of microorganisms and revealing the "leading-order" effects of the elasticity. However, they are founded on the assumption of *weak* elasticity which may not be always accurate. For instance, single-celled eukaryotes such as *Euglena* have large body deformations as they swim [167], and many bacteria buckle their flagella, substantially, to change direction [177]. These two phenomena exemplify a class of problems wherein understanding the elastohydrodynamic interactions may require a geometric or constitutive nonlinearity. But, one should note that, as we showed in Chapter 5, using non-linear elastic constitutive equations to express deformations even in a problem as (seemingly) simple as a sedimenting sphere can be quite challenging.

Despite the growing attention devoted to ciliary motion, our understanding of the dynamics of the ciliated microorganisms is still limited. Interactions between the cilia (and flagella) and the formation of wave-like beating patterns have been speculated to be strongly depended on hydrodynamic interactions. Several studies, both theoretically [26, 73] and experimentally [22, 23], have verified that hydrodynamic interactions can indeed lead to the phase-locking of adjacent cilia and flagella. However, in an experimental work, Quaranta et al. [159] revealed that in unicellular interactions of flagella, the coupling forces may be an order of magnitude larger than hydrodynamic forces, indicating a non-hydrodynamic origin for flagellar synchronization [100] such as intracellular elastic basal coupling [196]. This observation triggers the question of how do cilia and flagella interact within the cell body and also what is the contribution of the substrate elasticity to their phase locking? Answering these questions requires a careful examination of the cell body elasticity, which is often neglected in the minimal models used to understand the ciliary motion.

Minimal models may also fail to explain the behavior of more complex ciliated organisms such as larval forms of marine invertebrates. Ciliary bands, other than generating the propulsive thrust [1], have shown to also contribute to the larvae feeding [62, 151]. In a starfish larvae, the body deformation along with the local

vortices generated by the cilia, entrain the nearby prey and facilitate the feeding mechanism [62]. Given that, in such organisms, cilia are closely packed around the ciliate body and may 'tangle' [62], the bead-spring model [141] and far-field approximations can no longer be employed to capture the cilium-cilium interactions. Furthermore, modeling the active shape changes of the larvae is also challenging as it requires a thorough understanding of the internal impetus-generating mechanism.

Given the complexity of the poroelastocapillary rise phenomenon, several assumptions and approximations were made in Chapter 7 that can be lifted to provide a better quantitative model. For instance, the liquid diffusion into the length of the sheets was neglected due to the relatively slow evolution timescale, but should be accounted for when analyzing the equilibrium state of the system. Given the dependency of the capillary rise to the initial conditions [46, 160], inertial effects at early stages of the capillary rise can be important for less viscous fluids. Also, the dynamic contact angle at the meniscus has been shown to have quantitative effects, which should be incorporated into the model when comparing with the experimental results. To better understand the liquid rise within the layers of a paper, and as the natural extension to our study in Chapter 7, one may look into the poroelastocapillary rise of a wetting liquid between series of parallel sheets.

Lastly, in this dissertation, we tried to answer specific questions to better understand the role of elasticity in the microscopic motions in fluids, but yet, there exist several more to ponder. Questions that, we believe, should be answered collectively using experimental observations, computational simulations, and theoretical analysis.

Bibliography

[1] S. Amemiya, T. Hibino, H. Nakano, M. Yamaguchi, R. Kuraishi, and M. Kiyomoto. Development of ciliary bands in larvae of the living isocrinid sea lily *Metacrinus rotundus*. *Acta Zool.*, 96(1):36–43, 2013. → page 89

[2] J. Anderson. Colloid transport by interfacial forces. *Annu. Rev. Fluid Mech.*, 21:61–99, 1989. → page 9

[3] J. L. Anderson and D. C. Prieve. Diffusiophoresis caused by gradients of strongly adsorbing solutes. *Langmuir*, 7:403–406, 1991. → page 23

[4] D. L. Andrews and P. J. Wilkes. Irreducible tensors and selection rules for three-frequency absorption. *J. Chem. Phys.*, 83:2009–2014, 1985. → page 14

[5] D. L. Andrews, N. P. Blake, and K. P. Hopkins. Theory of electro-optical effects in two-photon spectroscopy. *J. Chem. Phys.*, 88:6022–6029, 1988. → page 14

[6] R. Anoop and A. K. Sen. Capillary flow enhancement in rectangular polymer microchannels with a deformable wall. *Phys. Rev. E*, 92(1): 013024, 2015. → page 73

[7] J. M. Aristoff, C. Duprat, and H. A. Stone. Elastocapillary imbibition. *Int. J. Nonlinear Mech.*, 46:648–656, 2011. → pages 73, 77, 79, 80

[8] J. E. Avron, O. Kenneth, and D. H. Oaknin. Pushmepullyou: an efficient micro-swimmer. *New J. Phys.*, 7:234, 2005. → page 42

[9] N. J. Balmforth, D. Coombs, and S. Pachmann. Microelastohydrodynamics of swimming organisms near solid boundaries in complex fluids. *Quart. J. Mech. Appl. Math.*, 63(3):267–294, 2010. → page 30

[10] G. K. Batchelor. The stress system in a suspension of force-free particles. *J. Fluid. Mech.*, 41:545, 1970. → pages 10, 13

[11] G. K. Batchelor and J. T. Green. The hydrodynamic interaction of two small freely-moving spheres in a linear flow field. *J. Fluid Mech.*, 56:375, 1972. → page 58

[12] H. Berg and L. Turner. Chemotaxis of bacteria in glass capillary arrays. escherichia coli, motility, microchannel plate, and light scattering. *Biophys. J.*, 58(4):919–930, 1990. → page 30

[13] A. P. Berke, L. Turner, H. C. Berg, and E. Lauga. Hydrodynamic attraction of swimming microorganisms by surfaces. *Phys. Rev. Lett.*, 101:038102, 2008. → pages 10, 30, 31, 40

[14] J. Bico, B. Roman, L. Moulin, and A. Boudaoud. Adhesion: Elastocapillary coalescence in wet hair. *Nature*, 432(7018):690–690, 2004. → page 72

[15] J. Bico, É. Reyssat, and B. Roman. Elastocapillarity: When surface tension deforms elastic solids. *Annu. Rev. Fluid Mech*, 50(1):629–659, 2018. → page 73

[16] J. R. Blake. A spherical envelope approach to ciliary propulsion. *J. Fluid Mech.*, 46:199–208, 1971. → pages 24, 25, 57

[17] J. R. Blake. A note on the image system for a stokeslet in a no-slip boundary. *Math. Proc. Camb. Philos. Soc.*, 70(02):303, 1971. → pages 35, 60

[18] S. Box, L. Debono, D. B. Phillips, and S. H. Simpson. Transitional behavior in hydrodynamically coupled oscillators. *Phys. Rev. E*, 91:022916, 2015. → page 57

[19] C. Brennen and H. Winet. Fluid mechanics of propulsion by cilia and flagella. *Annu. Rev. Fluid Mech.*, 9:339–398, 1977. → page 56

[20] H. Brenner. The Stokes resistance of an arbitrary particle—IV arbitrary fields of flow. *Chem. Eng. Sci.*, 19:703–727, 1964. → page 54

[21] A. T. Brown, I. D. Vladescu, A. Dawson, T. Vissers, J. Schwarz-Linek, J. S. Lintuvuori, and W. C. K. Poon. Swimming in a crystal. *Soft Matter*, 12(1): 131–140, 2016. → page 30

[22] D. R. Brumley, M. Polin, T. J. Pedley, and R. E. Goldstein. Hydrodynamic synchronization and metachronal waves on the surface of the colonial alga Volvox carteri. *Phys. Rev. Lett.*, 109:268102, 2012. → pages 9, 42, 57, 70, 89

[23] D. R. Brumley, K. Y. Wan, M. Polin, and R. E. Goldstein. Flagellar synchronization through direct hydrodynamic interactions. *eLife*, 3:02750, 2014. → page 89

[24] D. R. Brumley, M. Polin, T. J. Pedley, and R. E. Goldstein. Metachronal waves in the flagellar beating of volvox and their hydrodynamic origin. *J. R. Soc. Interface*, 12:20141358, 2015. → page 57

[25] N. Bruot and P. Cicuta. Realizing the physics of motile cilia synchronization with driven colloids. *arXiv:1510.04714*, 2015. → page 57

[26] N. Bruot, L. Damet, J. Kotar, P. Cicuta, and M. Cosentino Lagomarsino. Noise and synchronization of a single active colloid. *Phys. Rev. Lett.*, 107: 094101, 2011. → pages 57, 89

[27] S. Camalet and F. Jülicher. Generic aspects of axonemal beating. *New J. Phys.*, 2:24–22, 2000. → pages xiii, 59, 68

[28] S. Capodicasa, S. Fedi, A. M. Porcelli, and D. Zannoni. The microbial community dwelling on a biodeteriorated 16th century painting. *Int. Biodeterior. Biodegradation*, 64(8):727–733, 2010. → page 73

[29] D. Chandra, S. Yang, A. A. Soshinsky, and R. J. Gambogi. Biomimetic ultrathin whitening by capillary-force-induced random clustering of hydrogel micropillar arrays. *ACS Appl. Mater. Interfaces*, 1(8):1698–1704, 2009. → page 72

[30] M. Contino, E. Lushi, I. Tuval, V. K., and M. Polin. Microalgae scatter off solid surfaces by hydrodynamic and contact forces. *Phys. Rev. Lett.*, 115 (25), 2015. → page 30

[31] M. Cosentino Lagomarsino, P. Jona, and B. Bassetti. Metachronal waves for deterministic switching two-state oscillators with hydrodynamic interaction. *Phys. Rev. E*, 68:021908, 2003. → page 57

[32] N. B. Crane, O. Onen, J. Carballo, Q. Ni, and R. Guldiken. Fluidic assembly at the microscale: progress and prospects. *Microfluid. Nanofluid.*, 14(3-4):383–419, 2012. → page 72

[33] S. Das and S. K. Mitra. Different regimes in vertical capillary filling. *Phys. Rev. E*, 87(6), 2013. → page 76

[34] S. Das, P. R. Waghmare, and S. K. Mitra. Early regimes of capillary filling. *Phys. Rev. E*, 86(6), 2012. → page 76

[35] C. Datt, L. Zhu, G. J. Elfring, and O. S. Pak. Squirming through shear-thinning fluids. *J. Fluid. Mech.*, 784:R1, 2015. → page 11

[36] C. Datt, G. Natale, S. G. Hatzikiriakos, and G. J. Elfring. An active particle in a complex fluid. *J. Fluid. Mech.*, 823:675–688, 2017. → page 11

[37] P. de Gennes, F. Brochard-Wyart, and D. Quéré. *Capillarity and Wetting Phenomena*. Springer New York, 2004. → page 78

[38] N. Desai, V. A. Shaik, and A. M. Ardekani. Hydrodynamics-mediated trapping of micro-swimmers near drops. *Soft Matter*, 14(2):264–278, 2018. → page 30

[39] M. A. Dias and T. R. Powers. Swimming near deformable membranes at low reynolds number. *Phys. Fluids*, 25(10):101901, 2013. → page 31

[40] C. Dombrowski, L. Cisneros, S. Chatkaew, R. E. Goldstein, and J. O. Kessler. Self-concentration and large-scale coherence in bacterial dynamics. *Phys. Rev. Lett.*, 93:098103, 2004. → page 10

[41] K. Drescher, K. C. Leptos, I. Tuval, T. Ishikawa, T. J. Pedley, and R. E. Goldstein. Dancing *Volvox*: Hydrodynamic bound states of swimming algae. *Phys. Rev. Lett.*, 102:168101, 2009. → page 10

[42] K. Drescher, R. E. Goldstein, N. Michel, M. Polin, and I. Tuval. Direct measurement of the flow field around swimming microorganisms. *Phys. Rev. Lett.*, 105:168101, 2010. → page 10

[43] K. Drescher, J. Dunkel, L. H. Cisneros, S. Ganguly, and R. E. Goldstein. Fluid dynamics and noise in bacterial cell-cell and cell-surface scattering. *Proc. Natl. Acad. Sci.*, 108(27):10940–10945, 2011. → page 30

[44] R. Dreyfus, J. Baudry, and H. A. Stone. Purcell's "rotator": mechanical rotation at low Reynolds number. *EPJ B*, 47:161–164, 2005. → page 42

[45] J. Dunstan, G. Miño, E. Clement, and R. Soto. A two-sphere model for bacteria swimming near solid surfaces. *Phys. Fluids*, 24(1):011901, 2012. → page 30

[46] C. Duprat and H. A. Stone, editors. *Fluid-Structure Interactions in Low-Reynolds-Number Flows*. Royal Society of Chemistry, 2015. → pages 72, 90

[47] C. Duprat, J. M. Aristoff, and H. A. Stone. Dynamics of elastocapillary rise. *J. Fluid. Mech.*, 679:641–654, 2011. → pages 73, 74, 75, 76, 77, 79, 80, 83, 84

[48] T. Eisner and D. J. Aneshansley. Defense by foot adhesion in a beetle (hemisphaerota cyanea). *Proc. Natl. Acad. Sci.*, 97(12):6568–6573, 2000. → page 72

[49] G. J. Elfring. A note on the reciprocal theorem for the swimming of simple bodies. *Phys. Fluids*, 27:023101, 2015. → pages 11, 16, 23

[50] G. J. Elfring. Force moments of an active particle in a complex fluid. *J. Fluid. Mech.*, 829:R3, 2017. → pages 10, 11, 16, 17, 19

[51] G. J. Elfring and E. Lauga. Synchronization of flexible sheets. *J. Fluid Mech.*, 674:163–173, 2011. → pages 42, 57

[52] G. J. Elfring and E. Lauga. Theory of locomotion in complex fluids. In *Complex Fluids in Biological Systems*, pages 285–319. Springer, 2015. → page 17

[53] G. J. Elfring, O. S. Pak, and E. Lauga. Two-dimensional flagellar synchronization in viscoelastic fluids. *J. Fluid Mech.*, 646:505, 2010. → page 57

[54] J. Elgeti, R. G. Winkler, and G. Gompper. Physics of microswimmers—single particle motion and collective behavior: a review. *Rep. Prog. Phys.*, 78:056601, 2015. → pages 10, 57

[55] J. A. Enderby. Water absorption by polymers. *J. Chem. Soc. Faraday Trans.*, 51:106, 1955. → page 73

[56] B. Ezhilan and D. Saintillan. Transport of a dilute active suspension in pressure-driven channel flow. *J. Fluid Mech.*, 777:482–522, 2015. → page 30

[57] B. M. Friedrich and F. Jülicher. Flagellar synchronization independent of hydrodynamic interactions. *Phys. Rev. Lett.*, 109:138102, 2012. → page 70

[58] V. Galstyan, O. S. Pak, and H. A. Stone. A note on the breathing mode of an elastic sphere in Newtonian and complex fluids. *Phys. Fluids*, 27: 032001, 2015. → page 42

[59] T. Gao, H. H. Howard, and P. Ponte Castañeda. Rheology of a suspension of elastic particles in a viscous shear flow. *J. Fluid. Mech.*, 687:209–237, 2011. → page 42

[60] A. D. Gat and M. Gharib. Elasto-capillary coalescence of multiple parallel sheets. *J. Fluid Mech.*, 723:692–705, 2013. → pages 73, 87

[61] S. Ghose and R. Adhikari. Irreducible representations of oscillatory and swirling flows in active soft matter. *Phys. Rev. Lett.*, 112:118102, 2014. → page 10

[62] W. Gilpin, V. N. Prakash, and M. Prakash. Vortex arrays and ciliary tangles underlie the feeding-swimming trade-off in starfish larvae. *Nat. Phys.*, 13 (4):380–386, 2016. → pages 89, 90

[63] R. E. Goldstein and A. Goriely. Dynamic buckling of morphoelastic filaments. *Phys. Rev. E*, 74(1), 2006. → page 31

[64] R. E. Goldstein and S. A. Langer. Nonlinear dynamics of stiff polymers. *Phys. Rev. Lett.*, 75(6):1094–1097, 1995. → page 40

[65] R. E. Goldstein, T. R. Powers, and C. H. Wiggins. Viscous nonlinear dynamics of twist and writhe. *Phys. Rev. Lett.*, 80(23):5232–5235, 1998. → page 1

[66] R. E. Goldstein, A. Goriely, G. Huber, and C. W. Wolgemuth. Bistable helices. *Phys. Rev. Lett.*, 84(7):1631–1634, 2000. → page 1

[67] R. E. Goldstein, M. Polin, and I. Tuval. Noise and synchronization in pairs of beating eukaryotic flagella. *Phys. Rev. Lett.*, 103:168103, 2009. → pages 57, 67

[68] R. E. Goldstein, M. Polin, and I. Tuval. Emergence of synchronized beating during the regrowth of eukaryotic flagella. *Phys. Rev. Lett.*, 107:148103, 2011. → page 67

[69] R. E. Goldstein, E. Lauga, A. I. Pesci, and M. R. E. Proctor. Elastohydrodynamic synchronization of adjacent beating flagella. *Phys. Rev. Fluids*, 1:073201, 2016. → page 42

[70] R. Golestanian. Synthetic mechanochemical molecular swimmer. *Phys. Rev. Lett.*, 105:018103, 2010. → page 42

[71] R. Golestanian and A. Ajdari. Analytic results for the three-sphere swimmer at low Reynolds number. *Phys. Rev. E*, 77:036308, 2008. → page 42

[72] R. Golestanian, T. B. Liverpool, and A. Ajdari. Propulsion of a molecular machine by asymmetric distribution of reaction products. *Phys. Rev. Lett.*, 94:220801, 2005. → page 9

[73] R. Golestanian, J. M. Yeomans, and N. Uchida. Hydrodynamic synchronization at low reynolds number. *Soft Matter*, 7:3074, 2011. → pages 57, 89

[74] D. Gonzalez-Rodriguez and E. Lauga. Reciprocal locomotion of dense swimmers in Stokes flow. *J. Phys. Condens. Matter*, 21:204103, 2009. → page 41

[75] J. S. Guasto, K. A. Johnson, and J. P. Gollub. Direct measurement of the flow field around swimming microorganisms. *Phys. Rev. Lett.*, 105:168102, 2010. → page 10

[76] D. C. Guell, H. Brenner, R. B. Frankel, and H. Hartman. Hydrodynamic forces and band formation in swimming magnetotactic bacteria. *J. Theor. Biol.*, 135:525–542, 1988. → page 10

[77] S. Gueron and K. Levit-Gurevich. Energetic considerations of ciliary beating and the advantage of metachronal coordination. *Proc. Natl. Acad. Sci.*, 96:12240–12245, 1999. → page 56

[78] S. Gueron, K. Levit-Gurevich, N. Liron, and J. J. Blum. Cilia internal mechanism and metachronal coordination as the result of hydrodynamical coupling. *Proc. Natl. Acad. Sci.*, 94:6001–6006, 1997. → pages 1, 56

[79] X. Gui, Z. Zeng, Z. Lin, Q. Gan, R. Xiang, Y. Zhu, A. Cao, and Z. Tang. Magnetic and highly recyclable macroporous carbon nanotubes for spilled oil sorption and separation. *ACS Appl. Mater. Interfaces*, 5(12):5845–5850, 2013. → page 87

[80] B. Guirao and J. Joanny. Spontaneous creation of macroscopic flow and metachronal waves in an array of cilia. *Biophys. J.*, 92:1900–1917, 2007. → page 67

[81] M. E. Gurtin, E. Fried, and A. Lallit. *The Mechanics and Thermodynamics of Continua*. Cambridge University Press, 2010. → page 44

[82] J. Ha, J. Kim, Y. Jung, G. Yun, D. Kim, and H. Kim. Poro-elasto-capillary wicking of cellulose sponges. *Sci. Adv.*, 4(3):eaao7051, 2018. → page 73

[83] H. Hagiwara, N. Ohwada, and K. Takata. Cell biology of normal and abnormal ciliogenesis in the ciliated epithelium. In *Int. Rev. Cytol.*, pages 101–141. Elsevier BV, 2004. → page 67

[84] J. Happel and H. Brenner. *Low Reynolds Number Hydrodynamics*. Springer Netherlands, 1981. → pages 9, 11, 17, 41, 46, 58, 60

[85] G. Harkes, J. Dankert, and J. Feijen. Bacterial migration along solid surfaces. *Appl. Environ. Microbiol.*, 58(2):1500–1505, 1992. → page 30

[86] E. J. Hinch. Note on the symmetries of certain material tensors for a particle in Stokes flow. *J. Fluid. Mech.*, 54:423, 1972. → page 11

[87] N. Hirokawa, Y. Okada, and Y. Tanaka. Fluid dynamic mechanism responsible for breaking the left-right symmetry of the human body: The nodal flow. *Annu. Rev. Fluid Mech.*, 41:53–72, 2009. → pages 1, 56

[88] D. P. Holmes, P.-T. Brun, A. Pandey, and S. Protière. Rising beyond elastocapillarity. *Soft Matter*, 12(22):4886–4890, 2016. → page 73

[89] C. J. Hooke and J. P. O'Donoghue. Elastohydrodynamic lubrication of soft, highly deformed contacts. *J. Mech. Eng. Sci.*, 14(1):34–48, 1972. → page 72

[90] J. Huang, M. Juszkiewicz, W. H. de Jeu, E. Cerda, T. Emrick, N. Menon, and T. P. Russell. Capillary wrinkling of floating thin polymer films. *Science*, 317(5838):650–653, 2007. → pages 2, 72

[91] Z.-H. Huang, M. Abkarian, and A. Viallat. Sedimentation of vesicles: from pear-like shapes to microtether extrusion. *New J. Phys.*, 13:035026, 2011. → pages 44, 50

[92] M. Iima and A. S. Mikhailov. Propulsion hydrodynamics of a butterfly micro-swimmer. *EPL*, 85:44001, 2009. → page 42

[93] T. Ishikawa, T. Tanaka, Y. Imai, T. Omori, and D. Matsunaga. Deformation of a micro-torque swimmer. *Proc. R. Soc. A*, 472:20150604, 2016. → page 50

[94] M. Jabbarzadeh and H. C. Fu. Dynamic instability in the hook-flagellum system that triggers bacterial flicks. *Phys. Rev. E*, 97(1), 2018. → pages 31, 40

[95] M. K. Jawed, N. K. Khouri, F. Da, E. Grinspun, and P. M. Reis. Propulsion and instability of a flexible helical rod rotating in a viscous fluid. *Phys. Rev. Lett.*, 115:168101, 2015. → page 42

[96] H. Kim and L. Mahadevan. Capillary rise between elastic sheets. *J. Fluid Mech.*, 548(-1):141, 2006. → page 73

[97] S. Kim. A note on Faxen laws for nonspherical particles. *Int. J. Multiph. Flow*, 11:713–719, 1985. → page 54

[98] S. Kim and J. S. Karilla. *Microhydrodynamics: principles and selected applications*. Butterworth-Heinemann, 1991. → pages 5, 10, 11, 41

[99] Y. W. Kim and R. R. Netz. Pumping fluids with periodically beating grafted elastic filaments. *Phys. Rev. Lett.*, 96:158101, 2006. → page 56

[100] G. S. Klindt, C. Ruloff, C. Wagner, and B. M. Friedrich. In-phase and anti-phase flagellar synchronization by waveform compliance and basal coupling. *New J. Phys.*, 19:113052, 2017. → pages 9, 89

[101] E. W. Knight-Jones. Relations between metachronism and the direction of ciliary beat in Metazoa. *Quart. J. Microsc. Sci.*, s3-95:503–521, 1954. → page 56

[102] J. Kotar, M. Leoni, B. Bassetti, M. Cosentino Lagomarsino, and P. Cicuta. Hydrodynamic synchronization of colloidal oscillators. *Proc. Natl. Acad. Sci.*, 107:7669–7673, 2010. → page 57

[103] M. Kvick, D. M. Martinez, D. R. Hewitt, and N. J. Balmforth. Imbibition with swelling: Capillary rise in thin deformable porous media. *Phys. Rev. Fluids*, 2(7):074001, 2017. → page 73

[104] M. C. Lagomarsino, F. Capuani, and C. P. Lowe. A simulation study of the dynamics of a driven filament in an aristotelian fluid. *J. Theor. Biol.*, 224: 215–224, 2003. → page 42

[105] E. Lauga. Life at high Deborah number. *Europhys. Lett.*, 86:64001, 2009. → pages 11, 41

[106] E. Lauga. Life around the scallop theorem. *Soft Matter*, 7:3060–3065, 2011. → pages 9, 41

[107] E. Lauga. Locomotion in complex fluids: Integral theorems. *Phys. Fluids*, 26:081902, 2014. → page 11

[108] E. Lauga and S. Michelin. Stresslets induced by active swimmers. *Phys. Rev. Lett.*, 117:148001, 2016. → pages 10, 11, 16, 23

[109] E. Lauga and T. R. Powers. The hydrodynamics of swimming microorganisms. *Rep. Prog. Phys.*, 72:096601, 2009. → pages 1, 9, 11, 27, 42

[110] E. Lauga, W. R. DiLuzio, G. M. Whitesides, and H. A. Stone. Swimming in circles: Motion of bacteria near solid boundaries. *Biophys. J.*, 90(2): 400–412, 2006. → page 30

[111] L. G. Leal. The motion of small particles in non-Newtonian fluids. *J. Non-Newton. Fluid Mech.*, 5:33–78, 1979. → page 11

[112] M. Lee, S. Kim, H. Kim, and L. Mahadevan. Bending and buckling of wet paper. *Phys. Fluids*, 28:042101, 2016. → pages 73, 76

[113] P. Lenz and A. Ryskin. Collective effects in ciliar arrays. *Phys. Biol.*, 3:285, 2006. → pages 58, 62

[114] T. G. Leong, A. M. Zarafshar, and D. H. Gracias. Three-ĂŘdimensional fabrication at small size scales. *Small*, 6(7):792–806, 2010. → page 72

[115] M. Leoni, J. Kotar, B. Bassetti, P. Cicuta, and M. Cosentino Lagomarsino. A basic swimmer at low Reynolds number. *Soft Matter*, 5:472–476, 2009. → page 42

[116] A. M. Leshansky, O. Kenneth, O. Gat, and J. E. Avron. A frictionless microswimmer. *New J. Phys.*, 9:145–145, 2007. → page 28

[117] G. Li and A. M. Ardekani. Hydrodynamic interaction of microswimmers near a wall. *Phys. Rev. E*, 90(1), 2014. → page 30

[118] G. Li, J. Bensson, L. Nisimova, D. Munger, P. Mahautmr, J. X. Tang, M. R. Maxey, and Y. V. Brun. Accumulation of swimming bacteria near a solid surface. *Phys. Rev. E*, 84(4), 2011. → page 30

[119] L. Li, H. Manikantan, D. Saintillan, and S. E. Spagnolie. The sedimentation of flexible filaments. *J. Fluid. Mech.*, 735:705–736, 2013. → page 42

[120] M. J. Lighthill. On the squirming motion of nearly spherical deformable bodies through liquids at very small Reynolds numbers. *Comm. Pure Appl. Math*, 5:109–118, 1952. → pages 24, 25

[121] M. J. Lighthill. *Mathematical Biofluiddynamics*. SIAM, 1975. → page 42

[122] N. Liron and S. Mochon. The discrete-cilia approach to propulsion of ciliated micro-organisms. *J. Fluid. Mech.*, 75:593, 1976. → page 57

[123] B. Liu, M. Gulino, M. Morse, J. X. Tang, T. R. Powers, and K. S. Breuer. Helical motion of the cell body enhances caulobacter crescentus motility. *Proc. Natl. Acad. Sci.*, 111(31):11252–11256, 2014. → page 40

[124] H. Lodish, A. Berk, S. L. Zipursky, P. Matsudaira, D. Baltimore, and J. Darnell. *Cilia and Flagella: Structure and Movement*. W. H. Freeman, New York, 2000. → pages 9, 56

[125] E. Lushi, V. Kantsler, and R. E. Goldstein. Scattering of biflagellate microswimmers from surfaces. *Phys. Rev. E*, 96(2), 2017. → page 30

[126] R. Maboudian. Critical review: Adhesion in surface micromechanical structures. *J. Vac. Sci. Technol. B Microelectron. Nanometer. Struct. Process. Meas. Phenom.*, 15(1):1, 1997. → page 72

[127] H. Machemer. Ciliary activity and the origin of metachrony in paramecium: Effects of increased viscosity. *J. Exp. Biol.*, 57:239–259, 1972. → page 70

[128] A. W. Martinez, S. T. Phillips, and G. M. Whitesides. Three-dimensional microfluidic devices fabricated in layered paper and tape. *Proc. Natl. Acad. Sci.*, 105(50):19606–19611, 2008. → pages 73, 87

[129] A. W. Martinez, S. T. Phillips, G. M. Whitesides, and E. Carrilho. Diagnostics for the developing world: Microfluidic paper-based analytical devices. *Anal. Chem.*, 82(1):3–10, 2010. → pages 73, 87

[130] S. Michelin and E. Lauga. Phoretic self-propulsion at finite Pèclet numbers. *J. Fluid Mech.*, 747:572 – 604, 2014. → page 17

[131] S. Michelin and E. Lauga. A reciprocal theorem for boundary-driven channel flows. *Phys. Fluids*, 27:111701, 2015. → page 11

[132] T. D. Montenegro-Johnson, H. Gadelha, and D. J. Smith. Spermatozoa scattering by a microchannel feature: an elastohydrodynamic model. *R. Soc. Open Sci.*, 2:140475, 2015. → page 31

[133] T. Murata. On the deformation of an elastic particle falling in a viscous fluid. *J. Phys. Soc.*, 48:1738–1745, 1980. → pages 43, 52

[134] A. Najafi and R. Golestanian. Simple swimmer at low Reynolds number: Three linked spheres. *Phys. Rev. E*, 69:062901, 2004. → pages 42, 54

[135] A. Najafi and R. Zargar. Two-sphere low-Reynolds-number propeller. *Phys. Rev. E*, 81:067301, 2010. → page 42

[136] B. Nasouri and G. J. Elfring. Hydrodynamic interactions of cilia on a spherical body. *Phys. Rev. E*, 93:033111, 2016. → pages 9, 42, 56

[137] B. Nasouri and G. J. Elfring. Higher-order force moments of active particles. *Phys. Rev. Fluids*, 3:044101, 2018. → page 9

[138] B. Nasouri, A. Khot, and G. J. Elfring. Elastic two-sphere swimmer in Stokes flow. *Phys. Rev. Fluids*, 2:043101, 2017. → pages 9, 41

[139] F. T. Nguyen and M. D. Graham. Buckling instabilities and complex trajectories in a simple model of uniflagellar bacteria. *Biophys. J.*, 112(5): 1010–1022, 2017. → pages 31, 40

[140] S. T. Nguyen, J. Feng, N. T. Le, A. T. T. Le, N. Hoang, V. B. C. Tan, and H. M. Duong. Cellulose aerogel from paper waste for crude oil spill cleaning. *Ind. Eng. Chem. Res.*, 52(51):18386–18391, 2013. → page 87

[141] T. Niedermayer, B. Eckhardt, and P. Lenz. Synchronization, phase locking, and metachronal wave formation in ciliary chains. *Chaos*, 18:037128, 2008. → pages 9, 42, 57, 58, 59, 64, 66, 90

[142] R. W. Ogden. *Non-linear elastic deformations*. Dover, 1984. → page 44

[143] Y. Okada, S. Nonaka, Y. Tanaka, Y. Saijoh, H. Hamada, and N. Hirokawa. Abnormal nodal flow precedes situs inversus in iv and inv mice. *Mol. Cell*, 4:459–468, 1999. → pages xiii, 59, 60, 61, 68

[144] G. O'Toole, H. B. Kaplan, and R. Kolter. Biofilm formation as microbial development. *Annu. Rev. Microbiol.*, 54(1):49–79, 2000. → page 30

[145] O. S. Pak and E. Lauga. Generalized squirming motion of a sphere. *J. Engrg. Math.*, 88:1–28, 2014. → pages xi, 24, 25, 26

[146] O. S. Pak, L. Zhu, L. Brandt, and E. Lauga. Micropropulsion and microrheology in complex fluids via symmetry breaking. *Phys. Fluids*, 24: 103102, 2012. → page 11

[147] O. S. Pak, J. Feng, and H. A. Stone. Viscous marangoni migration of a drop in a poiseuille flow at low surface péclet numbers. *J. Fluid. Mech.*, 753: 535–552, 2014. → page 11

[148] D. Papavassiliou and G. P. Alexander. The many-body reciprocal theorem and swimmer hydrodynamics. *EPL*, 110:44001, 2015. → page 29

[149] L. E. Payne and W. H. Pell. The Stokes flow problem for a class of axially symmetric bodies. *J. Fluid Mech.*, 7:529, 1960. → page 51

[150] R. Pericet-Camara, A. Best, H. Butt, and E. Bonaccurso. Effect of capillary pressure and surface tension on the deformation of elastic surfaces by sessile liquid microdrops: An experimental investigation. *Langmuir*, 24 (19):10565–10568, 2008. → page 72

[151] B. Pernet, editor. *Larval Feeding: Mechanisms, Rates, and Performance in Nature*. Oxford University Press, 2018. → page 89

[152] M. Polin, I. Tuval, K. Drescher, J. P. Gollub, and R. E. Goldstein. Chlamydomonas swims with two "gears" in a eukaryotic version of run-and-tumble locomotion. *Science*, 325:487–490, 2009. → page 57

[153] T. R. Powers, R. E. Goldstein, and C. H. Wiggins. Supercoiling bacterial filaments. In *AIP Conference Proceedings*. AIP, 1999. → page 1

[154] C. Pozrikidis. *Boundary integral and singularity methods for linearized viscous flow*. Cambridge University Press, 1992. → pages 5, 11, 16, 20

[155] C. Pozrikidis. *Introduction to theoretical and computational fluid dynamics*. Oxford University Press, 2011. → page 13

[156] L. A. Pratt and R. Kolter. Genetic analysis of Escherichia coli biofilm formation: roles of flagella, motility, chemotaxis and type i pili. *Mol. Microbiol*, 30(2):285–293, 1998. → page 30

[157] E. M. Purcell. Life at low Reynolds number. *Am. J. Phys.*, 45:3–11, 1977. → pages 9, 41, 42, 56

[158] C. Py, P. Reverdy, L. Doppler, J. Bico, B. Roman, and C. N. Baroud. Capillary origami: Spontaneous wrapping of a droplet with an elastic sheet. *Phys. Rev. Lett.*, 98(15), 2007. → page 2

[159] G. Quaranta, M. E. Aubin-Tam, and D. Tam. Hydrodynamics versus intracellular coupling in the synchronization of eukaryotic flagella. *Phys. Rev. Lett.*, 115:238101, 2015. → pages 9, 70, 89

[160] D. Quéré. Inertial capillarity. *Europhys. Lett.*, 39(5):533–538, 1997. → pages 76, 90

[161] J. M. Rallison. Note on the Faxén relations for a particle in Stokes flow. *J. Fluid. Mech.*, 88:529, 1978. → page 11

[162] S. Ramaswamy. The mechanics and statistics of active matter. *Annu. Rev. Condens. Matter Phys.*, 1:323–345, 2010. → page 9

[163] E. Reyssat and L. Mahadevan. How wet paper curls. *Europhys. Lett.*, 93(5): 54001, 2011. → page 73

[164] A. M. Rijke. Wettability and phylogenetic development of feather structure in water birds. *J. Exp. Biol.*, 52(2):469–479, 1970. → page 72

[165] D. Riveline, C. H. Wiggins, R. E. Goldstein, and A. Ott. Elastohydrodynamic study of actin filaments using fluorescence microscopy. *Phys. Rev. E*, 56(2):R1330–R1333, 1997. → page 40

[166] A. J. Roberts, T. Kon, P. J. Knight, K. Sutoh, and S. A. Burgess. Functions and mechanics of dynein motor proteins. *Nat. Rev. Mol. Cell Biol.*, 14: 713–726, 2013. → pages 41, 56

[167] M. Rossi, G. Cicconofri, A. Beran, G. Noselli, and A. DeSimone. Kinematics of flagellar swimming inEuglena gracilis: Helical trajectories and flagellar shapes. *Proc. Natl. Acad. Sci.*, 114(50):13085–13090, 2017. → page 89

[168] D. Saintillan. The dilute rheology of swimming suspensions: A simple kinetic model. *Exp. Mech*, 50:1275–1281, 2009. → page 10

[169] D. Saintillan and M. J. Shelley. Active suspensions and their nonlinear models. *C. R. Physique*, 14:497–517, 2013. → page 10

[170] R. A. Sampson. On Stokes's current function. *Phil. Trans. R. Soc. Lond. A*, 182:449–518, 1891. → page 46

[171] A. S. Shah, Y. Ben-Shahar, T. O. Moninger, J. N. Kline, and M. J. Welsh. Motile cilia of human airway epithelia are chemosensory. *Science*, 325: 1131–1134, 2009. → pages 1, 56

[172] N. Sharifi-Mood, A. Mozaffari, and U. M. Córdova-Figueroa. Pair interaction of catalytically active colloids: from assembly to escape. *J. Fluid. Mech.*, 798:910–954, 2016. → page 29

[173] H. Shum and E. A. Gaffney. The effects of flagellar hook compliance on motility of monotrichous bacteria: A modeling study. *Phys. Fluids*, 24(6): 061901, 2012. → pages 31, 40

[174] K. Singh, J. R. Lister, and D. Vella. A fluid-mechanical model of elastocapillary coalescence. *J. Fluid Mech.*, 745:621–646, 2014. → pages 73, 87

[175] D. J. Smith and J. R. Blake. Surface accumulation of spermatozoa: A fluid dynamic phenomenon. *Math. Sci.*, 34:74–87, 2009. → page 16

[176] J. H. Snoeijer. Analogies between elastic and capillary interfaces. *Phys. Rev. Fluids*, 1(6):060506, 2016. → page 72

[177] K. Son, J. S. Guasto, and R. Stocker. Bacteria can exploit a flagellar buckling instability to change direction. *Nature Phys.*, 9:494–498, 2013. → pages 1, 31, 42, 89

[178] S. E. Spagnolie and E. Lauga. Jet propulsion without inertia. *Phys. Fluids*, 22:081902, 2010. → page 11

[179] S. E. Spagnolie and E. Lauga. Hydrodynamics of self-propulsion near a boundary: predictions and accuracy of far-field approximations. *J. Fluid Mech*, 700:105–147, 2012. → pages 16, 29

[180] S. E. Spagnolie and E. Lauga. Hydrodynamics of self-propulsion near a boundary: predictions and accuracy of far-field approximations. *J. Fluid. Mech.*, 700:105–147, 2012. → pages 30, 35, 40

[181] S. E. Spagnolie, G. R. Moreno-Flores, D. Bartolo, and E. Lauga. Geometric capture and escape of a microswimmer colliding with an obstacle. *Soft Matter*, 11:3396–3411, 2015. → pages 30, 31, 61

[182] S. E. Spagnolie, C. Wahl, J. Lukasik, and J. Thiffeault. Microorganism billiards. *Physica D*, 341:33–44, 2017. → page 30

[183] R. Stocker, J. R. Seymour, A. Samadani, D. E. Hunt, and M. F. Polz. Rapid chemotactic response enables marine bacteria to exploit ephemeral microscale nutrient patches. *Proc. Natl. Acad. Sci.*, 105(11):4209–4214, 2008. → page 30

[184] H. A. Stone and A. D. T. Samuel. Propulsion of microorganisms by surface distortions. *Phys. Rev. Lett.*, 77:4102–4104, 1996. → pages 11, 16, 23

[185] J. W. Swan and J. F. Brady. Simulation of hydrodynamically interacting particles near a no-slip boundary. *Phys. Fluids*, 19(11):113306, 2007. → page 29

[186] D. Takagi, J. Palacci, A. B. Braunschweig, M. J. Shelley, and J. Zhang. Hydrodynamic capture of microswimmers into sphere-bound orbits. *Soft Matter*, 10(11):1784, 2014. → page 30

[187] M. Taroni and D. Vella. Multiple equilibria in a simple elastocapillary system. *J. Fluid Mech.*, 712:273–294, 2012. → page 73

[188] T. D. Taylor and A. Acrivos. On the deformation and drag of a falling viscous drop at low Reynolds number. *J. Fluid Mech.*, 18:466, 1964. → page 47

[189] D. Topgaard and O. Söderman. Diffusion of water absorbed in cellulose fibers studied with1h-NMR. *Langmuir*, 17(9):2694–2702, 2001. → page 73

[190] R. Trouilloud, T. S. Yu, A. E. Hosoi, and E. Lauga. Soft swimming: Exploiting deformable interfaces for low Reynolds number locomotion. *Phys. Rev. Lett.*, 101:048102, 2008. → page 41

[191] N. Uchida and R. Golestanian. Generic conditions for hydrodynamic synchronization. *Phys. Rev. Lett.*, 106:058104, 2011. → page 57

[192] A. Vilfan and F. Jülicher. Hydrodynamic flow patterns and synchronization of beating cilia. *Phys. Rev. Lett.*, 96:058102, 2006. → pages 57, 62

[193] M. M. Villone, F. Greco, M. Hulsen, and P. L. Maffettone. Numerical simulations of deformable particle lateral migration in tube flow of Newtonian and viscoelastic media. *J. Non-Newton Fluid.*, 234:105–113, 2016. → page 44

[194] A. Walther and H. E. Müller. Janus particles: Synthesis, self-assembly, physical properties, and applications. *Chem. Rev.*, 113:5194–5261, 2013. → page 9

[195] K. Y. Wan and R. E. Goldstein. Emergence of synchronized beating during the regrowth of eukaryotic flagella. *Phys. Rev. Lett.*, 113:238103, 2014. → page 67

[196] K. Y. Wan and R. E. Goldstein. Coordinated beating of algal flagella is mediated by basal coupling. *Proc. Natl. Acad. Sci.*, 113:E2784–E2793, 2016. → pages 9, 89

[197] E. W. Washburn. The dynamics of capillary flow. *Phys. Rev.*, 17:273–283, 1921. → pages xiv, 72, 76, 81

[198] C. H. Wiggins and R. E. Goldstein. Flexive and propulsive dynamics of elastica at low Reynolds number. *Phys. Rev. Lett.*, 80:3879, 1998. → page 42

[199] C. H. Wiggins, D. Riveline, A. Ott, and R. E. Goldstein. Trapping and wiggling: Elastohydrodynamics of driven microfilaments. *Biophys. J.*, 74 (2):1043–1060, 1998. → page 31

[200] H. Winet, G. S. Bernstein, and J. Head. Observations on the response of human spermatozoa to gravity, boundaries and fluid shear. *Reproduction*, 70(2):511–523, 1984. → page 30

[201] C. W. Wolgemuth, T. R. Powers, and R. E. Goldstein. Twirling and whirling: Viscous dynamics of rotating elastic filaments. *Phys. Rev. Lett.*, 84(7):1623–1626, 2000. → page 31

[202] C. W. Wolgemuth, R. E. Goldstein, and T. R. Powers. Dynamic supercoiling bifurcations of growing elastic filaments. *Physica D*, 190(3-4): 266–289, 2004. → page 31

[203] C. Wollin and H. Stark. Metachronal waves in a chain of rowers with hydrodynamic interactions. *Eur. Phys. J. E*, 34:42, 2011. → pages 57, 70

[204] Y.-N. Young and M. J. Shelley. Stretch-coil transition and transport of fibers in cellular flows. *Phys. Rev. Lett.*, 99(5), 2007. → page 31

Appendix A

Auxiliary flow field and stress field calculations of a spherical active particle

Here we present expressions for the auxiliary flow field and stress field considered for an active spherical particle in Chapter 3. For simplicity, we define the flow associated with rigid-body translation as $\hat{\mathbf{u}}'_U = \hat{\mathbf{G}}_U \cdot \left(\hat{\mathbf{U}} - \hat{\mathbf{U}}^\infty\right)$, which from equation (3.33) gives $\hat{\mathbf{u}}'_U(\mathbf{x} \in \partial\mathcal{B}) = \hat{\mathbf{U}} - \hat{\mathbf{U}}^\infty$. Thus, for a sphere, $\hat{\mathbf{P}}_U$, $\hat{\mathbf{G}}_U$ and $\hat{\mathbf{T}}_U$ can be simply found

$$\hat{P}_{U,i} = \frac{3a}{2\left(x_l x_l\right)^{\frac{3}{2}}} x_i, \tag{A.1}$$

$$\hat{G}_{U,ij} = \left(\frac{3a}{4\left(x_l x_l\right)^{\frac{1}{2}}} + \frac{a^3}{4\left(x_l x_l\right)^{\frac{3}{2}}}\right)\delta_{ij} + \left(\frac{3a}{4\left(x_l x_l\right)^{\frac{3}{2}}} - \frac{3a^3}{4\left(x_l x_l\right)^{\frac{5}{2}}}\right)x_i x_j, \tag{A.2}$$

$$\hat{T}_{U,ijk} = \left(-\frac{9a}{2\left(x_l x_l\right)^{\frac{5}{2}}} + \frac{15a^3}{2\left(x_l x_l\right)^{\frac{7}{2}}}\right)x_i x_j x_k - \frac{3a^3}{2\left(x_l x_l\right)^{\frac{5}{2}}}\left(x_i\delta_{jk} + x_j\delta_{ik} + x_k\delta_{ij}\right). \tag{A.3}$$

Similarly, $\hat{\mathbf{u}}'_{\Omega}(\mathbf{x} \in \partial\mathcal{B}) = \left(\hat{\mathbf{\Omega}} - \hat{\mathbf{\Omega}}^{\infty}\right) \times \mathbf{r}$ leads to

$$\hat{P}_{\Omega,i} = 0, \tag{A.4}$$

$$\hat{G}_{\Omega,ij} = \frac{a^3}{(x_l x_l)^{\frac{3}{2}}} \epsilon_{ijk} x_k, \tag{A.5}$$

$$\hat{T}_{\Omega,ijk} = \frac{3a^3}{(x_l x_l)^{\frac{5}{2}}} \left[\epsilon_{kis} x_j + \epsilon_{kjs} x_i\right] x_s. \tag{A.6}$$

Relevant to the stresslet calculations, we impose $\hat{\mathbf{u}}'_{E}(\mathbf{x} \in \partial\mathcal{B}) = \mathbf{r} \cdot \left(-\hat{\mathbf{E}}^{\infty}\right)$ in which $\hat{\mathbf{E}}^{\infty}$ is a symmetric and deviatoric second-order tensor and so

$$\hat{P}_{E,ij} = \frac{5a^3}{(x_l x_l)^{\frac{5}{2}}} \overbrace{x_i x_j}, \tag{A.7}$$

$$\hat{G}_{E,ijk} = \frac{a^5}{(x_l x_l)^{\frac{5}{2}}} \overbrace{\delta_{ij} x_k}^{jk} + \frac{5}{2}\left(\frac{a^3}{(x_l x_l)^{\frac{5}{2}}} - \frac{a^5}{(x_l x_l)^{\frac{7}{2}}}\right) x_i \overbrace{x_j x_k}, \tag{A.8}$$

$$\begin{aligned}\hat{T}_{E,ijkm} = {} & \frac{a^5}{(x_l x_l)^{\frac{5}{2}}} \left(\delta_{kj}\delta_{im} + \delta_{ki}\delta_{jm}\right) + 5\left(\frac{7a^5}{(x_l x_l)^{\frac{9}{2}}} - \frac{5a^3}{(x_l x_l)^{\frac{7}{2}}}\right) x_i x_j x_k x_m \\ & + \frac{5a^3}{2(x_l x_l)^{\frac{5}{2}}} \left(\delta_{kj} x_i x_m + \delta_{ki} x_j x_m + \delta_{mj} x_i x_k + \delta_{mi} x_j x_k\right) \\ & - \frac{5a^5}{(x_l x_l)^{\frac{7}{2}}} \left(\delta_{im} x_k x_j + \delta_{jm} x_k x_i + \delta_{ij} x_k x_m + \delta_{jk} x_i x_m + \delta_{ik} x_j x_m\right).\end{aligned} \tag{A.9}$$

In determining the stresslet dipole, we have $\hat{\mathbf{u}}'_{\Gamma}(\mathbf{x} \in \partial\mathcal{B}) = \mathbf{rr} : \left(-\hat{\mathbf{\Gamma}}^{\infty}\right)$. Noting that $\hat{\mathbf{\Gamma}}^{\infty}$ is a fully symmetric, deviatoric third-order tensor, we find

$$\hat{P}_{\Gamma,ijk} = \frac{35}{4} \frac{a^5}{(x_l x_l)^{\frac{7}{2}}} \overbrace{x_i x_j x_k}, \tag{A.10}$$

$$\hat{G}_{\Gamma,ijkm} = \frac{1}{8}\left(\frac{15a^7}{(x_l x_l)^{\frac{7}{2}}} - \frac{7a^5}{(x_l x_l)^{\frac{5}{2}}}\right) \overbrace{\delta_{im} x_j x_k}^{jkm} + \frac{35}{8}\left(\frac{a^5}{(x_l x_l)^{\frac{7}{2}}} - \frac{a^7}{(x_l x_l)^{\frac{9}{2}}}\right) x_i \overbrace{x_j x_k x_m}, \tag{A.11}$$

and

$$
\begin{aligned}
&\hat{T}_{\Gamma,ijkmn} = \\
&\frac{15}{8}a^7\left\{\delta_{ni}\left[\frac{\delta_{jk}x_m+\delta_{mj}x_k}{(x_lx_l)^{\frac{7}{2}}}-\frac{7x_jx_kx_m}{(x_lx_l)^{\frac{9}{2}}}\right]+\delta_{nj}\left[\frac{\delta_{ik}x_m+\delta_{im}x_k}{(x_lx_l)^{\frac{7}{2}}}-\frac{7x_ix_kx_m}{(x_lx_l)^{\frac{9}{2}}}\right]\right\}\\
&-\frac{7}{8}a^5\left\{\delta_{ni}\left[\frac{\delta_{jk}x_m+\delta_{mj}x_k}{(x_lx_l)^{\frac{5}{2}}}-\frac{5x_jx_kx_m}{(x_lx_l)^{\frac{7}{2}}}\right]+\delta_{nj}\left[\frac{\delta_{ik}x_m+\delta_{im}x_k}{(x_lx_l)^{\frac{5}{2}}}-\frac{5x_ix_kx_m}{(x_lx_l)^{\frac{7}{2}}}\right]\right\}\\
&+\frac{35}{4}a^5\left[-\frac{7x_ix_jx_kx_mx_n}{(x_lx_l)^{\frac{9}{2}}}\right]-\frac{35}{4}a^7\left[\frac{\delta_{ij}x_mx_nx_k}{(x_lx_l)^{\frac{9}{2}}}-\frac{9x_ix_jx_mx_nx_k}{(x_lx_l)^{\frac{11}{2}}}\right]\\
&+\frac{35}{8}\left(\frac{a^5}{(x_lx_l)^{\frac{7}{2}}}-\frac{a^7}{(x_lx_l)^{\frac{9}{2}}}\right)\Big[\delta_{jk}x_ix_mx_n+\delta_{jm}x_ix_kx_n+\delta_{jn}x_ix_kx_m\\
&+\delta_{ik}x_jx_mx_n+\delta_{im}x_jx_kx_n+\delta_{in}x_jx_kx_m\Big].
\end{aligned}
\tag{A.12}
$$

For a sphere with boundary condition $\hat{\mathbf{u}}'_\Lambda(\mathbf{x}\in\partial\mathcal{B}) = (\boldsymbol{\epsilon}\cdot\mathbf{r})\,\mathbf{r} : \left(-\hat{\boldsymbol{\Lambda}}^\infty\right)$, wherein $\hat{\boldsymbol{\Lambda}}^\infty$ is a second-order symmetric and deviatoric tensor, we have

$$\hat{P}_{\Lambda,ij} = 0, \tag{A.13}$$

$$\hat{G}_{\Lambda,ijk} = a^5\frac{\overbrace{\epsilon_{ijm}x_mx_k}^{jk}}{(x_lx_l)^{\frac{5}{2}}}, \tag{A.14}$$

$$
\begin{aligned}
\hat{T}_{\Lambda,ijkm} = &\frac{a^5}{(x_lx_l)^{\frac{5}{2}}}\left(\epsilon_{iks}\delta_{mj}x_s+\epsilon_{jks}\delta_{mi}x_s+\epsilon_{kmi}x_j+\epsilon_{kmj}x_i\right)\\
&-\frac{5a^5}{(x_lx_l)^{\frac{7}{2}}}x_mx_s\left(\epsilon_{iks}x_j+\epsilon_{jms}x_i\right).
\end{aligned}
\tag{A.15}
$$

Finally, $\hat{\mathbf{u}}'_e(\mathbf{x} \in \partial\mathcal{B}) = \left(2|\mathbf{r}|^2\mathbf{I} - \mathbf{rr}\right) \cdot (-\hat{\mathbf{e}}^\infty)$ yields

$$\hat{P}_{e,i} = \frac{5a^3}{2(x_l x_l)^{\frac{3}{2}}} x_i, \tag{A.16}$$

$$\hat{G}_{e,ij} = \left(\frac{3a^5}{4(x_l x_l)^{\frac{3}{2}}} + \frac{5a^3}{4(x_l x_l)^{\frac{1}{2}}} \right) \delta_{ij} - \left(\frac{9a^5}{4(x_l x_l)^{\frac{5}{2}}} - \frac{5a^3}{4(x_l x_l)^{\frac{3}{2}}} \right) x_i x_j, \tag{A.17}$$

$$\hat{T}_{e,ijk} = \frac{15}{2} \left(\frac{3a^5}{(x_l x_l)^{\frac{7}{2}}} - \frac{a^3}{(x_l x_l)^{\frac{5}{2}}} \right) x_i x_j x_k - \frac{9a^5}{2(x_l x_l)^{\frac{5}{2}}} \left(\delta_{ij} x_k + \delta_{ik} x_j + \delta_{jk} x_i \right). \tag{A.18}$$